JETP Letters, Vol. 82, No. 4, 2005, pp. 169–173. From Pis'ma v Zhurnal Éksperimental'noĭ i Teoreticheskoĭ Fiziki, Vol. 82, No. 4, 2005, pp. 187–191.

Inflaton Field Potential Producing an Exactly Flat Spectrum of Adiabatic Perturbations¶

A. A. Starobinsky

Landau Institute for Theoretical Physics, Russian Academy of Sciences, Moscow, 119334 Russia

Received July 7, 2005

Presented in this letter is the exact solution of the problem of finding the potential of an inflaton scalar field for which adiabatic perturbations generated during a de Sitter (inflationary) stage in the early Universe have an exactly flat (or, the Harrison–Zeldovich) initial spectrum. This solution lies outside the scope of the slow-roll approximation and higher-order corrections to it. The potential found depends on two arbitrary physical constants, one of which determines the amplitude of the perturbations. For small (zero) values of the other constant, a long (infinite) inflationary stage with slow rolling of the inflaton field exists. © *2005 Pleiades Publishing, Inc.*

PACS numbers: 98.80.–k

The great increase in the amount and accuracy of the cosmological observational data obtained already and expected in the near future makes possible the ambitious program of determination of an initial power spectrum $P_0(k)$ of inhomogeneous density perturbations in the Universe directly from data. Then, if working within the scope of the simplest versions of the inflationary scenario of the early Universe (i.e., with one slowly rolling scalar field ϕ—the inflaton), a natural next step is to reconstruct an effective self-interaction inflaton potential $V(\phi)$ leading to the generation of such $P_0(k)$ from inflaton quantum vacuum fluctuations during a de Sitter (inflationary) stage. Note that, in inflationary cosmology, an initial power spectrum means the spectrum that was formed by the end of the inflationary stage, i.e., by the beginning of a postinflationary power-law evolution of the Universe (it was first calculated in [1] for the $R + R^2$ model [2] and in [3–5] for the new inflationary model [6, 7]). Here $k = |\mathbf{k}|$, and the spatial dependence $\exp(i\mathbf{kr})$ of all the Fourier modes of adiabatic (scalar) perturbations is assumed.

From the mathematical point of view, since quantum generation of perturbations reduces to a kind of scattering problem, the reconstruction of $V(\phi)$ may be considered as a specific inverse scattering problem. Its solution is known in the slow-roll approximation for the inflaton field, including first [8], second [9] and third [10] order corrections to this basic approximation with respect to small slow-roll parameters, and in the so-called general slow-roll approximation [11, 12]. It is nonunique if additional information about the spectrum of primordial gravitational waves generated during a de Sitter (inflationary) stage [13] is not used. Namely, generally, there exists a one-parameter family of $V(\phi)$ producing the same $P_0(k)$ (here and below I don't count one more trivial free parameter corresponding to invariance with respect to a constant shift of the inflaton field: $\phi \longrightarrow \phi + \phi_0$). However, an exact solution of the reconstruction problem is desirable for at least two purposes:

(1) to investigate how good the convergence of the perturbation series in powers of slow-roll parameters is (if it takes place at all); and

(2) to determine the exact degree of degeneracy of the problem, i.e., to find the measure of a set of potentials producing the same perturbation spectrum.

In particular, the problem of accuracy of the slow-roll approximation prediction for $P_0(k)$ (including higher order corrections) has been intensively and critically studied recently using different methods: [14], [15] (the uniform approximation), [16] (the improved WKB approximation), and others.

By an exact solution, I mean a solution of the following system of equations for a spatially-flat Friedmann–Robertson–Walker (FRW) background with a scale factor $a(t)$ and scalar (adiabatic) perturbations described by the Mukhanov variable $Q \equiv u/a$:

$$H^2 = \frac{8\pi G}{3}\left(\frac{\dot\phi^2}{2} + V(\phi)\right), \tag{1}$$

$$\ddot\phi + 3H\dot\phi + \frac{dV}{d\phi} = 0, \tag{2}$$

$$\frac{d^2u_k}{d\eta^2} + \left(k^2 - \frac{1}{z}\frac{d^2z}{d\eta^2}\right)u_k = 0, \tag{3}$$

obtained without any approximations. Here

$$H = \frac{\dot a}{a}, \quad z = \frac{a\dot\phi}{H}, \quad \eta = \int\frac{dt}{a(t)}, \tag{4}$$

¶ The text was submitted by the author in English.

0021-3640/05/8204-0169$26.00 © 2005 Pleiades Publishing, Inc.

dot means the derivative with respect to t, $u_k(\eta)\exp(i\mathbf{kr})$ is the wave function of a Fourier mode of the quantum field u (the c-number multiplying the Fock annihilation operator $\hat{a}_\mathbf{k}$), and $c = \hbar = 1$ holds throughout the paper. The variable Q [17] is equal to $\delta\phi_L + \frac{\dot\phi}{H}\Phi$ in the longitudinal gauge (Φ is the quasi-Newtonian gravitational potential) or to $\delta\phi_S - \frac{\dot\phi}{6H}(\mu + \lambda)$ in the synchronous gauge (μ and λ are the Lifshits variables). The normalized initial condition for u_k corresponding to the adiabatic vacuum at $t \longrightarrow -\infty$ ($\eta \longrightarrow -\infty$) is

$$u_k = e^{-ik\eta}/\sqrt{2k}. \tag{5}$$

At late times during an inflationary stage in the super-horizon regime ($k \ll aH$, $\eta \longrightarrow 0$),

$$u_k/z = HQ_k/\dot\phi \longrightarrow \text{const} = \zeta(k) \tag{6}$$

($\zeta = -h/2$ in the notation of [4]).

Then, the initial spectrum of adiabatic perturbations for a postinflationary cosmology in the super-horizon regime is (assuming the absence of nondiagonal pressure components)

$$\langle\Phi^2\rangle = \left(1 - \frac{H}{a}\int_0^t a\,dt\right)^2\langle\zeta^2\rangle$$

$$= \left(1 - \frac{H}{a}\int_0^t a\,dt\right)^2\int P_0(k)\frac{dk}{k}, \tag{7}$$

$$P_0(k) = \frac{k^3\zeta^2(k)}{2\pi^2}.$$

Here $t = 0$ corresponds to the end of inflation. For historical reasons, the slope n_S of the spectrum is defined with respect to density perturbations in the nonrelativistic dark matter + baryon component at the present time, $(\delta\rho)_k = -k^2\Phi_k/4\pi Ga^2$ before integration over d^3k. So, $n_S = 1 + d\ln P_0(k)/d\ln k$ in k. Finally, using the equation $\dot H = -4\pi G\dot\phi^2$, which follows from Eqs. (1) and (2), Eq. (1) can be recast in the Hamilton–Jacobi form [18]:

$$H^2(\phi) - \frac{H'^2(\phi)}{12\pi G} = \frac{8\pi G}{3}V(\phi), \tag{8}$$

where the prime denotes the derivative with respect to ϕ.

Exact solutions of the inverse problem of reconstruction of $V(\phi)$ given $P_0(k)$ are known for the following two cases only if we are not considering solutions describing Universes collapsing towards a singularity.

(1) A power-law perturbation spectrum with the slope $n_S = \text{const} < 1$ [19]. Then,

$$V(\phi) \propto H^2(\phi) \propto \exp\left(\pm\sqrt{\frac{16\pi G}{q}}\phi\right),$$
$$a(t) \propto t^q, \quad q = \frac{3 - n_S}{1 - n_S} > 1. \tag{9}$$

This is just the power-law inflation. Considered as a function of $\phi(t)$, H is related to $V(\phi)$ through Eq. (8). Note, however, that this is not the only potential producing the $n_S = \text{const} < 1$ spectrum.

(2) The case when no perturbations are generated at all (no real created quanta of the inflaton field) [20]:

$$H(\phi) = H_1\exp(2\pi G\phi^2),$$
$$V(\phi) = \frac{3H_1^2}{8\pi G}\left(1 - \frac{4\pi G\phi^2}{3}\right)\exp(4\pi G\phi^2). \tag{10}$$

In the literature, this case is sometimes incorrectly referred to as the potential generating the $n_S = 3$ perturbation spectrum. However, one should not forget that generated perturbations are quantum (even quantum-gravitational) and require renormalization. After subtraction of the vacuum energy $\omega(t)/2 = k/2a(t)$ of each mode, no created fluctuations remain in this case. Moreover, the number of real inflaton quanta generated in each perturbation mode $\mathbf{k}$ should be large, because, in the opposite case, they may not be interpreted as classical perturbations after the end of the inflation (see [21] for a more detailed discussion of this point).

Strictly speaking, there is no exit from inflation for the potential (9), and the potential (10) does not admit a low curvature regime at all. However, in the former case, $V(\phi)$ can be deformed such that it reaches zero at a sufficiently large value of ϕ. This will result in a very small change of the perturbation spectrum at the present scales of interest that may be safely neglected. Sometimes, the case of a parabolic potential near its maximum $V(\phi) = V_0 - m^2\phi^2/2$ is mentioned as an exactly soluble case. However, it is not the one in our terminology, since, in this case, $H(\phi)$ is approximated by the constant value $H_0 = \sqrt{8\pi GV_0/3}$.

In this paper, a family of exact solutions for the case $n_S = 1$ is constructed. It is just the initial spectrum proposed by Harrison and Zeldovich [22], after all, for aesthetic reasons. Note that it satisfies the most recent CMB data [23, 24]. Let us first consider what follows for this case from the slow-roll approximation. Then, the leading term in the power spectrum reads

$$k^3\zeta^2(k) \propto (V^3/V'^2)_{t = t_k}, \tag{11}$$

where t_k is the moment when $k = aH$. It is clear that, to get $n_S = 1$, $V^{3/2}/V'$ should not depend on ϕ. Therefore, $V(\phi) \propto \phi^{-2}$. Note that this solution of the reconstruction problem is unique for a given amplitude of the flat spec-

trum. This kind of inflation was dubbed intermediate inflation in [25] (see also [26]). Its scale factor behavior is $a(t) \propto \exp(\mathrm{const} t^{2/3})$. Once more, it does not have an exit from inflation, so it should be modified at large ϕ. A next order slow-roll correction to this potential was considered in [27].

To obtain an exact solution for $H(\phi)$ and $V(\phi)$ in the case $n_S = 1$, note first that, for

$$\frac{1}{z}\frac{d^2z}{d\eta^2} = \frac{2}{\eta^2}, \tag{12}$$

Eq. (3) reduces to the equation for a massless scalar field in the de Sitter background and has the solution

$$u_k = \frac{e^{-ik\eta}}{\sqrt{2k}}\left(1 - \frac{i}{k\eta}\right) \tag{13}$$

satisfying the initial condition (5). Let us write the general solution of Eq. (12) in the form

$$z = \frac{B}{|\eta|}\left(1 + \frac{|\eta|^3}{\eta_0^3}\right), \quad \eta < 0, \tag{14}$$

where A, η_0 are constants. The limiting case $\eta_0 \longrightarrow 0$, when the first term in brackets may be neglected, is not interesting because it corresponds to a collapsing universe (however, it is dual to the case $\eta_0 \longrightarrow \infty$ considered below). The power spectrum of the growing perturbation mode is $P_0(k) = 1/4\pi^2B^2$ and does not depend on η_0 (η_0 appears in the amplitude of the decaying mode only and makes it nonscale free). Thus, we have the exactly flat spectrum. Present observational CMB data [24] fix the quantity B with ≈10% accuracy:

$$\frac{1}{2\pi B} = 4.8 \times 10^{-5}\left(\frac{A}{0.9}\exp(\tau - 0.17)\right)^{1/2}, \tag{15}$$

where A is the quantity introduced in [24] and τ is the optical length after recombination. In this notation, $A = 0.9$ corresponds to the value $A = 4.3 \times 10^{-4}$ of the other quantity A introduced in [28] to characterize an amplitude of initial perturbations (and it is conjectured to lie in the range $(3–10) \times 10^{-4}$ in that paper).

Since the aim of this paper is to find some exact solution, I will not investigate them if there exist other forms of z leading to the $n_S = 1$ spectrum too. The absence of other solutions for z would immediately follow from scaling arguments if we assume that $u_k \propto k^{-1/2}f(k\eta)$ for all η. However, the latter assumption might not be necessary. Moreover, I will consider only one particular case of Eq. (14) corresponding to the limit $\eta_0 \longrightarrow \infty$.

So, let $z = -B/\eta$. Let us express all the quantities of interest as functions of ϕ:

$$\begin{aligned} t &= -4\pi G\int\frac{d\phi}{H'}, \\ \ln a &= \int H(t)dt = -4\pi G\int\frac{H}{H'}d\phi, \\ \eta &= \int\frac{dt}{a(t)} = -4\pi G\int\frac{d\phi}{H'}\exp\left(4\pi G\int\frac{H}{H'}d\phi\right), \\ z &= \frac{a\dot\phi}{H} = -\frac{H'}{4\pi GH}\exp\left(-4\pi G\int\frac{H}{H'}d\phi\right). \end{aligned} \tag{16}$$

Equating the last line in Eq. (16) to $-B/\eta$, we get the following equation:

$$\int P(\phi)d\phi = -BHP, \quad P \equiv \frac{4\pi G}{H'}\exp\left(4\pi G\int\frac{H}{H'}d\phi\right). \tag{17}$$

After differentiation, Eq. (17) reduces to $P = -B(HP' + H'P)$, or

$$\frac{4\pi GH^2}{H'} - \frac{HH''}{H'} + H' + \frac{1}{B} = 0. \tag{18}$$

Let us introduce the dimensionless variables

$$\begin{aligned} x &= \sqrt{4\pi G}\phi, \quad y = B\sqrt{4\pi G}H, \\ V(x) &= \frac{32\pi^2G^2B^2}{3}V(\phi). \end{aligned} \tag{19}$$

Then, from (8), $V = y^2 - (1/3)(dy/dx)^2$. For these variables, Eq. (18) reads:

$$y\frac{d^2y}{dx^2} = \left(\frac{dy}{dx}\right)^2 + \frac{dy}{dx} + y^2. \tag{20}$$

After dividing by y^2, the last equation can be integrated to $dy/dx = xy - 1$ (an integration constant is excluded by shifting x, i.e., ϕ). Therefore,

$$y = e^{x^2/2}\left(\int_x^\infty e^{-\tilde x^2/2}d\tilde x + C\right), \tag{21}$$

where C is another integration constant. This just yields us a one-parameter family of solutions having $n_S = 1$. The so-called slow-roll parameters for this solution are the following:

$$\begin{aligned} \epsilon(\phi) &\equiv \frac{1}{4\pi G}\frac{H'^2}{H^2} = \left(\frac{1}{y} - x\right)^2, \\ \tilde\eta(\phi) &\equiv \frac{1}{4\pi G}\frac{H''}{H} = \frac{1}{y}\frac{d^2y}{dx^2} = x^2 - \frac{x}{y} + 1. \end{aligned} \tag{22}$$

The partial solution with $C = 0$ has an infinite inflationary stage that is just described by the slow-roll

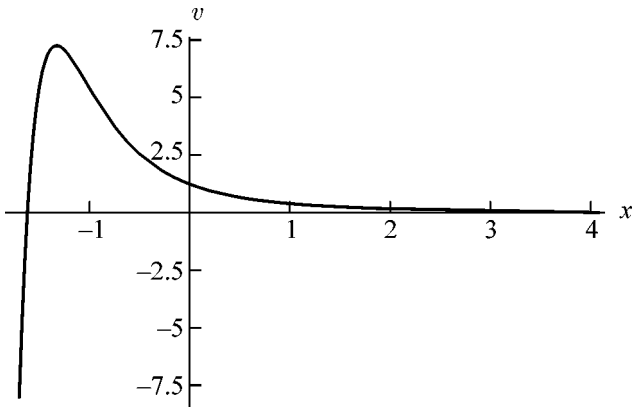

The dimensionless potential $v(x)$ for the $C = 0$ case.

approximation for $x \gg 1$. Its graph is plotted in the figure. Its large x expansion is

$$y = \frac{1}{x} - \frac{1}{x^3} + \frac{3}{x^5} - \frac{15}{x^7} + \ldots,$$
$$v = \frac{1}{x^2} - \frac{7}{3x^4} + \frac{9}{x^6} - \ldots. \quad (23)$$

It is straightforward to check that it leads to $n_S = 1$ (as it should) for the first [8] and second [9] order corrections to the slow-roll approximation. However, these corrections miss the whole 1-parametric family with $C \neq 0$ completely.

For $x < 0$, the solution with $C = 0$ has rather a particular behavior: the potential $v(x)$ reaches the maximum value $v_{\max} \approx 7.252$ at $x \approx -1.326$, becomes zero at $x \approx -1.618$, and then goes to $-\infty$ at $x \longrightarrow -\infty$ (however, such effective potentials are considered in string inspired models now). In the latter limit, $y \longrightarrow \infty$, so we get an initial curvature singularity at the finite proper time $t_0 < 0$. If $t = 0$ is the moment when $x = 0$ ($v(0) = \pi/2 - 1/3 \approx 1.237$) and the inflationary stage begins, then $|t_0| \sim H^{-1}(0) \sim BG^{1/2}$. The scale factor reaches zero very slowly: $a(t) \propto |\ln(t - t_0)|^{-1/2}$ for $t \longrightarrow t_0$. Still, the Riemann tensor is not twice integrable for $t \longrightarrow t_0$, so this singularity is a strong one. The same refers to all the initially expanding ($y > 0$) solutions with $C \neq 0$ and $C > -\sqrt{2\pi}$—they all begin from such a singularity.

By taking $C < 0$ and very small, it becomes possible to construct a solution with a long but finite inflationary stage. Namely, if $C = -\sqrt{3}x_1^{-2}\exp(-x_1^2/2)$ with $x_1 \gg 1$, then $v(x)$ becomes zero at $x = x_1$ (y still remains $\sim x_1^{-1}$). In this case, inflation ends ($\epsilon, |\tilde{\eta}| \sim 1$) at $x = x_1 - \mathbb{O}(x_1^{-1})$. The total number of e folds is $N_{\text{tot}} = 2\pi G\phi_1^2 = x_1^2/2$. Thus, $C \sim \exp(-N_{\text{tot}})$, which is in agreement with the general principle that terms not caught by an arbitrary order of a WKB-type expansion are exponentially small. For $x \geq x_1$, one may put $v \equiv 0$. Then, the kinetic dominated phase $a(t) \propto t^{1/3}$ follows the inflationary stage. Otherwise, we may assume that v has a local minimum $v = \frac{1}{2}\mu^2(x - x_1)^2$ around this point. It results in oscillations in ϕ and the matter-dominated postinflationary stage $a(t) \propto t^{2/3}$.

Finally, note that the spectrum of gravitational waves (GW) is not flat for this model: for $1 \ll x \ll x_1$, the tensor–scalar ratio and the slope of the GW initial power spectrum $r = -8n_T = 16/x^2 = 8/N$, where N is the number of e-folds from the beginning of inflation. The present upper observational bound $r < 0.36$ [29] requires $N > 22$ for the comoving scale crossing the Hubble radius at present. So, N_{tot} should exceed ~70 in this model.

This research was partially supported by the Russian Foundation for Basic Research (project no. 05-02-17450), by the Russian Academy of Sciences (research program "Elementary Particles"), and by the Russian Ministry of Education and Science (Scientific School project no. 2338.2003.2).

REFERENCES

1. V. F. Mukhanov and G. V. Chibisov, Pis'ma Zh. Éksp. Teor. Fiz. **33**, 549 (1981) [JETP Lett. **33**, 532 (1981)].
2. A. A. Starobinsky, Phys. Lett. B **91B**, 99 (1980).
3. S. W. Hawking, Phys. Lett. B **115B**, 295 (1982).
4. A. A. Starobinsky, Phys. Lett. B **117B**, 175 (1982).
5. A. H. Guth and S.-Y. Pi, Phys. Rev. Lett. **49**, 1110 (1982).
6. A. D. Linde, Phys. Lett. B **108B**, 389 (1982).
7. A. Albrecht and P. J. Steinhardt, Phys. Rev. Lett. **48**, 1220 (1982).
8. E. D. Stewart and D. H. Lyth, Phys. Lett. B **302**, 171 (1993).
9. E. D. Stewart and J.-O. Gong, Phys. Lett. B **510**, 1 (2001).
10. J. Choe, J.-O. Gong, and E. D. Stewart, J. Cosmol. Astropart. Phys. **0407**, 012 (2004).
11. S. Dodelson and E. D. Stewart, Phys. Rev. D **65**, 101301 (2002); E. D. Stewart, Phys. Rev. D **65**, 103 508 (2002).
12. M. Joy, E. D. Stewart, J.-O. Gong, and H.-C. Lee, J. Cosmol. Astropart. Phys. **0504**, 012 (2005).
13. A. A. Starobinsky, Pis'ma Zh. Éksp. Teor. Fiz. **30**, 719 (1979) [JETP Lett. **30**, 682 (1979)].
14. J. Martin and D. Schwarz, Phys. Rev. D **62**, 103520 (2000); D. J. Schwarz and C. A. Terrero-Escalante, J. Cosmol. Astropart. Phys. **0408**, 003 (2004).
15. S. Habib, A. Heinen, K. Heitmann, *et al.*, Phys. Rev. D **70**, 083507 (2004); Phys. Rev. D **71**, 043518 (2005).
16. R. Casadio, F. Finelli, M. Luzzi, and G. Venturi, Phys. Rev. D **71**, 043517 (2005); gr-qc/0506043 (2005).
17. V. F. Mukhanov, Pis'ma Zh. Éksp. Teor. Fiz. **41**, 402 (1985) [JETP Lett. **41**, 493 (1985)].

18. A. G. Muslimov, Class. Quantum Grav. **7**, 231 (1990); D. S. Salopek and J. R. Bond, Phys. Rev. D **42**, 3936 (1990).
19. F. Lucchin and S. Matarrese, Phys. Rev. D **32**, 1316 (1985).
20. R. Easther, Class. Quantum Grav. **13**, 1775 (1996).
21. D. Polarski and A. A. Starobinsky, Class. Quantum Grav. **13**, 377 (1996).
22. E. R. Harrison, Phys. Rev. D **1**, 2726 (1970); Ya. B. Zeldovich, Mon. Not. R. Astron. Soc. **160**, 1P (1972).
23. A. Benoit, P. Ade, A. Amblard, *et al.*, Astron. Astrophys. **399**, L25 (2003).
24. C. L. Bennett, M. Halpern, G. Hinshaw, *et al.*, Astrophys. J., Suppl. **148**, 1 (2003).
25. J. D. Barrow and A. R. Liddle, Phys. Rev. D **47**, 5219 (1993).
26. A. D. Rendall, Class. Quantum Grav. **22**, 1655 (2005).
27. A. Vallinotto, E. J. Copeland, E. W. Kolb, *et al.*, Phys. Rev. D **69**, 103519 (2004).
28. A. A. Starobinsky, Pis'ma Astron. Zh. **9**, 579 (1983) [Sov. Astron. Lett. **9**, 302 (1983)].
29. U. Seljak, A. Makarov, P. McDonald, *et al.*, Phys. Rev. D **71**, 103 515 (2005).

JETP Letters, Vol. 82, No. 4, 2005, pp. 174–177. Translated from Pis'ma v Zhurnal Éksperimental'noĭ i Teoreticheskoĭ Fiziki, Vol. 82, No. 4, 2005, pp. 192–195.

Monochromaticity of the Smith–Purcell Optical Radiation Generated by a 75-keV Electron Beam

Yu. N. Adishchev[a], A. V. Vukolov[a], D. V. Karlovets[a], A. P. Potylitsyn[a], and G. Kube[b]

[a] *Tomsk Polytechnic University, pr. Lenina 30, Tomsk, 634034 Russia*
e-mail: vukolov@interact.phtd.tpu.edu.ru
[b] *DESY, 22603 Humburg, Germany*

Received June 16, 2005

The monochromaticity of the Smith–Purcell optical radiation generated by a 75-keV electron beam with a final emittance of $\epsilon = 0.65 \times 10^{-4}$ mm rad that passes over a grating with a period of $D = 0.833$ μm has been analyzed. It has been shown that the monochromaticity of Smith–Purcell radiation is determined not only by the angular aperture of a monochromator but also by the divergence of the electron beam. © *2005 Pleiades Publishing, Inc.*

PACS numbers: 41.60.–m, 41.85.Qg

Free-electron lasers have recently been created and are successfully used to generate intense monochromatic radiation in the infrared and submillimeter ranges [1]. Such free-electron lasers involve an electron beam with an energy on the order of 50–200 MeV that passes through an undulator with a several-centimeter period. A promising scheme is a free-electron laser based on the Smith–Purcell effect, which will provide radiation in the above range on an electron beam with energy below 1 MeV [2]. Smith–Purcell radiation (SPR) is generated when a charged particle passes parallel to the surface of a periodic structure (e.g., diffraction grating). The mechanism of radiation was predicted by Frank [3] and was experimentally observed for the first time by Smith and Purcell [4] in the optical range on a 300-keV electron beam. The intensity of SPR in the optical range was studied in [5–9] on electron beams with energies from 20 keV [9] to 855 MeV [8]. However, the monochromaticity of the radiation has not yet been investigated experimentally.

For a unidirectional electron beam, the position of the line in the radiation spectrum is expressed in terms of the emission angle and grating period through the known dispersion relation [4]

$$\lambda_n = \frac{D}{|n|}\left(\frac{1}{\beta} - \cos\theta\sin\Phi\right), \qquad (1)$$

where λ is the radiation wavelength, D is the grating period, n is the diffraction order, $\beta = v/c$ is the ratio of the electron velocity to the speed of light, and θ and Φ are the emission angles of SPR photons as shown in Fig. 1.

The monochromaticity of SPR for the unidirectional beam at a fixed emission angle of SPR photons is determined by the number N of grating periods:

$$\Delta\lambda/\lambda \approx 1/N.$$

The angular distribution of radiation energy for the nth order is given by the expression [8]

$$\frac{dW_n}{d\Omega} = 2\pi\alpha\hbar c\frac{n^2}{D}N\frac{\sin^2\theta\sin^2\Phi}{\left(\frac{1}{\beta} - \cos\theta\sin\Phi\right)^3} \times |R_n|^2\exp\left(-\frac{4\pi d}{\lambda\beta\gamma}\sqrt{1 + (\beta\gamma\sin\theta\cos\Phi)^2}\right), \qquad (2)$$

where α is the fine structure constant, $|R_n|^2$ is the radiation factor determined by the grating profile, and γ is the Lorentz factor.

The factor $|R_n|^2$ for nonrelativistic electrons is determined by the grating profile and photon emission angles θ and Φ. This quantity is calculated using various models, which give results differing from each other by more than one order of magnitude. For esti-

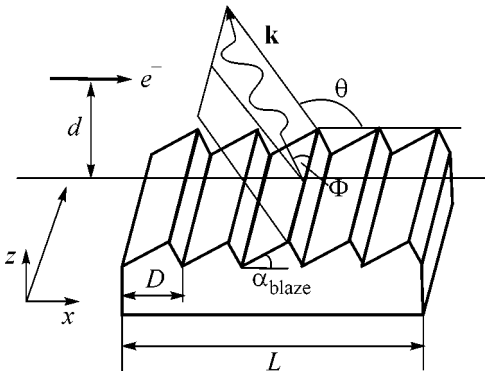

Fig. 1. Scheme of the generation of the Smith–Purcell radiation: **k** is the wavevector, α_{blaze} is the grating-blaze angle, and d is the distance between the electron trajectory and grating (impact parameter).

0021-3640/05/8204-0174$26.00

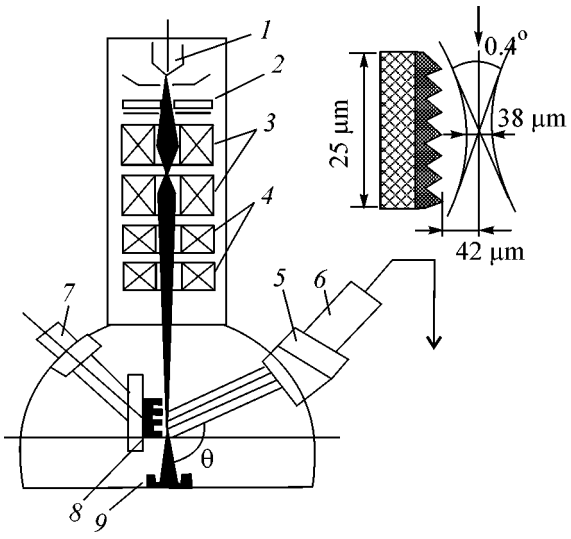

Fig. 2. Geometry of the experiment: (*1*) cathode, (*2*) anode, (*3*) condensers, (*4*) beam-displacement system, (*5*) monochromator, (*6*) photomultiplier tube, (*7*) micrometer screw, (*8*) grating, and (*9*) Faraday cylinder.

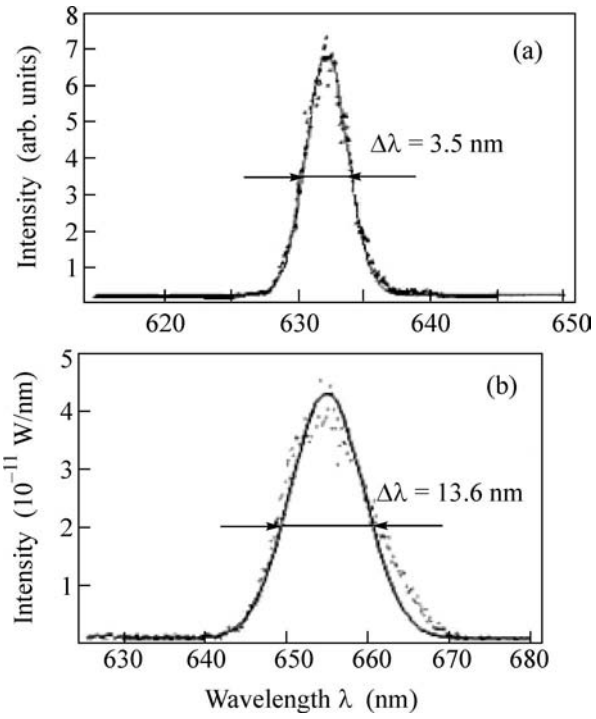

Fig. 3. Emission spectrum of the (a) laser and (b) laser diode.

mates under our experimental conditions, we can take $|R_n|^2 = \text{const} = 1$ according to the Van der Berg model [10]. The intensity of SPR decreases exponentially as the impact parameter d increases. The interaction parameter

$$h_{\text{int}} = \lambda\beta\gamma/4\pi,$$

determines the efficiency of the "coupling" between the beam and grating. In the experiment described in [4], the electron beam size (150 μm) was much larger than the interaction parameter $h_{\text{int}} \approx 0.1$ μm.

The experimental setup for obtaining and studying SPR in the optical range was created on the basis of an EMMA-2 electron microscope. The scheme of the setup is shown in Fig. 2. The electron microscope generates an electron beam with an energy of 25–100 keV and a current of about 1–3 μA. The cross section of the beam in the focus at the diffraction-grating center was $\leq 38 \pm 2$ μm. The distance between the electron beam axis and grating in the focus was approximately equal to 42 μm, which virtually excludes the interaction of the beam particles with the grating. For our experiment, $h_{\text{int}} \approx 0.03$ μm. It is worth noting that the beam diameter in experiments described in [5] and [6] was equal to 200 μm and 5 mm, respectively. The electron energy spread was estimated as $\Delta E/E < 1\%$. The beam emittance, which was measured using the beam sizes at four points and the secondary electron emission current from four movable plates of the charge-sensitive electrometer, was equal to 0.65×10^{-4} mm rad [11]. The plates were moved by means of a micrometer screw, which allowed both the measurement of the beam diameter with a spatial resolution of about 2 μm and the determination of the emittance from a simple geometric construction. The beam divergence was estimated as $\Delta\theta \approx 0.4°$.

A triangular profile grating (see Fig. 1) with a period of 833 nm and an angle of $\alpha_{\text{blaze}} = 26.44°$ was used in the experiment. For the grating length $L = 25$ mm, the number N of periods was approximately equal to 30000. The grating was made of glass and covered by an aluminum coating with a thickness of 700 ± 50 nm. The observation of SPR was performed at an angle of $\theta = 135°$, which corresponds to a radiation wavelength of $\lambda = 745$ nm for $n = 3$ and an electron energy of $E = 75$ keV ($\beta = 0.49$).

The radiation spectrum in the range 500–760 nm was measured in the experiment using an optical monochromator with a photomultiplier tube (PMT) operating in the count regime. The resolution of the monochromator was controlled by the width of the input aperture. For a chosen monochromator aperture width of 2 mm, the resolution was measured using a laser with a wavelength of $\lambda_{\text{las}} = 634$ nm and a linewidth of approximately $\approx 10^{-2}$ nm and was equal to $\Delta\lambda \approx 3.5$ nm ($\Delta\lambda$ is the FWHM of the measured spectrum, see Fig. 3a). To calibrate the optical system, a laser diode ($\lambda = 655$ nm), as well as red ($\lambda = 665$ nm) and blue ($\lambda = 490$ nm) light diodes, is used in addition to the above laser. Figure 3b shows the emission spectrum of the laser diode measured by the monochromator. The laser power was measured by a calorimeter and was equal to 0.37 mW. Two sequential neutral filters attenuate the laser beam by a factor of $k = 1.3 \times 10^{-6}$. For this reason, a PMT with

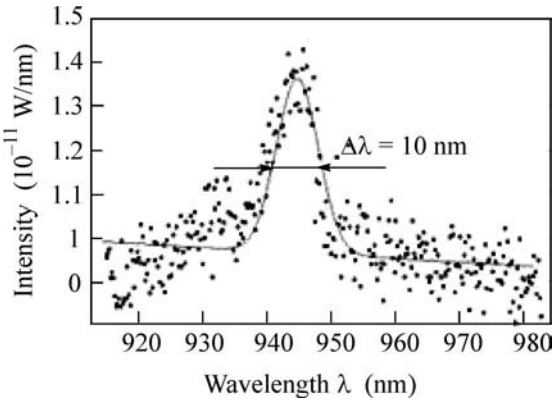

Fig. 4. (Points) Measured spectrum of Smith–Purcell radiation and (solid line) the fit by a Gaussian plus constant background.

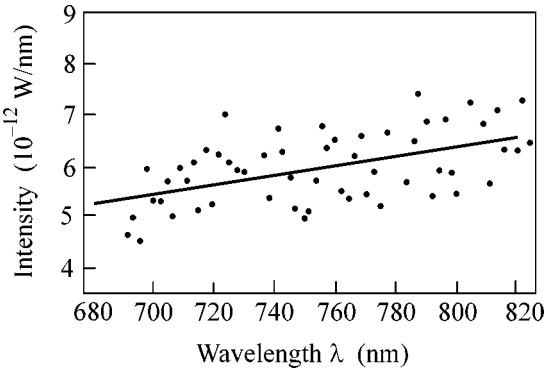

Fig. 5. (Points) Radiation spectrum for the case where the beam touches the grating and (solid straight line) a linear fit.

the same gain as that for the measurement of the SPR spectrum was used as the detector. The measurement results made it possible to obtain the coefficient for recalculation of the number of PMT counts to watts.

For the normal position of the grating ($\Phi = 90°$), we observed a bright peak at a wavelength of $\lambda_3 = 745$ nm, which agrees well with the theory ($\lambda_3^{\text{theor}} = 745.2$ nm), with a width of $\Delta\lambda/\lambda \approx 1.4\%$ (see Fig. 4).

The yield of photons that was calculated taking into account the monochromator aperture and PMT efficiency was approximately equal to $\sim 2 \times 10^{-6}$ photons per electron. For a beam with a current of $I = 1$ μA at an observation angle of $\theta = 130° \pm 1.5°$ and diffraction order $n = 3$, the experimental power of the useful signal (SPR power) was equal to $\Delta P \approx 3.2 \times 10^{-12}$ W.

The solid angle cut by the monochromator aperture and PMT cathode was estimated as $\Delta\Omega = 5 \times 10^{-4}$ in our experiment. Thus, we detected the radiation brightness (the angular distribution of power per unit current, which is proportional to the SPR energy per unit solid angle)

$$\frac{\Delta P}{I\Delta\Omega} = \frac{\Delta W}{\Delta\Omega} = 6.4 \times 10^{-9}\ \text{W/(μA ster)}$$

$$= 6.4 \times 10^{-3}\ \text{eV/(}e\text{ ster)}$$

The total measurement error does not exceed 50%. In the experiment described in [5], the measured power of the SPR for the second diffraction order and the beam with a current of 0.25 μA and an energy of 100 keV was equal to $\Delta P \approx 3 \times 10^{-11}$ W and brightness per unit current was

$$\frac{\Delta P}{I\Delta\Omega} = 16 \times 10^{-9}\ \text{W/(μA ster)}.$$

An SPR power of 34 μW/(cm^2 ster) was obtained in the optical range for a beam with a current of 3 mA and an energy of 120 keV in the experiment described in [6], where a detector scanned a grating area of 0.5 mm^2, which corresponds to the brightness

$$\frac{\Delta P}{I\Delta\Omega} = 5.7 \times 10^{-11}\ \text{W/(μA ster)}.$$

Our result is slightly less than the result obtained in [5], but it is much larger (by approximately two orders of magnitude) than the result obtained in [6].

We carried out an additional experiment in which an electron beam slightly touched the surface in the initial and final sections of the grating, which was accompanied by the observed luminescence of these sections. Figure 5 shows the measured radiation spectrum. In this case, the radiation intensity is much higher, but no lines are observed in the spectrum. Transition radiation with a continuous spectrum is likely generated when the beam touches the grating. The effect of horizontal angular divergence on the position and shape of the SPR line was previously analyzed in [12]. It was shown that the position of the line in the spectrum in this case is determined by the Smith–Purcell formula with the replacement of the grating period D by $D/\cos\Psi$, where Ψ is the angle between the beam-velocity projection onto the grating plane and perpendicular to the "top" of a blaze. In our case, the effects associated with the horizontal divergence of the beam on the lineshape are negligible.

However, the effect of the vertical angular divergence and the finite angular aperture $\Delta\theta$ of the detector on the position and shape of the SPR line is considerable even in the simplest model [13] in which a real grating is represented by a set of ideally conducting strips separated by vacuum gaps. For zero emittance and the aperture $\Delta\theta = 3°$, we estimated the monochromaticity as $\Delta\lambda/\lambda = 0.7\%$. Figure 6 shows the calculation of the SPR line for the out aperture after averaging over the vertical angular distribution, which was approximated by a Gaussian with a variance of $\sigma^2 = 1.96$ mrad^2. According to this figure, the SPR line is

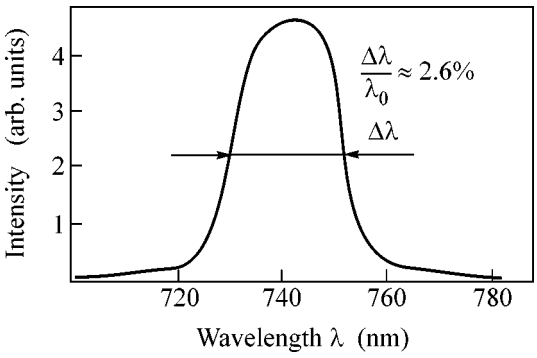

Fig. 6. Shape of the Smith–Purcell radiation line after averaging over vertical emittance for experimental values of the monochromator aperture.

broadened to $\Delta\lambda/\lambda = 2.6\%$. The experiment geometry was chosen such that the particle trajectory touches the grating at its edge for the maximum flight angle $\theta_{0\,\max} = 3\sigma$. The line is broadened due primarily to an increase in the distance between the flying electron and the grating for the nonzero flight angle θ_0. When the electron is spaced from the grating at distances larger than h_{int}, the remaining part of the grating makes almost no contribution; i.e., the SPR line is formed by N_{eff} periods rather than N periods, where the effective number of periods is $N_{\text{eff}} \ll N$ and is determined by the initial section of the grating. Using the experimental linewidth, we estimate the effective number of periods that make a contribution to the SPR line as $N_{\text{eff}} \approx \lambda/\Delta\lambda \approx 70$.

The broadening of the SPR was calculated using the simplest SPR model in which the real grating profile was disregarded. However, this approximation yields a value close to the experimental value, which makes it possible to obtain semiquantitative estimates for the inclusion of the effect of the finite beam emittance on the characteristics of SPR. In turn, this circumstance enables one to use the results to estimate the possibility of creating a new type of free-electron lasers based on SPR [7], where the monochromaticity of the spectral line is determining.

REFERENCES

1. W. B. Colson, Nucl. Instrum. Methods Phys. Res. A **375**, 669 (1996).
2. A. Friedman, A. Gover, G. Kurizki, *et al.*, Rev. Mod. Phys. **60**, 471 (1988).
3. M. Frank, Izv. Akad. Nauk SSSR, Ser. Fiz. **6**, 3 (1942).
4. S. J. Smith and E. M. Purcell, Phys. Rev. **92**, 1069 (1953).
5. A. Gover *et al.*, J. Opt. Soc. Am. B **1**, 723 (1984).
6. I. Shih *et al.*, J. Opt. Soc. Am. B **7**, 345 (1990).
7. J. Urata, M. Goldstein, M. F. Kimmitt, *et al.*, Phys. Rev. Lett. **80**, 516 (1998).
8. G. Kube, Dissertation (Inst. of Nuclear Physics, Univ. Mainz, Germany, 1998).
9. H. Ishizuka *et al.*, Nucl. Instrum. Methods Phys. Res. A **445**, 276 (2000).
10. P. M. Van den Berg, J. Opt. Soc. Am. **63**, 1588 (1973).
11. Yu. N. Adishchev, A. V. Vukolov, and A. P. Potylitsyn, Izv. Tomsk. Politekh. Univ., Fiz. **307** (6), 48 (2004).
12. O. Haeberle, P. Rullhusen, J.-M. Salome, and N. Maene, Phys. Rev. E **55**, 4675 (1997).
13. A. P. Potylitsyn, P. V. Karataev, and G. A. Naumenko, Phys. Rev. E **61**, 7039 (2000).

Translated by R. Tyapaev

JETP Letters, Vol. 82, No. 4, 2005, pp. 178–180. Translated from Pis'ma v Zhurnal Éksperimental'noĭ i Teoreticheskoĭ Fiziki, Vol. 82, No. 4, 2005, pp. 196–199.

100-TW Femtosecond Laser Based on Parametric Amplification

V. V. Lozhkarev[a], S. G. Garanin[b], R. R. Gerke[c], V. N. Ginzburg[a], E. V. Katin[a], A. V. Kirsanov[a], G. A. Luchinin[a], A. N. Mal'shakov[a], M. A. Mart'yanov[a], O. V. Palashov[a], A. K. Poteomkin[a], N. N. Rukavishnikov[b], A. M. Sergeev[a], S. A. Sukharev[b], G. I. Freĭdman[a], E. A. Khazanov[a], A. V. Charukhchev[d], A. A. Shaĭkin[a], and I. V. Yakovlev[a]

[a] *Institute of Applied Physics, Russian Academy of Sciences, ul. Ul'yanova 46, Nizhni Novgorod, 603950 Russia*
e-mail: khazanov@appl.sci-nnov.ru

[b] *Russian Federal Nuclear Center VNIIEF, pr. Mira 37, Sarov, Nizhni Novgorod region, 607188 Russia*

[c] *ZAO KholoGréĭT, St. Petersburg, 190068 Russia*

[d] *Research Institute for Complex Testing of Optoelectronic Devices and Systems, Sosnovy Bor, Leningrad region, 188540 Russia*

Received June 20, 2005

In experiments on the parametrical amplification of femtosecond pulses in wide-aperture DKDP crystals, a power of more than 100 TW has been reached, which is much higher than the record level achieved in such lasers. The energy efficiency obtained for the parametric amplifier is equal to 27%. The energy of a 72-fs pulse is equal to 10 J. © *2005 Pleiades Publishing, Inc.*

PACS numbers: 42.65.–k

Petawatt power was reached for laser radiation already in 1997 [1] using the amplification of chirped pulses in neodymium glass. To date, this level has been achieved only in three laboratories in the world [1–3]. A further increase in the power is fundamentally limited by the narrow gain band of neodymium glass and the low optical stability of diffraction gratings. The use of parametric amplifiers instead of standard laser amplifiers is one of the most promising ways for overcoming the petawatt power barrier. In such systems, which were first proposed in [4, 5], by choosing a nonlinear crystal, propagation directions, and frequencies of the pump and signal waves, the conditions of broadband matching are realized and, in addition, the principle of sequential extension (chirping), multicascade amplification, and, in addition, the compression of amplified pulses, which is traditional for the generation of superstrong fields is used.

The amplification of femtosecond pulses to petawatt powers in parametric amplifiers requires, first, the kilojoule energy of a pump pulse with a duration of about 1 ns, which makes neodymium glass lasers most promising, second, nonlinear crystals with an aperture of 30 cm or larger, which restricts the choice to only two candidates: the KDP and DKDP crystals.

The problem of creating parametric amplifiers of femtosecond pulses to multiterawatt and petawatt levels was discussed and experimentally studied in [6–10]. In those works, KDP crystals were considered as nonlinear elements in the last cascades of parametric amplifiers. In these crystals, upon pumping by the radiation of the second harmonic of a neodymium-glass laser (pump wavelength of 527 nm), the maximum width of the gain band is reached close to degenerate interaction (signal wavelength of about 1054 nm). In [11, 12], we proposed to use nondegenerate parametric amplification in the DKDP crystal, which, in contrast to the KDP crystal, is transparent to about 1.4 μm [13]. Moreover, as was shown in [12, 14], for the central wavelength of 910-nm signal radiation, the ultrabroadband phase matching is realized in the DKDP crystal, which makes it possible to amplify pulses with a duration of 10–15 fs. As driven femtosecond generators, lasers operating at the wavelength of 910-nm signal radiation (sapphire with titanium) or 1250-nm idler radiation (forsterite with chromium) can be used. As was shown in [15], the latter variant is promising. More recently, a 0.44-TW laser was created [14, 16]. This laser is a start system for a 100-TW laser complex described in this paper.

Figure 1 shows the scheme of the 100-TW laser complex with a Cr: forsterite laser emitting 45-fs pulses with an energy of 3 nJ (central wavelength of 1250 nm) as a master oscillator. We used an original stretcher (passband of 1000 cm^{-1}), which contained two prisms in addition to ordinary diffraction gratings, which made it possible to efficiently compress a 600-ps pulse with a wavelength of 910 nm by means of a usual compressor [14, 16].

The second harmonic of a single-mode single-frequency Nd:YLF laser with a wavelength of 527 nm, energy up to 1 J in a 1.5-ns pulse, and a pulse repetition frequency of 2 Hz is used as the pumping of the first two parametric amplifiers. A fraction of the radiation of

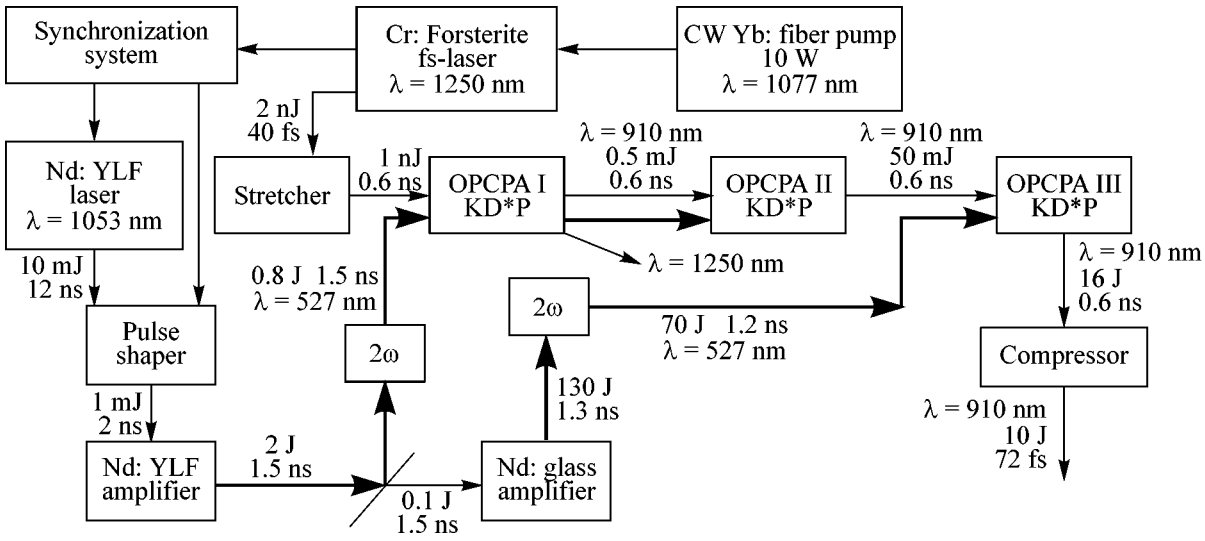

Fig. 1. Scheme of the 100-TW laser complex based on the parametric amplification of chirped pulses.

the fundamental harmonic of this laser is directed through a multistep spatial filter [16, 17] to the input of a five-cascade amplifier based on phosphate neodymium glass. The amplifier worked with a period of one pulse per 30 min and ensured the output energy of 70 J of a second-harmonic pulse with a duration of 1.2–1.5 ns for a beam diameter of 10 cm. The divergence of the output radiation was equal to three diffraction limits, which satisfies the requirement imposed on the pump radiation of the third parametric amplifier. The pumping system of all parametric amplifiers was described in detail in [18] and its synchronization with the femtosecond driving generator was discussed in [19].

The first parametric amplifier was two-pass. It performed the wide-band transformation of 1250-nm chirped pulses into 910-nm signal pulses at the first pass and amplified the 910-nm radiation at the second pass. After the second amplifier, the pulse energy reached several tens of millijoules. The adjustment procedure, as well as spectral, angular, and energy characteristics of the first two parametric amplifiers (terawatt power), was described in detail in [14].

The third parametric amplifier (a noncoated DKDP crystal 65 mm in length with a clear aperture of 100 mm) had a weak-signal amplification factor of 1500 for a pumping energy of 50 J. For an input signal of several tens of millijoules, these parameters ensured the deep saturation of the parametric amplification. The energy of 16 J of the chirped pulse at the input of the compressor was reached due to saturation and the high quality of the pump beam, see Fig. 2. The maximum physical energy efficiency of the parametric amplifier was equal to 27%. The radiation spectrum was not narrowed.

To compress the pulse, we used a vacuum compressor based on two diffraction gratings and one angular reflector with a pure aperture of 110 mm. The transmission coefficient of the compressor was equal to 65%. The remote adjustment system ensured the adjustment of all the optical elements of the compressor with an accuracy of five angular second. Neither narrowing of the spectrum nor angular chirp is observed in the output radiation. The maximum energy of the compressed pulses was equal to 10 J. Figure 3 shows the autocorrelation function. It corresponds to a Lorentz pulse with an FWHM of 72 fs. Thus, the peak power at the output of the femtosecond laser complex based on the parametric amplification of chirped pulses was equal to 130 TW, which is eight times higher than the record

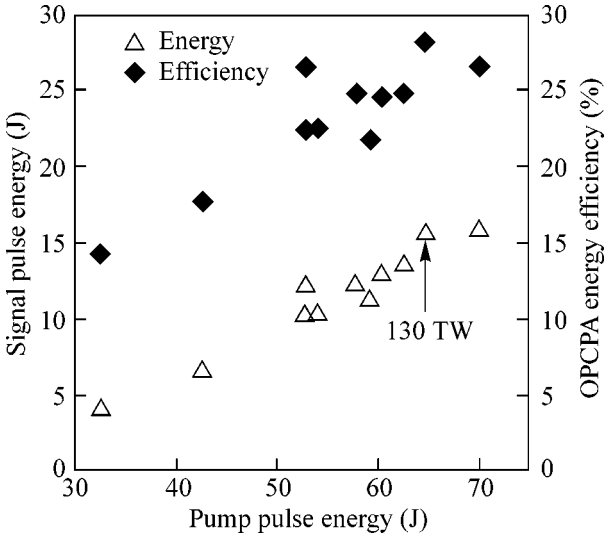

Fig. 2. (Triangles) Signal pulse energy at the input of the compressor and (diamonds) the energy efficiency of the parametric amplifier vs. the pump pulse energy.

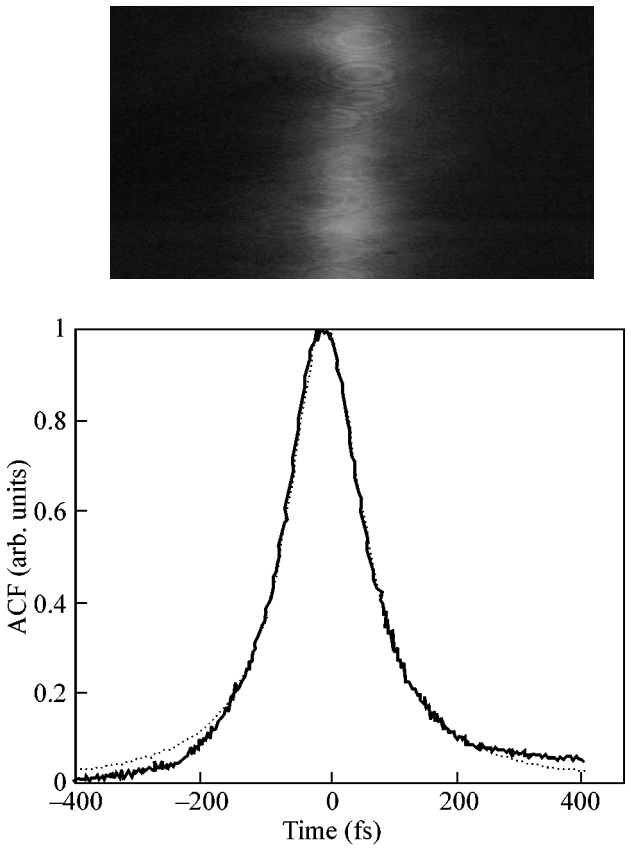

Fig. 3. (Solid line, photo) Autocorrelation function at the output of the 100-TW laser and (dotted line) the Lorentz curve for a pulse with a half-maximum duration of 72 fs.

level reached in lasers with the parametric amplification of chirped pulses [9].

Thus, 100-TW peak power has been reached experimentally with the architecture of the high-power femtosecond lasers that we proposed previously. Calculations show that, in order to reach multipetawatt power, an additional parametric amplifier with an aperture of 200–300 mm and a pump energy of 1–2 kJ at a wavelength of 527 nm is necessary. A DKDP crystal for such an amplifier has been grown at the Institute of Applied Physics, Russian Academy of Sciences (Nizhni Novgorod, Russia), and a pump laser exists at the Russian Federal Nuclear Center VNIIEF (Sarov): it is one of the channels of the Luch setup based on neodymium phosphate glass [20]. At present, a multipetawatt laser source is under development on this basis.

This work was supported by the Council of the President of the Russian Federation for Support of Young Russian Scientists and Leading Scientific Schools (project no. NSh-1625.2003.2), the Presidium of the Russian Academy of Sciences (program “Femtosecond Optics and the Physics of Superstrong Laser Fields”), and the Division of Physical Sciences, Russian Academy of Sciences (program “Nonlinear Optics of Unique Laser Systems”).

REFERENCES

1. D. M. Pennington, M. D. Perry, B. C. Stuart, *et al.*, Proc. SPIE **3047**, 490 (1997).
2. Y. Kitagawa, Y. Sentoku, S. Akamatsu, *et al.*, Phys. Plasmas **9**, 2202 (2002).
3. C. B. Edwards, J. C. Aldis, R. Allot, *et al.*, Proc. SPIE **4948**, 444 (2003).
4. A. Piskarskas, A. Stabinis, and A. Yankauskas, Usp. Fiz. Nauk **150**, 127 (1986) [Sov. Phys. Usp. **29**, 869 (1986)].
5. A. Dubietis, G. Jonusauskas, and A. Piskarskas, Opt. Commun. **88**, 437 (1992).
6. I. N. Ross, P. Matousek, M. Towrie, *et al.*, Opt. Commun. **144**, 125 (1997).
7. P. Matousek, B. Rus, and I. N. Ross, IEEE J. Quantum Electron. **36**, 158 (2000).
8. I. N. Ross, J. L. Collier, P. Matousek, *et al.*, Appl. Opt. **39**, 2422 (2000).
9. X. Yang, Z. Xu, Y. Leng, *et al.*, Opt. Lett. **27**, 1135 (2002).
10. O. Chekhlov, J. L. Collier, I. N. Ross, *et al.*, in *Proceedings of Conference on Lasers and Electro-Optics, CLEO-2005* (Baltimore, Maryland, 2005), JFB3.
11. G. Freidman, N. Andreev, V. Bespalov, *et al.*, in *Proceedings of Conference on Lasers and Electro-Optics, CLEO-2002* (Long Beach, California, 2002), Postdeadline Papers, CPDA9-1.
12. G. Freidman, N. Andreev, V. Ginzburg, *et al.*, Proc. SPIE **4630**, 135 (2002).
13. V. I. Bespalov, I. A. Batyreva, L. A. Dmitrenko, *et al.*, Kvantovaya Élektron. (Moscow) **4**, 1563 (1977).
14. V. V. Lozhkarev, G. I. Freidman, V. N. Ginzburg, *et al.*, Laser Phys. **15** (2005).
15. G. Freidman, N. Andreev, V. Bespalov, *et al.*, Proc. SPIE **4972**, 90 (2003).
16. N. F. Andreev, V. I. Bespalov, V. I. Bredikhin, *et al.*, Pis’ma Zh. Éksp. Teor. Fiz. **79**, 178 (2004) [JETP Lett. **79**, 144 (2004)].
17. A. K. Poteomkin, E. V. Katin, E. A. Khasanov, *et al.*, in *Proceedings of Advanced Solid-State Photonics Meeting* (Vienna, 2005), TuB42.
18. A. K. Potemkin, E. V. Katin, A. V. Kirsanov, *et al.*, Kvantovaya Élektron. (Moscow) **35**, 302 (2005).
19. E. V. Katin, V. V. Lozhkarev, O. V. Palashov, and E. A. Khazanov, Kvantovaya Élektron. (Moscow) **33**, 836 (2003).
20. S. G. Garanin, A. I. Zaretskiĭ, R. I. Il’kaev, *et al.*, Kvantovaya Élektron. (Moscow) **35**, 299 (2005).

Translated by R. Tyapaev

JETP Letters, Vol. 82, No. 4, 2005, pp. 181–184. From Pis'ma v Zhurnal Éksperimental'noĭ i Teoreticheskoĭ Fiziki, Vol. 82, No. 4, 2005, pp. 200–203.

Chaotic Tunneling in a Laser Field¶

V. L. Golo and Yu. S. Volkov

Faculty of Mechanics and Mathematics, Moscow State University, Moscow, 119899 Russia

e-mail: golo@mech.math.msu.su

Received July 7, 2005

We study the driven tunneling of a one-dimensional charged particle confined to a rectangular double well. The numerical simulation of the Schrödinger equation based on the Cranck–Nicholson finite-difference scheme shows that the modulation of the amplitude of the external field may result in parametric resonance. The latter is accompanied by the breakdown of the quasi-periodic motion characteristic of the usual driven tunneling and the emergence of irregular dynamics. We describe the above breakdown with the occupation probability for the ground state of the unperturbed system and create the visualization of the irregular dynamics with the help of Shaw–Takens' reconstruction of the state space. Both approaches agree concerning the values of the resonant frequency for the parametric excitation. Our results indicate that the shape of the laser pulse could be essential for generating chaotic tunneling. © *2005 Pleiades Publishing, Inc.*

PACS numbers: 03.65.–w

1. Driven transitions in a double well are instrumental for studying the tunneling in various fields of physics and chemistry [1, 2]. Considerable attention has been drawn to the tunneling dynamics in the presence of a driving force with a time dependent amplitude. In his seminar paper [3], M. Holthaus showed that shaping the driving force may be instrumental in controlling the tunneling in a bistable potential. In particular, it was shown in [3] that, by choosing an appropriate envelope for a laser pulse, one may perform population transfer on time scales much shorter than the base tunneling time. This situation is intimately related to the problem of quantum chaos, which is generally approached within the framework of the quasi-classical approximation and Gutzwiller's theory. In fact, classical chaotic systems are often used as a clue to quantum ones. In contrast, it would be very interesting to look at quantum chaos the other way around and consider systems that need studying without approximations that could have bearing upon classical mechanics, for example, particles confined to potentials of a size comparable with the de Broglie wave length. This is additionally interesting owing to the fact that calculations within the framework of semiclassical theory should depart from the quantum ones on the time scale of $\hbar/\Delta E$ with ΔE being the typical spacing between energy levels. Therefore, the Schrödinger equation describing the problem needs numerical studying.

This letter aims at the theoretical description of the tunneling transitions for a charged particle in a one-dimensional rectangular double-well potential $U(x)$ and an external periodic field $V(t)$ that mimics electromagnetic irradiation. The Hamiltonian of the system in dimensionless units is given by the equation

$$H = \frac{1}{2}\hat{p}^2 + U(x) + V(t)$$

in which the potential U reads

$$U = \begin{cases} -U_1, & a \le x \le b \\ -U_2, & c \le x \le d, \\ 0, & \text{otherwise} \end{cases} \qquad (1)$$

i.e., the unsymmetrical double well comprising the two shafts of different depths U_1, U_2 (see Fig. 1). The shape of U is chosen in such a way that the values of the wave functions $\psi_0(x, t) = \langle x|0\rangle$, $\psi_1(x, t) = \langle x|1\rangle$ of the ground and the first excited state are very small outside the right and the left shafts of the well, respectively (see Fig. 1). Consequently, the particle's transitions $|0\rangle \rightleftharpoons |1\rangle$ can be visualized as tunneling ones. The field frequency Ω verifies the constraint of the resonance, which in dimensionless units reads $\Omega = E_1 - E_0$, where E_0, E_1 are the energies of the ground and the first excited states. The external field $V(t)$ has the form

$$V(t) = -A\sin(\Omega t)\hat{p}, \quad \hat{p} = -i\partial_x,$$

where $\hat{p}$ is the operator of momentum corresponding to an electromagnetic wave described by the vector potential $A_x = A_z = 0$, $A_y = A\sin\Omega(t - x/c)$ with the scalar potential ϕ being equal to zero [5]. In what follows, we neglect the dependence of A on x since the wavelength is assumed to be much larger than the well's size.

We are looking for regimes in which the regular tunneling breaks down and becomes chaotic. The main

¶ The text was submitted by the authors in English.

0021-3640/05/8204-0181$26.00 © 2005 Pleiades Publishing, Inc.

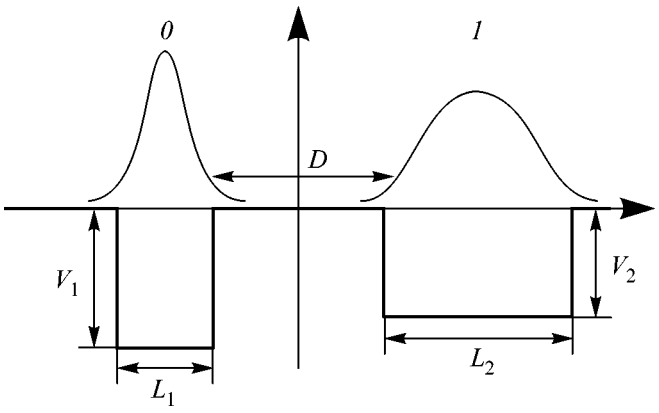

Fig. 1. Rectangular one-dimensional double-well potential. Lines *0* and *1* indicate the moduli of the wave functions $|\psi_0(x, t)|$ and $|\psi_1(x, t)|$ of the ground and the first excited states. In the chosen configuration, $D = 0.876$ is the distance between the wells; $L_1 = 2.337$, $L_2 = 2.045$ are the widths; and $V_1 = 13.82$, $V_2 = 11.91$ are the depths of the shafts in dimensionless units.

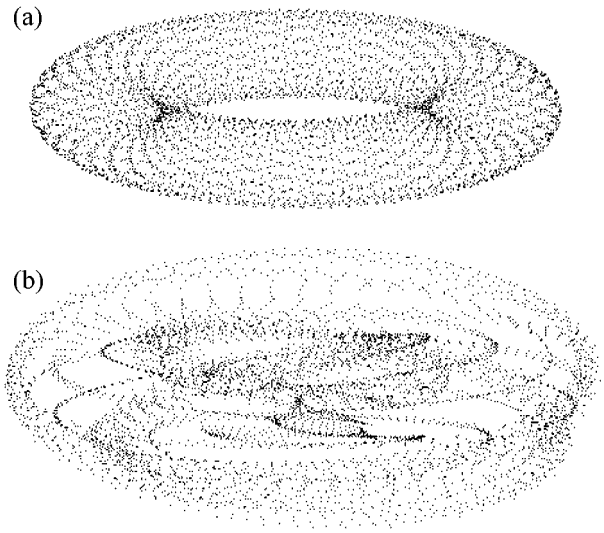

Fig. 2. Visualization of the state space. (a) No parametric excitation, (b) parametric excitation: $A_0 = 0.3$, $\epsilon = 0.1$, $\omega = 0.01755$. The lag time is 330 in both cases.

technique employed for this is the Shaw–Takens (ST) method [4] for reconstructing the state space of a system from a stream of data obtained with the numerical integration of the Schrödinger equation by embedding it in a phase space of enough dimension $\mathcal{D}$; in our case $\mathcal{D} = 3$. The important thing is that one may monitor the dynamics of driven tunneling by using the occupation probability N_0 of the ground state of the unperturbed system

$$N_0 = |\langle 0|\psi\rangle|^2,$$

where $|0\rangle$ and $|\psi\rangle$ are the ground vector and the state vector of the system at the moment of time t, respectively. To obtain the visualization, we shall form a time series that comprises the values of N_0 at the moments of time $n\tau$, $n = 0, 1, 2, \ldots$, with τ being the lag time, so that $N_{0k} = N_0(k\tau)$, $k = 1, 2, 3, \ldots$. Then, the series of vectors $Y_k = (N_{0k}, N_{0k+1}, N_{0k+2})$, $k = 0, 1, 2, 3, \ldots$, serves as a 3d visualization of the state space for the given problem. In particular, we can observe the transition from the regular motion characteristic of the unperturbed resonant motion to the irregular one generated by a parametric excitation given by Eq. (2) below (see Fig. 2).

2. The parametric excitation of the system is generated by the modulation of the amplitude A of the vector potential

$$A = A_0[1 - \epsilon\sin(\omega t)]. \qquad (2)$$

The approximate expression for the frequency of the parametric resonance caused by Eq. (2) can be obtained by employing the rotating wave approximation [5] after some analytical calculations. It reads

$$\omega_{\text{prm}} = A\kappa, \quad \kappa = |\langle 0|\hat{p}|1\rangle|. \qquad (3)$$

In fact, the actual resonant frequency ω_{prm} differs from that given above, and its calculation requires some numerical work.

3. The visualization with the help of the ST method gives a torus in 3d space, which is fairly well drawn and changes in the lag-time, thus, resulting only in continuous deformations of the picture with no sudden modifications being observed (see Fig. 2). In contrast, in the case of a parametric excitation at a frequency close to the value given by Eq. (3) being present, the choice of the lag time is very important for obtaining a meaningful visualization. The break down of the quasi-periodic motion by the resonant parametric excitation is shown in Fig. 2. It is to be noted that the visualization depends on a number of premises; first of all, on the value of the lag time τ and the dimension d of the visualization window. A wise choice of τ is dictated by the characteristic times of the motion under investigation, so that, for certain values of τ, the visualization picture is coherent enough, whereas, for others, it is not meaningful. Therefore, using the ST method, one has to compare pictures obtained for different values of the lag time.

4. We may look at our problem the other way around. Consider sets of the system's states $\mathcal{F}_{kk+1}$, $k = 1, 2, \ldots, \mathcal{N}$, where $\mathcal{N}$ is large enough, given by the constraints

$$\Delta_k \le N_0 \le \Delta_{k+1}, \qquad (4)$$

where Δ_k are intervals dividing the segment $0 \le N_0 \le 1$ in $\mathcal{N}$ equal parts. Take a sufficiently large period of time

T and consider the times τ_k spent by the system in the sets of states $\mathcal{F}_{kk+1}$, that is, where Eq. (4) is verified. We shall define the visiting frequencies as

$$\nu_{kk+1} = \tau_k/T.$$

One may cast ν_{kk+1} in the form of the probability density, $\xi(N_0)$, for the distribution of N_0 by assuming that all the intervals $\Delta_{k+1} - \Delta_k$ are of equal size Δ and by defining

$$\xi(N_0) = \nu_{kk+1}/\Delta.$$

On considering the limit of ξ as $\mathcal{N} \longrightarrow \infty$, we shall obtain the probability density $\xi(N_0)$ (see Fig. 3).

To put it in a quantitative analytical form, we may consider the characteristic function $\chi_{ab}(x)$= 1 if $a \le x \le b$ and 0 otherwise and introduce the quantity

$$\nu_\phi(a, b) = \lim_{T\to\infty}\left\{\frac{1}{T}\int_{-T/2}^{+T/2}\chi_{ab}(N_0)dt\right\}, \qquad (5)$$

so that ν_{ab} can be considered as the frequency of visiting a region of states determined by the constraint $a \le N_\phi \le b$.

The important point is that the limit indicated in the above equation does exist in the context of the problem under investigation. To see this fact, we shall employ the normalization of wave functions in a finite box; that is, our system will be confined to a rectangular potential of infinite depth of a size much larger than the double well's size. Then, the system has the discrete spectrum of eigenvalues, and the characteristic function $\chi_{ab}(N_0)$ can be expanded in Fourier series; the time averaging in the above equation results in canceling out terms oscillating in time, so that the limit exists. The use of the finite box normalization is also important for managing the numerical simulation. The finite integration mesh, or basis, results in reflection of the wave packet that distorts the time evolution of the packet is assumed to be known. By imposing the finite box normalization, we use the physical framework that appears to be compatible with the tunneling dynamics in the double well of a size much smaller than the box and enables us to overcome the numerical artifacts.

It is worth noting that the construction of visiting frequencies is analogous to that of the dwell time that is aimed at studying the localization of wave packets and defined by the equation [6, 7],

$$\tau_D(a, b) = \int_{-\infty}^{+\infty} dt\int_a^b |\psi(x, t)|^2 dx.$$

The probability density ξ indicates that, at the resonant frequency ω_{prm}, the character of the system's motion undergoes a drastic change (see Fig. 3). At this point, it should be noted that the frequency of the parametric resonance ω_{prm}, which can be found by comparing the sizes of the peaks in Fig. 3 for different values of ω in Eq. (2), differs by approximately 5% from the value given by the rotation wave approximation (3). The resonant value corresponds to the most pronounced breakdown of the twin peaks, which correspond to the ground and the first excited state of the free system.

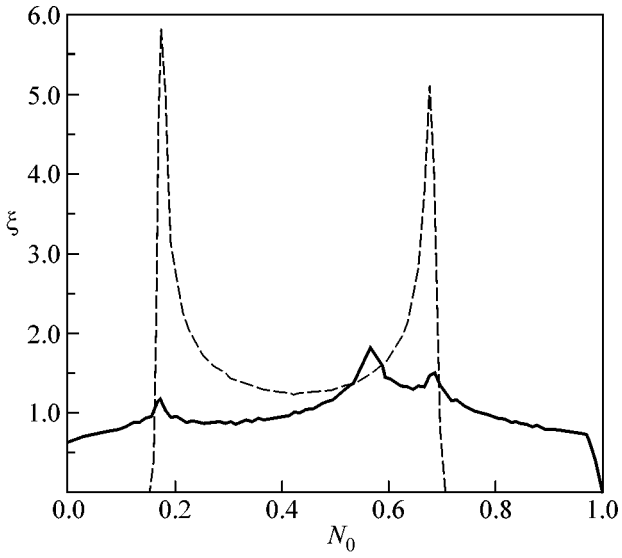

Fig. 3. Probability density ξ for the distribution of N_0 with $A_0 = 0.3$; six bound states (levels confined to the well). The dashed line corresponds to no parametric excitation. The solid line corresponds to parametric excitation with $\epsilon = 0.1$, parametric frequency $\omega = 0.01755$ close to the resonant one, ω_{prm}.

5. In conclusion, we should like to note that, as follows from Eq. (2) for the amplitude of the driving force, the pulse V has a triplet structure determined by the main contribution at the frequency $\Omega = E_1 - E_0$ and two satellites at $\Omega \pm \omega_{prm}$ of less amplitude owing to the equation for $A(t)$ given by Eq. (2)

$$A(t) = A_0\kappa\sin\Omega t - \frac{1}{2}A_0\kappa\epsilon\cos[(\Omega - \omega_{prm})t]$$
$$+ \frac{1}{2}A_0\kappa\epsilon\cos[(\Omega + \omega_{prm})t].$$

The triplet structure could generally have an important bearing on the tunneling in the double-well potential. In fact, if a monochromatic pulse at the resonant frequency $\Omega = E_1 - E_0$ is employed, there is no parametric excitation and the dynamics of the occupation probability have the usual form. In contrast, a poor quality non-monochromatic pulse may contain the triplet $\Omega \pm \omega_{prm}$, so that the deformation of the tunneling dynamics and the emergence of the chaotic motion become possible. It is worth noting that the amplitude of the driving force A_0 can be small so that the frequency shift determined by ω_{prm} may be minuscule.

This work was supported by the Council of the President of the Russian Federation for Support of Young Scientists and Leading Scientific Schools (project no. NSh-1988.2003.1 and the Russian Foundation for Basic Research (project nos. 01-01-00583, 03-02-16173, 04-04-49645).

REFERENCES

1. D. T. Monteiro, S. M. Owen, and D. S. Saraga, Philos. Trans. R. Soc. London, Ser. A **357**, 1359 (1999).
2. M. Grifoni and P. Hänggi, Phys. Rep. **304**, 229 (1998).
3. M. Holthaus, Phys. Rev. Lett. **69**, 1596 (1992).
4. N. H. Packard, J. P. Crutchfield, J. D. Farmer, and R. S. Shaw, Phys. Rev. Lett. **45**, 712 (1980).
5. M. O. Scully and M. S. Zubairy, *Quantum Optics* (Cambridge Univ. Press, Cambridge, 1999), Chap. 5.
6. M. Büttiker, Phys. Rev. B **27**, 6178 (1983).
7. H. M. Nussenzveig, Phys. Rev. A **62**, 042 107 (2000).

JETP Letters, Vol. 82, No. 4, 2005, pp. 185–187. Translated from Pis'ma v Zhurnal Éksperimental'noĭ i Teoreticheskoĭ Fiziki, Vol. 82, No. 4, 2005, pp. 204–206.

Ultraviolet Flashes in the Equatorial Region of the Earth

G. K. Garipov[a], M. I. Panasyuk[a], V. I. Tulupov[a], B. A. Khrenov[a], A. V. Shirokov[a], I. V. Yashin[a], and H. Salazar[b]

[a] *Skobel'tsyn Institute of Nuclear Physics, Moscow State University, Vorob'evy gory, Moscow, 119992 Russia*

[b] *University of Puebla, Puebla, Mexico*

Received June 15, 2005

Intense ultraviolet flashes with a duration of 1 to 64 ms have been detected by the UV detector (wavelengths 300–400 nm) that operates at the *Universitetsky-Tatiana* MSU satellite. Most flashes occur in the equatorial region of the Earth. The nature of the observed flashes is discussed. © *2005 Pleiades Publishing, Inc.*

PACS numbers: 51.50.+v, 92.60.Pw

1. DETECTOR OF THE UV RADIATION OF THE EARTH'S ATMOSPHERE

The scientific equipment of the *Universitetsky-Tatiana* MSU microsatellite (circular orbit with an inclination of 82° and an altitude of 950 km) includes a UV detector [1], which is a photomultiplier tube (PMT) with a multialkali cathode on UV glass. A UFS-1 filter 2.5-mm thick that cuts light with wavelengths longer than 400 nm was mounted at the entrance window of the PMT. For wavelengths less than 300 nm, the detection efficiency decreases due to a decrease in the quantum efficiency of the PMT and light absorption in the atmosphere. For wavelengths of 300–400 nm, the quantum efficiency of the cathode is equal to 20%. The R1463 PMT has a high energy resolution and makes it possible to separate a signal from a single photoelectron. Before the beginning of operation, the signal from a single photoelectron was measured as a function of the voltage on the divider of the PMT. This characteristic is used for determining a UV signal in the number of photoelectrons from the digital value of the signal for a known voltage on the PMT. Knowing the quantum efficiency of the cathode, one may pass from the signal magnitude in the number of photoelectrons to the signal magnitude in the number of photons with the wavelength in a given range. A collimator at the entrance of the PMT determines the geometric factor of the detector: field of view 0.25 rad (the circle diameter in the observed atmosphere is equal to about 250 km), a PMT-cathode working area of 0.4 cm^2, and an aperture of 0.02 cm^2 sr.

The main feature of the operation of the detector is the use of a digital oscilloscope for obtaining the time profile of the UV signal. The time sample and signal integration time change according to the formulated goal. One of the goals of the detector is the selection of UV flashes in the atmosphere. For their selection and the measurement of the time profile of UV flashes, two variants of the digital oscilloscope were applied: first, with a sweep length of 4 ms and time sample of 16 μs and, second, with a sweep length of 64 ms and time sample of 256 μs. The intensity of UV radiation is determined from the recording of two codes: the code M of the high voltage on the PMT and the code N of the analog-to-digital converter (ADC). The limited capabilities of the satellite for transmission of data to the control center force us to choose only one brightest flash over the satellite turn in each of two ranges of their duration.

2. DETECTION OF UV FLASHES

To date, the data obtained from February to April 2005 on Earth's nightside for 91 turns of the satellite have been analyzed. Flashes with a signal magnitude much higher than noise are detected in almost every turn of the satellite. Forty-five flashes with durations of 1–4 ms and 38 flashes with durations of 10–64 ms were detected. Figure 1 shows the typical oscillograms of the flashes. Owing to the condition of the selection of the one largest signal in each turn, the amplitudes of many flashes exceed the ADC measurement limit. At the same time, the number of photoelectrons in such flashes can be estimated from the pulse width at the limiting signal value.

From the total number of photoelectrons recorded by the detector in a flash (~10^4 in flashes with durations 1–4 ms and ~10^5 in flashes with durations 10–64 ms), the energy released in the UV range in a flash in the atmosphere is estimated. Considering that UV radiation in the atmosphere is isotropic (fluorescence of excited nitrogen molecules of the atmosphere) and taking into account the geometric factor 3×10^{17} for detecting a flash at a distance of 950 km by a detector with an area of 0.4 cm^2, as well as the quantum efficiency of the PMT and the absorption of photons with wavelengths

0021-3640/05/8204-0185$26.00

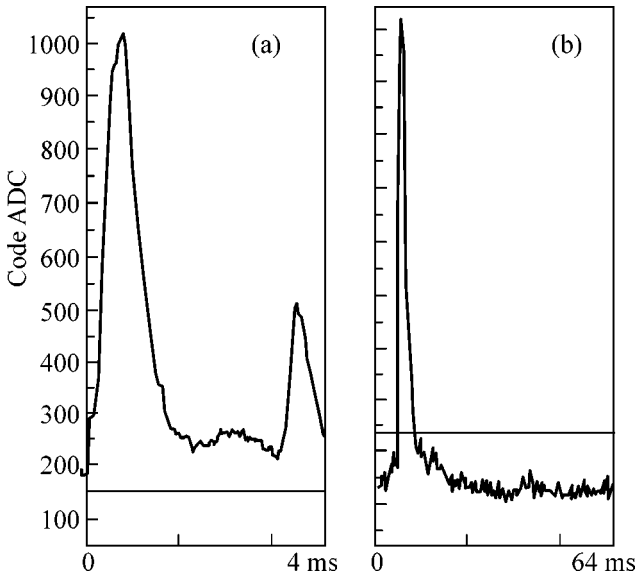

Fig. 1. Oscillogram of UV flashes.

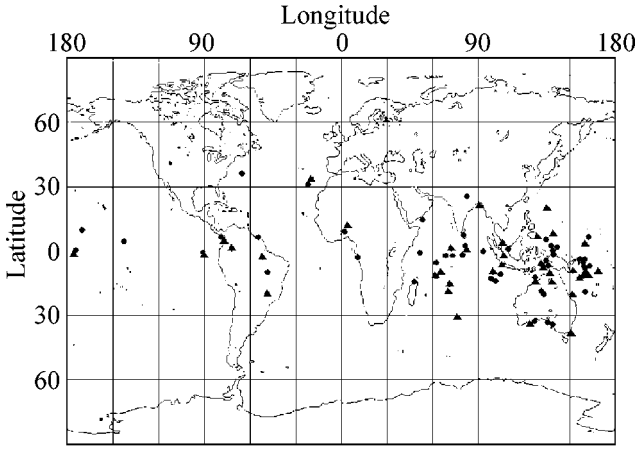

Fig. 2. Map of the geographical coordinates of flashes.

of 300–400 nm in the atmosphere, we determine from the number of detected photoelectrons that 10^{22}–10^{23} photons are emitted during a flash in the atmosphere, which corresponds to UV radiation energy of 10^{11}–10^{12} erg. For the cases where the signal magnitude exceeds the limit value of the dynamic ADC range, estimates provide values on the order of 10^{13} erg (1 MJ).

From the time of the detection of flashes, it is possible to determine the coordinates of the atmospheric region, where a UV flash occurs. The latitudinal and longitudinal distribution of the brightest flashes in each satellite turn is shown in Fig. 2 (note that the nonuniform longitude distribution of the flashes is associated with the operation regime of the scientific equipment of the satellite, which does not work in all turns of the satellite). Among 83 detected flashes, 50 flashes occurred in the equatorial region of the Earth between 10° N and 10° S. For eight cases, the time of the appearance of a flash with a duration of 1–4 ms is close to the time of the detection of flashes with a duration of 10–64 ms, so that the places of both flashes are within the limit ≃400 km. "Noise" flashes separated as flashes with a small amplitude and small duration (at a level required by the control system) are uniformly distributed over the latitudes on which measurements were carried out on the nightside of the Earth from 65° N to 65° S.

3. DISCUSSION OF THE RESULTS

The energy observed for UV flashes and their dominant appearance in the equatorial region of the Earth can be explained under the assumption that they are caused by electric discharges in regions of storm clouds that form a separated belt in the equatorial region. Experimental data on UV flashes that do not include the spectral characteristics of fluorescence are insufficient for final conclusions on the nature of a discharge. At the same time, data on the energy released in the UV range for short flashes make it possible to estimate the most energetically favorable discharge variant. Under the assumption that the observed UV flashes are associated with ordinary intercloud discharges, which slightly emit in the UV range (~0.1% of the total light intensity), the total radiation energy in each flash is expected to be at the gigajoule level. For lightning directed to the ground, the estimate is much higher due to the strong absorption of UV radiation under clouds. If the observed UV flashes are attributed to the actively discussed new type of discharge in the atmosphere between clouds and the ionosphere (sprites, blue jets), the estimate of the energy in the discharge is much lower. Gurevich and Zybin [2] reviewed both the theory of their development and experimental works on the observation of these discharges in the atmosphere. The parameters of the UV flashes observed in this work—the duration on the order of several milliseconds and energy released in fluorescent UV glow on the order of 10^{12}–10^{13} erg—are consistent with the parameters presented in [2]. It is also interesting that the time profiles of the detected flashes virtually coincide with the profiles of sprites obtained on the *EXL98* aircraft and at the Jelm Mountain station (data were presented in [3]). Relativistic electrons with minimum ionization losses (breakdown on runaway electrons), which efficiently excite the UV fluorescence of nitrogen molecules of the atmosphere, play the main role in the development of sprite discharges. A necessary condition for the initiation of a discharge is the presence of a high electric field in the region of the discharge development. According to much experimental evidence, the electric field between clouds and the ionosphere is particularly high in the equatorial region of the Earth, which possibly increases the dominance of the appearance of UV

flashes in the equatorial region. An additional necessary condition for the initiation of breakdown on runaway electrons is a high density of "seed" electrons at the onset of the breakdown. Gurevich *et al.* [4] showed that a sufficient number of seed electrons are created by an extensive air shower (EAS) with a large number of secondary electrons. Using the TUS and KLPVE orbital detectors [5, 6], one can hope to detect an EAS created by an ultrarelativistic cosmic-ray particle (energy higher than 10^{19} eV) before a sprite discharge is developed in the atmosphere. The data obtained from the *Universitetsky-Tatiana* satellite make it possible to design such a methodically difficult experiment involving the TUS and KLYPVE EAS detectors.

REFERENCES

1. G. K. Garipov, M. I. Panasyuk, I. A. Rubinshteĭn, *et al.*, Prib. Tekh. Éksp. (in press).
2. A. V. Gurevich and K. P. Zybin, Usp. Fiz. Nauk **171**, 1177 (2001) [Phys. Usp. **44**, 1119 (2001)].
3. M. J. Heavner, PhD Thesis (Univ. of Fairbanks, Alaska, 2000).
4. A. V. Gurevich, K. P. Zybin, and R. A. Roussel-Dupre, Phys. Lett. A **254**, 79 (1999).
5. B. A. Khrenov and M. I. Panasyuk (for the Kosmotepetl Collab.), AIP Conf. Proc. **566**, 57 (2001).
6. B. A. Khrenov (for the Kosmotepetl Collab.), Nucl. Phys. B (Proc. Suppl.) **113**, 115 (2001).

Translated by R. Tyapaev

JETP Letters, Vol. 82, No. 4, 2005, pp. 188–192. From Pis'ma v Zhurnal Éksperimental'noĭ i Teoreticheskoĭ Fiziki, Vol. 82, No. 4, 2005, pp. 207–211.

Nonlinear Dynamics of Surface Dust Vortex and Dust Zonal Flow Systems¶

P. K. Shukla[a] and Dastgeer Shaikh[b]

[a] *Institut für Theoretische Physik IV, Ruhr-Universität Bochum, D-44780 Bochum, Germany*
e-mail: ps@tp4.rub.de

[b] *Institute of Geophysics and Planetary Physics, University of California Riverside, CA 92507, USA*

Received May 27, 2005; in final form, June 22, 2005

We present analytical and simulation studies of highly resolved dust fluid flows involving nonlinearly coupled incompressible surface dust vortex modes (SDVMs) and dust zonal flows (DZFs) in nonuniform unmagnetized dusty plasmas. For this purpose, we use the hydrodynamic equations for the dust fluid and Boltzmann distributed electrons and ions and obtain a set of equations that exhibit nonlinear couplings between the SDVMs and DZFs. The nonlinear equations are then used to investigate the parametric excitation of DZFs by the Reynolds stresses of the SDVMs. Large scale SDVMs emerge through nonlinear interactions with DZFs, and they suppress the dust particle transport across the density gradient. In contrast, DZFs possess short scale vortices with a higher turbulent transport. The relevance of our investigation into the role of coherent structures in a nonuniform dusty plasma is discussed. © *2005 Pleiades Publishing, Inc.*

PACS numbers: 52.27.Lw, 52.35.–q

Dust and dusty plasmas are ubiquitous in space and laboratory discharges [1–3]. In space, dusty plasmas can be found in accretion disks, supernova remnants, interstellar clouds, planetary magnetospheres, cometary tails, and in the Earth's ionosphere/mesosphere. In laboratory discharges, dusty plasmas play a role in plasma processing, edge plasmas in magnetic fusion devices, and in microelectronics fabrication. Dusty plasmas are composed of electrons, ions, and charged micro dust particles. In most space and laboratory dusty plasmas, the dust grains are weakly correlated, since the coupling parameter Γ (the ratio between the average Coulomb interaction energy and the average particle thermal energy) is much smaller than 1. On the other hand, in dusty plasmas with $\Gamma \geq 1$, one encounters dust Coulomb crystals [4], dust microbubbles [5], and dust Coulomb balls [6], which are a manifestation of novel collective processes in dusty plasmas. Dusty plasmas exist in liquid and crystalline phases, as well as in the gaseous state [7]. While enormous work has been carried out to understand the nonlinear dynamics of this complex plasma state, there exist a number of outstanding issues and largely unexplored nonlinear dynamics that need complimentary approaches for a broader universal understanding. With the advent of sophisticated controlled laboratory experiments and computer simulations [2, 8, 9], we have advanced our knowledge of nonlinear effects in complex (dusty) plasmas. For instance, recent experimental investigations [8, 9] of dust nanofluidics show the formation of dust shear flows at kinetic levels and also measure the dust viscosity. Nevertheless, these experiments studying the properties of dust fluid turbulence on a kinetic level require knowledge of energy transfer due to nonlinear mode couplings associated with harmonic generation, which is considered as a generic feature of fully developed plasma and fluid turbulence. Moreover, sheared flows and nonlinear structures are quite common in hydrodynamics [10] and the Martian atmospheres [11], though their self-consistent evolution in a two-dimensional (2D) Yukawa system has not been explored as yet. Our present letter, therefore, investigates, through fully self-consistent nonlinear fluid simulations, the formation of long-scale flows due to surface dust vortex modes (SDVMs) and dust zonal flows (DZFs) in nonuniform unmagnetized, dissipative dusty plasmas. Interestingly, we find that the long-scale flows in our work are excited across a nonuniform dust density gradient; a situation encountered most frequently in numerous laboratory experiments and space plasmas.

Our investigations are based on a model put forward by Hasegawa and Shukla [12], who theoretically pointed out the existence of incompressible SDVMs in a nonuniform, unmagnetized dusty plasma. We first discuss the equilibrium state of our partially ionized laboratory dusty discharges in which collisions between stationary neutrals with electrons and ions are more frequent than those between electrons and ions. In the dust particle loaded discharge, one obtains [13] from the conservation of the electron and ion fluxes the ambipolar electric field $E_{0z} = D_i\chi^{-1}\partial n_{i0}/\partial z - D_e\chi^{-1}\partial n_{e0}/\partial z$, where $D_j = T_j/m_j\nu_{jn}$ and $\mu_{jn} = e/m_j\nu_{jn}$ are

¶ The text was submitted by the authors in English.

the diffusion and mobility of the particle species j (j equals e for electrons, i for ions); e is the magnitude of the electron charge; T_j is the temperature; m_j is the mass; ν_{jn} is the rate of the electron and ion-neutral collisions; $\chi = \mu_i n_{i0} + \mu_e n_{e0}$, $n_{i0} = n_{e0} + Z_d n_{d0}$, n_{i0}, n_{e0}, n_{d0} are the unperturbed number densities of the ions, electrons, and dust grains, respectively; and Z_d is the number of electrons on a dust grain. The vertically upward (along the z axis) ambipolar electric field E_{0z} can levitate a negatively charged dust particle due to a balance between the electric force ($= -Z_d e E_{0z}$) and the vertically downward gravity force $-m_d g$, where m_d is the dust mass, and g is the gravity constant. Nitter [14] has also discussed the levitation of charged dust in the plasma sheath of rf and dc glow discharges where the electric field E_{0z} is obtained by solving Poisson's equation together with a Boltzmann electron density distribution and the ion density distribution deduced from the steady state continuity and momentum equations for collisional ions.

When the equilibrium is perturbed, one has the possibility of nonlinear SDVMs in the form of a dipolar vortex [15] or a chain of vortexes [16], which can be associated with coherent vortical structures in laboratory experiments [17–21]. The concept of drift wave driven zonal flows in a collisional electron–ion plasma (without dust) was introduced by Hasegawa and Wakatani [22]. When the phase speed (wavelength) of the SDVMs and DZFs is much smaller than the electron and ion thermal speeds (the electron and ion collisional mean free paths $V_{\mathrm{Te,\,Ti}}/\nu_{en,\,in}$, where $V_{\mathrm{Te}}(V_{\mathrm{Ti}})$), the electron (ion) thermal speed in dusty plasmas and the perturbed electrostatic forces ($q_j n_{e0,\,i0}\mathbf{E}_1$) acting on electrons and ions balance the corresponding pressure gradient $-\nabla P_{j1}$, where $q_e = -e$, $q_i = e$, and $\mathbf{E}_1$ (P_{j1}) is the perturbed electric field (perturbed pressure). The dynamics of incompressible ($\nabla \cdot \mathbf{v}_d = 0$) SDVMs and DZFs is then governed by the dust continuity and dust momentum equations, namely, [12]

$$\partial \rho_d/\partial t + \nabla \cdot (\rho_d \mathbf{v}_d) = 0, \tag{1}$$

and

$$\rho_d(\partial/\partial t + \nu_d - \eta\nabla^2 + \mathbf{v}_d \cdot \nabla)\mathbf{v}_d = -\nabla P_1 + \rho_d g\hat{\mathbf{z}}, \tag{2}$$

where $\rho_d = m_d(n_{d0} + n_{d1})$, $n_{d1}(\ll n_{d0})$ is a small perturbation in the equilibrium dust number density, $\mathbf{v}_d$ is the perturbed dust fluid velocity, ν_d is the dust-neutral collision frequency, η represents the kinematic dust fluid viscosity (typically $\simeq 10^{-2}$–10^{-1} cm^2/s in the laboratory, similar to that of water $\sim 10^{-2}$ cm^2/s), and $P_1 = P_{e1} + P_{i1} + P_{d1}$ is the perturbation in the equilibrium pressure. We stress that Eq. (2), in which the electric force on charged dust grains is eliminated by using $\mathbf{E}_1 = -(e/Z_d n_d)\nabla(P_{e1} + P_{i1})$, is widely used in the investigation of collective processes in dusty plasmas [15]. Furthermore, the effect of dust charge fluctuations can be neglected [15], since the timescale we are interested in is longer than the dust-charging period (typically microseconds for dusty plasma discharges).

Two-dimensional incompressible SDVMs and DZFs are characterized by the velocity vectors $\mathbf{v}_s = \hat{\mathbf{x}} \times \nabla\psi_s(y, z)$ and $\mathbf{v}_z = \hat{\mathbf{x}} \times \nabla\psi_z(y, z)$, respectively. Here, $\hat{\mathbf{x}}$ is the unit vector along the x axis, which is perpendicular to the z axis, and ψ_s and ψ_z are the stream functions of the SDVMs and DZFs, respectively. Thus, there exist SDVM and DZF vorticities characterized by $\Omega_s = \nabla \times \mathbf{v}_s \equiv \hat{\mathbf{x}}\nabla_\perp^2\psi_s(y, z)$ and $\Omega_z = \nabla \times \mathbf{v}_z \equiv \hat{\mathbf{x}}\nabla_\perp^2\psi_z$. Letting $\rho_d = \rho_{d0} + \rho_{ds}$ and $\mathbf{v}_d = \mathbf{v}_s + \mathbf{v}_z$ in Eqs. (1) and (2), we obtain the governing equations for the SDVMs in the presence of DZFs. We have

$$\left(\frac{\partial}{\partial t} + \hat{\mathbf{x}} \times \nabla\psi_s \cdot \nabla\right)\rho_{ds} + \rho'_{d0}\frac{\partial\psi_s}{\partial y} + (\hat{\mathbf{x}} \times \nabla\psi_z \cdot \nabla)\rho_{ds} = 0, \tag{3}$$

and

$$\left(\frac{\partial}{\partial t} + \nu_d - \eta\nabla^2 + \hat{\mathbf{x}} \times \nabla\psi_s \cdot \nabla\right)\nabla_\perp^2\psi_s + g\frac{\partial\rho_{ds}}{\partial y} + (\hat{\mathbf{x}} \times \nabla\psi_s \cdot \nabla)\nabla_\perp^2\psi_z + (\hat{\mathbf{x}} \times \nabla\psi_z \cdot \nabla)\nabla_\perp^2\psi_s = 0, \tag{4}$$

where $\rho'_{d0} = \partial\rho_{d0}/\partial z$ and $\rho_{d0}(z) \ll \rho_{ds}$. We note that $\rho_{dz} \ll \rho_{ds}$ due to the insignificant variation of the dust zonal flows (ZF) stream function along the y axis.

The dynamics of DZFs in the presence of the SDVMs is governed by

$$\left(\frac{\partial}{\partial t} + \nu_d - \eta\nabla^2 + \hat{\mathbf{x}} \times \nabla\psi_z \cdot \nabla\right)\nabla_\perp^2\psi_z + \Omega_{\mathrm{ave}} = 0, \tag{5}$$

where $\Omega_{\mathrm{ave}} = \langle\hat{\mathbf{x}} \times \nabla\psi_s \cdot \nabla\nabla_\perp^2\psi_s\rangle$ and the angular bracket denotes the averaging over the SDVM period. In the absence of the nonlinear interactions, the SDVMs and DZFs are decoupled. The corresponding dispersion relations obtained from Eqs. (3)–(5) are $\omega^2 + i\omega(\nu_d + \eta k_\perp^2) - \Omega_B^2 k_y^2/(k_y^2 + k_z^2) = 0$ and $\Omega + i(\nu_d + \eta k_\perp^2) = 0$, respectively. Here, $\omega(\Omega)$ is the frequency of the SDVMs (DZFs), and k_y (k_z) is the component of the wavevector along the $y(z)$ axis. The buoyancy frequency squared is denoted by $\Omega_B^2 = g\partial\ln\rho_{d0}/\partial z$. If the equilibrium dust density is proportional to $\exp(-z/L)$, where $L = \rho_{d0}/\rho'_{d0}$ is the dust density gradient scale-size, then $\Omega_B^2 = -g/L$. We note that the latter is positive definite for $L < 0$. In the absence of dissipation, we observe the frequency condensation of SDVMs for $k_z \gg k_y \longrightarrow 0$, indicating the possibility of SDVMs driven by

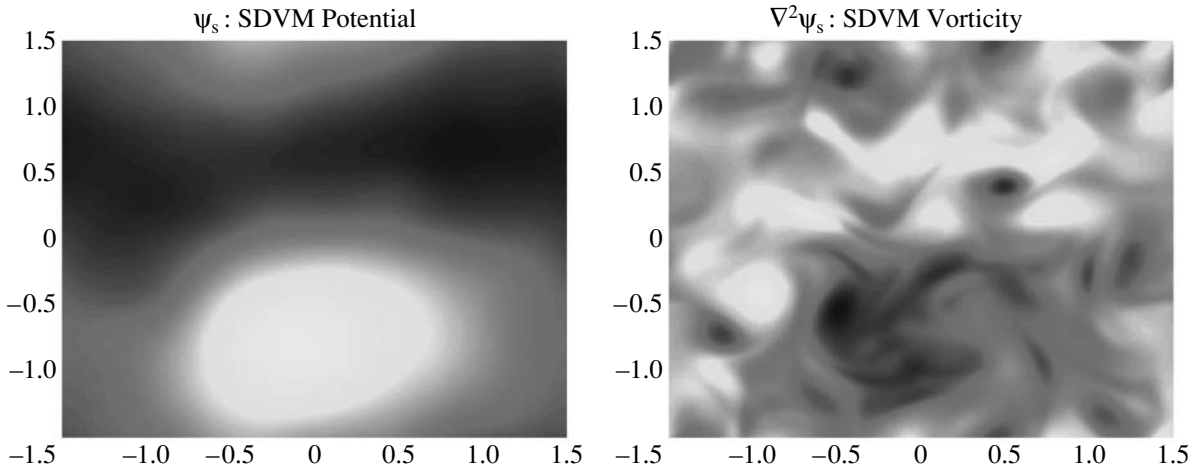

Fig. 1. Time evolution of the SDVMs yields long scale potential flows (left) for which k_z is finite and $k_y \approx 0$. The vorticity component $\nabla^2\psi_s$ consequently possesses elongated small scale structures.

DZFs with short scale structures along the z axis, as discussed below.

We first consider the parametric excitation of DZFs by large amplitude SDVMs. For this purpose, we neglect the self-interaction mode couplings in Eqs. (3)–(5) and let $\rho_{ds} = \rho_{0\pm}\exp(\pm i\mathbf{k}_0 \cdot \mathbf{r} \mp i\omega_0 t) + \sum_{+,-}\rho_\pm \exp(i\mathbf{k}_\pm \cdot \mathbf{r} - i\omega_\pm t)$, $\psi_s = \psi_{0\pm}\exp(\pm i\mathbf{k}_0 \cdot \mathbf{r} \mp i\omega_0 t) + \sum_{+,-}\rho_\pm \exp(i\mathbf{k}_\pm \cdot \mathbf{r} - i\omega_\pm t)$, and $\psi_z = \varphi\exp(i\mathbf{q} \cdot \mathbf{r} - i\Omega t)$, where the subscript $0\pm$ ($\pm$) stands for the SDVM pump (sidebands), $\mathbf{k}_\pm = \mathbf{q} \pm \mathbf{k}_0$, and $\omega_\pm = \Omega \pm \omega_0$. Fourier transforming (3)–(5) and matching the phases, we obtain

$$H_\pm\psi_\pm = \pm i\frac{\omega_0\hat{\mathbf{x}} \times \mathbf{q} \cdot \mathbf{k}_0}{k_\pm^2}(gk_{0y} + 2k_{\perp 0}^2 - q_\perp^2)\psi_{0\pm}\varphi, \quad (6)$$

and

$$(\Omega + i\nu)\varphi = i\frac{\hat{\mathbf{x}} \times \mathbf{k}_0 \cdot \mathbf{q}}{q_\perp^2}(K_-^2\psi_{0+}\psi_- - K_+^2\psi_{0-}\psi_+), \quad (7)$$

where $H_\pm = \omega_\pm^2 + i(\nu_d + \eta k_\pm^2)\omega_\pm - \Omega_B^2 k_{0y}^2/k_\pm^2$, $k_\pm^2 = k_{0y}^2 + k_{z\pm}^2$, $K_\pm^2 = k_{\perp\pm}^2 - k_{0\perp}^2$, and $\nu = \nu_d + \eta q_\perp^2$. Eliminating $\psi_\pm$ from Eq. (7) by using Eq. (6), we have the nonlinear dispersion relation

$$\Omega + i\nu = \omega_0\frac{|\hat{\mathbf{x}} \times \mathbf{k}_0 \cdot \mathbf{q}|^2}{q_\perp^2} \times (gk_{0y} + 2k_{\perp 0}^2 - q_\perp^2)\sum_{+,-}\frac{K_\pm^2|\psi_0|^2}{H_\pm}, \quad (8)$$

where $|\psi_0|^2 = \psi_{0+}\psi_{0-}$. For $q_\perp \ll |\mathbf{k}_0|$, we obtain from Eq. (8) $\Omega(\Omega + i\nu) = (|\hat{\mathbf{x}} \times \mathbf{k}_0 \cdot \mathbf{q}|/q_\perp^2)(gk_{0y} + 2k_{\perp 0}^2)\mathbf{q} \cdot \mathbf{k}_{0\perp}|\psi_0|^2$, which predicts a purely growing instability ($\Omega = i\gamma$) if the growth rate $\gamma > \nu$ and $(gk_{0y} + 2k_{\perp 0}^2)\mathbf{q} \cdot \mathbf{k}_{0\perp} < 0$. For some typical values, viz., $|\mathbf{v}_s| \sim C_D$, $|\mathbf{k}/\mathbf{k}_0| \sim 0.1$, we have $\gamma \sim$ one tenth of the dust acoustic wave frequency $k_0 C_D$, where C_D is the dust acoustic speed [15].

Next, in order to study the dynamics of nonlinearly coupled SDVMs and DZFs, we develop a nonlinear code to carry out high resolution computer simulations of (3)–(5) in a periodic box of length π in each direction. The time integration uses a second order predictor–corrector method. The spatial resolution is 1024×1024 Fourier modes. All the fluctuations in the simulations are initialized with a Gaussian random number generator to ensure that the Fourier modes are all spatially uncorrelated and randomly phased. This ensures a nearly isotropic initial condition in the real space. We further make sure that no asymmetry is introduced in the dynamical evolution by the initial spectra and the boundary conditions. The normalization is as follows: ρ_{ds} by ρ_{d0}; $\psi_{s,z}$ by $C_D\lambda_D$; t by ω_{pd}^{-1}; and the space variable by $\lambda_D = C_D/\omega_{pd}$, where $\lambda_D = C_D/\omega_{pd}$ is the dusty plasma Debye radius [15]. Thus, the free parameters in our simulations are $\nu_d/\omega_{pd} \sim 10^{-2}$–$10^{-3}$, $\eta/C_D\lambda_D \sim 10^{-2}$, $\lambda/L \sim 0.01$, and $g\lambda/C_D^2 \sim \lambda_D/L_p \sim 0.01$, where $L_p^{-1} = -P_0^{-1}\partial P_0/\partial z$. In Figs. 1 and 2, we show the evolutions of the stream functions and vorticities of the SDVMs and DZFs, respectively. We see that the stream functions are coherent, contrary to the irregular vorticities. This is an indication of the dual cascade, in which energy from short scale SDVMs is transferred to large scale DZFs. It is pertinent to note from Eqs. (3)–(5) that the mode $k_y \approx 0$ cannot be excited in a linear regime in which this mode is entirely absent from the dynamics.

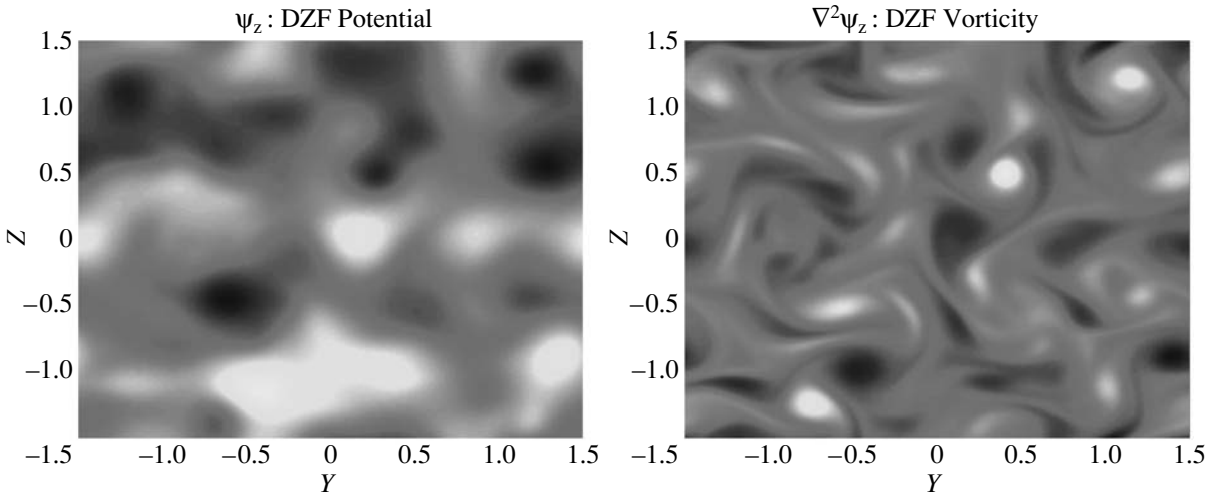

Fig. 2. Dust zonal flows (DZF) tend to cascade towards shorter length scales that eventually align along the flow direction.

Nevertheless, the $k_y \approx 0$ mode, essentially leading to an asymmetric large scale flows in a real space, is generated purely as a result of nonlinear interactions among SDVMs and DZFs in an inertial range spectral space across a large equilibrium dust density gradient. More precisely, in the SDVMs, the energy flows towards smaller k's, so that we expect large-scale structures similar to the modified Navier–Stokes (NS) turbulence. On the other hand, DZFs are the zero-frequency limit of the SDVM mode; they have very small k_y and very large k_z, so that the frequency condensation occurs for short wavelength (viz., $k_z \gg k_y$) structures. DZFs are excited due to the Reynolds stresses of the SDVMs. While the Reynolds stresses possess a tendency of typically generating large-scale flows, their time average appearing in Eq. (5) causes a net nonlinear dissipation of zonal flows. This appears to be the primary reason why DZFs form short scales (see Fig. 2). The vorticity field of DZFs in Fig. 2 appears to be stretched across the equilibrium density gradient wrapping the small-scale dust vortex structures around in the nonlinear saturated state. The vortices are trapped in the horizontal sheared flow and propagate along the self-consistent flow across the equilibrium gradient. The energy spectrum decays due to dust-neutral collisions and dust kinematic viscosity at smaller scales. Figure 3 exhibits a high-resolution Kolomogrov-like spectrum of a fully developed coupled SDVM–ZF turbulent system. The spectrum of SDVMs is evidently steeper than that of DZFs in the inertial regime, thereby indicating the presence of large-scale structures in its spectrum. This is further consistent with Fig. 1, which demonstrates $k_y \approx 0$ flows in the saturated SDVM–ZF turbulent state. It is to be noted that both the spectra in Fig. 3 are steeper compared to the fully developed 2D turbulent spectra for enstrophy or energy due to large-scale structures that condensate the lower Fourier modes because of inverse cascade processes. The dust density fluctuations also cascade towards long-scale structures due to short scale vortex merging. There also exist nonthermal transport associated with the effective turbulent diffusion ($D_{\text{eff}} = \int_0^\tau d\tau \langle v(y, t=0) v(y, t+\tau) \rangle$) of a dust particle in large scale ZF structures due to a random walk of the macroparticles in enhanced zonal flow fluctuations. As expected, emergence of large-scale coherent flows in SDVMs quench turbulent transport, in contrast to that involving random short scale DZFs, as shown in Fig. 4. In nonuniform, nonlinear media without dust, 2D flows have been explained on the basis of the NS and the

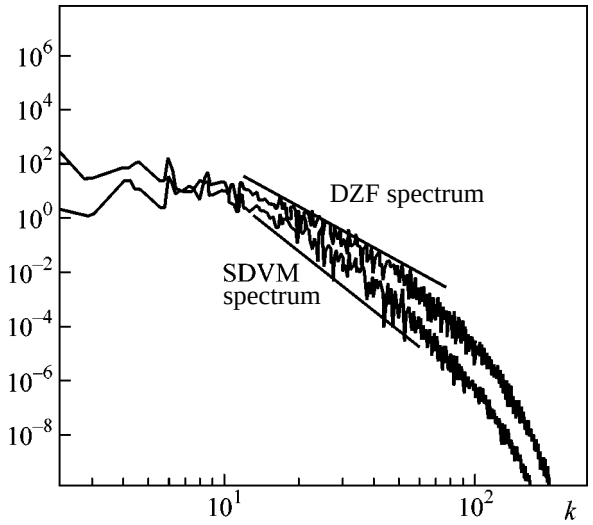

Fig. 3. Kolmogorov-like turbulent spectra of a coupled DZF and SDVMs system. The spectrum of SDVMs in inertial range turbulence is more steep than that of DZF due to the presence of large scale flows that have $k_y \approx 0$. The numerical resolution is 1024×1024 Fourier modes in a two-dimensional box.

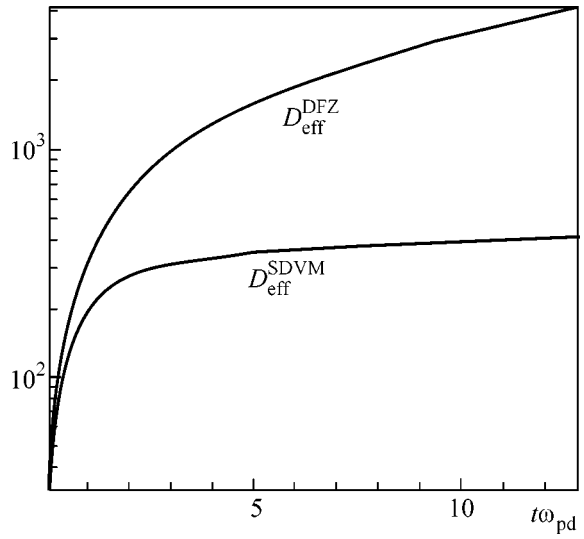

Fig. 4. Effective diffusion coefficient associated with nonlinear turbulent transport in a coupled SDVM–DZF system. In agreement with Fig. 3, transport is suppressed due to the presence of large-scale flows in SDVM, while it is enhanced in short scales DZFs.

Charney–Hasegawa–Mima (CHM) equations [23, 24], which have two constants of motion, namely, the energy and enstrophy (squared vorticity). The energy decays from a source to a long wavelength, while enstrophy flows to shorter scales. Such a dual cascading, in agreement with the statistical quasi-equilibrium theory, ensures the formation of coherent vortical structures (eddies) [25], which are responsible for producing enhanced transport of fluids and plasma particles. For unbounded 2D NS turbulence, the conserved quantities are the kinetic energy $E = \int_0^\infty E(k)dk$ and fluid enstrophy $Z = \int_0^\infty k^2 E(k)dk$, where E_k is the kinetic energy spectrum. For CHM turbulence, the conserved quantities are the total energy $E + \lambda^2 I$ and total enstrophy $Z + \lambda^2 E$, where $I = \int_0^\infty k^{-2} E(k)dk$ and λ is a positive constant.

To summarize, we have presented a nonlinear mechanism by which DZFs can be generated on account of the energy of incompressible SDVMs in a nonuniform unmagnetized dusty plasma. Specifically, we have presented a system of equations that shows that nonlinear couplings between the SDVMs and DZFs occur due to interactions between the SDVM density fluctuation and the velocity fluctuation of DZFs, as well as due to the dust fluid advection in the coupled SDVM–DZF system. The coupled mode equations are analyzed to show the existence of the modulational instability, which drives DZFs at nonthermal levels. The dynamics of nonlinearly interacting SDVMs and DZFs reveals interesting features of dual cascading leading to the formation of large scale dust vortices. The latter can produce dust particle transport across the density gradient. In fact, localized dust grain structures in association with dust grain transport have been observed in nonuniform laboratory dusty plasma discharges [17–21].

This work was partially supported by the Deutsche Forschungsgemeinschaft through the Sonderforschungsbereich 591. The work of D.S. was supported in part by NASA (grant nos. NAG5-1162 and NAG5-10932) and by the US National Science Foundation (grant no. ATM0296113).

REFERENCES

1. R. Merlino and J. Goree, Phys. Today **57**, 32 (2004).
2. V. E. Fortov *et al.*, Phys. Usp. **47**, 447 (2004).
3. M. Horányi *et al.*, Rev. Geophys. **42**, RG4002 (2004).
4. J. H. Chu and Lin I, Phys. Rev. Lett. **72**, 4009 (1994); H. Thomas *et al.*, Phys. Rev. Lett. **73**, 652 (1994).
5. H. Y. Chu *et al.*, Phys. Rev. Lett. **90**, 075004 (2003).
6. O. Arp *et al.*, Phys. Rev. Lett. **93**, 165004 (2004).
7. H. M. Thomas and G. Morfill, Nature **379**, 806 (1996); Lin I *et al.*, Science **272**, 1626 (1996).
8. G. E. Morfill *et al.*, Phys. Rev. Lett. **92**, 175 004 (2004).
9. V. Nosenko and J. Goree, Phys. Rev. Lett. **93**, 155004 (2004).
10. M. Lesieur, *Turbulence in Fluids* (Kluwer Academic, Dordrecht, 1991).
11. R. Greely *et al.*, Geophys. Res. Lett. **31**, L24702 (2004).
12. A. Hasegawa and P. K. Shukla, Phys. Lett. A **332**, 82 (2004).
13. K. Ostrikov, Phys. Rev. E **71**, 026405 (2005).
14. T. Nitter, Plasma Sources Sci. Technol. **5**, 93 (1996).
15. P. K. Shukla and A. A. Mamun, *Introduction to Dusty Plasma Physics* (Inst. of Physics, Bristol, 2002).
16. V. I. Petviashvilli and O. A. Pokhotelov, *Solitary Waves in Plasmas and in the Atmosphere* (Gordon and Breach, Philadelphia, 1993).
17. D. A. Law *et al.*, Phys. Rev. Lett. **80**, 4189 (1998); G. E. Morfill *et al.*, Phys. Rev. Lett. **83**, 1598 (1999).
18. O. S. Vaulina *et al.*, JETP **91**, 1147 (2000); New J. Phys. **6**, 82 (2003).
19. V. A. Rykov *et al.*, New J. Phys. **5**, 129 (2003).
20. V. E. Fortov *et al.*, JETP **96**, 704 (2003).
21. O. S. Vaulina *et al.*, Plasma Phys. Rep. **30**, 918 (2004).
22. A. Hasegawa and M. Wakatani, Phys. Rev. Lett. **50**, 682 (1983).
23. J. G. Charney, Publ. Kosjones. Nors. Videnshap. Akad. Oslo **17**, 3 (1948); A. Hasegawa and K. Mima, Phys. Rev. Lett. **39**, 205 (1977); Phys. Fluids **21**, 87 (1978); A. Hasegawa, Adv. Phys. **34**, 1 (1985).
24. A. Hasegawa *et al.*, Phys. Fluids **22**, 2122 (1979); W. Horton and A. Hasegawa, Chaos **4**, 227 (1994); M. V. Nezlin *et al.*, Chaos **6**, 309 (1996); W. Horton, Rev. Mod. Phys. **71**, 735 (1999).
25. W. Horton and Y. H. Ichikawa, *Chaos and Structures in Nonlinear Plasmas* (World Sci., Singapore, 1996).

JETP Letters, Vol. 82, No. 4, 2005, pp. 193–197. Translated from Pis'ma v Zhurnal Éksperimental'noĭ i Teoreticheskoĭ Fiziki, Vol. 82, No. 4, 2005, pp. 212–216.

High-Pressure Effect on the Crystal and Magnetic Structures of the Frustrated Antiferromagnet $YMnO_3$

D. P. Kozlenko[a], S. E. Kichanov[a, *], S. Lee[b], J.-G. Park[b, c], V. P. Glazkov[d], and B. N. Savenko[a]

[a] *Joint Institute for Nuclear Research, Dubna, Moscow region, 141980 Russia*

** e-mail: ekich@nf.jinr.ru*

[b] *Department of Physics and Institute of Basic Science, SungKyunKwan University, Suwon 440-746, Republic of Korea*

[c] *Center for Strongly Correlated Materials Research, Seoul National University, Seoul 151-742, Republic of Korea*

[d] *Russian Research Centre, Kurchatov Institute, Moscow, 123182 Russia*

Received June 6, 2005

The high-pressure (to 5 GPa) effect on the crystal and magnetic structures of the hexagonal manganite $YMnO_3$ is studied by neutron diffraction in the temperature range 10–295 K. A spin-liquid state due to magnetic frustration on the triangular lattice formed by Mn ions is observed in this compound at normal pressure and $T > T_N = 70$ K, and an ordered triangular antiferromagnetic state with the symmetry of the irreducible representation Γ_1 arises at $T < T_N$. The high-pressure effect leads to a spin reorientation of Mn magnetic moments and a change in the symmetry of the antiferromagnetic structure, which can be described by a combination of the irreducible representations Γ_1 and Γ_2. In addition, it is observed that the ordered magnetic moment of Mn ions decreases from 3.27 μ_B (0 GPa) to 1.52 μ_B (5 GPa) at $T = 10$ K and diffuse scattering is enhanced at temperatures close to T_N. These effects can be explained within the model of the coexistence of the ordered antiferromagnetic phase and the spin-liquid state, whose volume fraction increases with pressure due to the enhancement of frustration effects. © *2005 Pleiades Publishing, Inc.*

PACS numbers: 62.50.+p, 75.25.+z, 75.47.Lx

Manganites $RMnO_3$ exhibit a wide variety of physical properties depending on the rare-earth element R. Compounds with a large ionic radius of the element R (La, Pr, Nd, Sm, Eu, Gd, and Tb) are crystallized in an orthorhombic structure with the *Pnma* space group [1]. In compounds with a smaller ionic radius of the element R (Ho, Er, Tm, Yb, Lu, Y, Sc, and In), a hexagonal crystal structure with the $P6_3cm$ space group is observed [2]. Hexagonal manganites belong to a class of ferroelectromagnets in which the transition temperature to the ferroelectric state $T_C \sim 600$–900 K is much higher than the antiferromagnetic (AFM) ordering temperature $T_N \sim 70$–130 K [3]. A characteristic feature of the hexagonal structure of $RMnO_3$ manganites is the occurrence of two-dimensional triangular lattices formed by Mn ions in the (*ab*) planes, which leads to geometrically frustrated magnetism. The planar triangular Mn lattices are separated from each other by noncoplanar layers of rare-earth ions so that the distances between the nearest neighboring Mn atoms in the lattice plane (*ab*) are about 3.5 Å, which is appreciably smaller than the distance between the neighboring Mn planes along axis *c* (about 6 Å). As a result, the AFM Mn–O–Mn superexchange inside the planes is dominant, while the Mn–O–O–Mn superexchange between neighboring planes is approximately two orders of magnitude weaker [4]. The magnetic properties of hexagonal $RMnO_3$ manganites essentially depend on the ionic radius *r* of the element R. In the $InMnO_3$ compound with the largest *r*, magnetic ordering is not observed down to 5 K [5]. In $YMnO_3$ at $T < T_N = 70$ K, the magnetic moments of Mn ions are ordered into a trigonal AFM structure whose symmetry can be described within the models of the Γ_1 or Γ_3 irreducible representation [4, 6–8]. The AFM ordering in compounds with a smaller value of *r* ($HoMnO_3$, $ErMnO_3$, $TmMnO_3$, $YbMnO_3$, $LuMnO_3$, and $ScMnO_3$) has a different symmetry type and can be described within the models of the Γ_2 or Γ_4 irreducible representation [6, 9–14]. In addition, spin-reorientation phase transitions were detected in $ScMnO_3$ and $HoMnO_3$ at temperatures $T_R < T_N$ [6, 9–13]. The change in the character of the magnetic ordering in hexagonal manganites with changing *r* indicates that the competing exchange interactions strongly depend on structural parameters. Besides chemical substitution, the balance of these interactions can be substantially changed by applying an external high pressure, which also leads to a change in the structural parameters. However, the high-pressure effect on the structure and properties of hexagonal manganites is poorly understood.

This work is devoted to studying the interplay between changes in the crystal and magnetic structure of the hexagonal manganite $YMnO_3$ at high pressures by neutron diffraction.

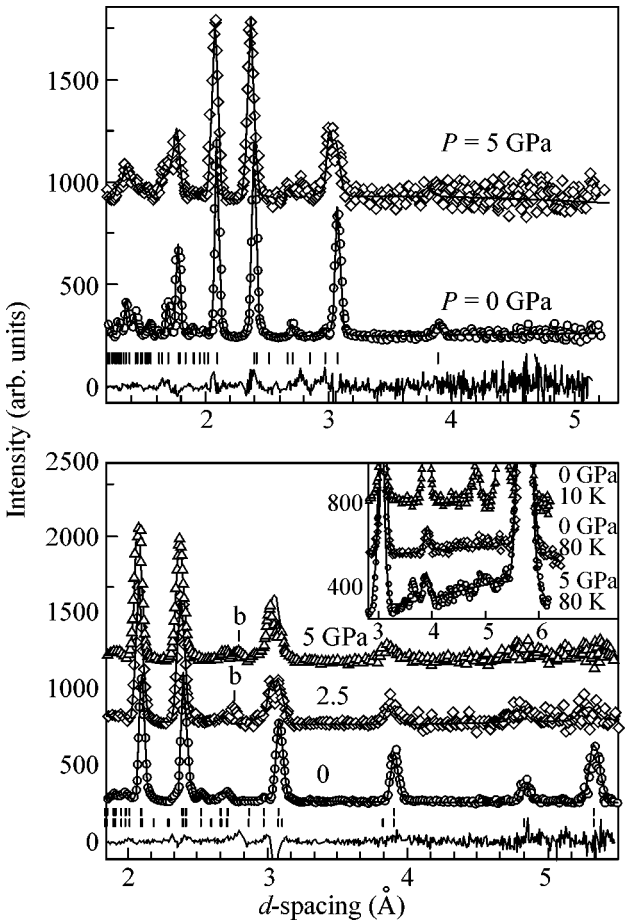

Fig. 1. Diffraction spectra of $YMnO_3$ measured at pressures P = 0, 2.5, and 5 GPa; temperatures T = 295, 10, and 80 K; and scattering angles 2θ = 90° and (the inset) 45.5° and treated by the Rietveld method. The experimental points, calculated profile, and difference curve are presented for P = 5 GPa and T = (upper panel) 290 and (lower panel) 10 K. Dashes indicate the calculated positions of (the upper row) structural and (the lower row) magnetic diffraction peaks. The diffraction peak from the high-pressure cell is marked with the letter b.

1. EXPERIMENTAL PROCEDURE

Polycrystalline $YMnO_3$ samples were prepared by a conventional solid-phase reaction method. The Y_2O_3 (99.999%) and Mn_2O_3 (99.999%) oxides were mixed thoroughly; the obtained uniform mixture was heated to 900°C for 12 h and then was successively annealed for 24 h at temperatures of 1100 and 1200°C, after which final sintering was performed at a temperature of 1350°C for 24 h with intermediate grindings to prevent the formation of stable phases of minor impurities. An x-ray diffraction analysis showed that the obtained samples contain a pure hexagonal $YMnO_3$ phase.

Experiments on neutron diffraction were performed on the DN-12 spectrometer [15] of the IBR-2 pulsed high-flux reactor (Frank Laboratory of Neutron Physics, Joint Institute for Nuclear Research, Dubna) with the use of high-pressure sapphire anvil cells [16] in the range of high external pressures up to 5 GPa and temperatures of 10–300 K. The diffraction spectra were measured at scattering angles of $2\theta = 90°$ and 45.5°. For these scattering angles, the diffractometer resolution at the wavelength λ = 2 Å was $\Delta d/d$ = 0.02 and 0.025, respectively. The characteristic measurement time of one spectrum was 20 h. The volume of the samples under study was $V \sim 2.5$ mm^3. The pressure in the cell was measured by the ruby luminescence line shift with an accuracy of 0.05 GPa. The value averaged over the pressures determined for several small ruby crystals (50–100 μm) located at various points on the sample surface was used as the pressure on the sample. The gradient of the pressure distribution over the sample surface did not exceed 20%. The measurements with the high-pressure cell at low temperatures were performed with the use of a specialized cryostat based on a closed-cycle helium refrigerator. The diffraction data were analyzed by the Rietveld method using the MRIA [17] and FullProf [18] programs for the crystal and magnetic structures, respectively.

2. RESULTS AND DISCUSSION

Parts of the diffraction spectra of $YMnO_3$ obtained at various pressures and temperatures are shown in Fig. 1. In the entire range of pressures up to 5 GPa and temperatures (10–295 K), the crystal structure of this compound retains its initial hexagonal symmetry. The structural parameters of $YMnO_3$ calculated based on the diffraction data for some temperatures and pressures are given in the table. The values of the parameters obtained at normal conditions are in good agreement with the values obtained in the previous investigations [6, 7]. At normal pressure and temperatures below T_N = 70 K, the occurrence of (100) and (101) magnetic reflections was observed at d_{hkl} = 5.31 and 4.82 Å, respectively, and the occurrence of a magnetic contribution to the (102) nuclear reflection was observed at d_{hkl} = 3.88 Å, which pointed to the occurrence of a triangular AFM state in which the magnetic moments of Mn are located in the (*ab*) plane and oriented at angles of 120° with respect to each other. The initial analysis of the magnetic structure was carried out using the models of the Γ_1 and Γ_3 irreducible representations. A better agreement with the experimental data was obtained for the Γ_1 model (Fig. 2) as well as in earlier work [6]. The value of the magnetic moment of manganese 3.27(5) μ_B obtained at T = 10 K is in good agreement with the previous studies of $YMnO_3$ at normal pressure [6–8] and is significantly lower than the expected value of 4.0 μ_B for the Mn^{3+} ion. At temperatures somewhat higher than T_N, appreciable diffuse scattering was observed in the range of interplanar distances $4 < d_{hkl} < 6$ Å (Fig. 1). Its occurrence in the vicin-

ity of T_N as well as the small value of the ordered magnetic moment of Mn is the consequence of the geometrical magnetic frustration characteristic of the triangular AFM configurations. According to [8], the magnetic state of $YMnO_3$ in the vicinity of T_N can be considered as a spin liquid with strong magnetic frustrations and the residual regions of the spin-liquid state at temperatures below T_N coexist with the ordered AFM state. At the pressure $P = 2.5$ GPa and temperatures $T < T_N$, a decrease and a relative change are observed in the intensities of the magnetic peaks (Fig. 1). The ratio of the peak intensities $I_{(100)}/I_{(101)}$ at $T = 10$ K decreases substantially from 3.4 at $P = 0$ to 1.5 at $P = 2.5$ GPa. An analysis of the diffraction data showed that this effect is due to the spin reorientation of the magnetic moments of Mn in the (*ab*) plane. The angle φ between the direction of the magnetic moment of Mn and the crystallographic axis *a* changes from 90° (at $P = 0$) to 60° ($P = 2.5$ GPa), while the AFM symmetry changes and can be described by a combination of the irreducible representations $\Gamma_1 + \Gamma_2$ (Fig. 2). The latter allows arbitrary values of the angle φ between 90° (corresponding to the Γ_1 representation) and 0° (corresponding to the Γ_2 representation). As the pressure increases further to 5 GPa, the angle φ decreases from 60° to 41°. In the pressure range 0–5 GPa, the ordered magnetic moment of Mn decreases from 3.27(3) to 1.52(9) μ_B. Simultaneously with this, an increase in diffuse scattering is observed in the range of interplanar distances $4 < d_{hkl} < 6$ Å (Fig. 1). Both effects can point to an increase in the volume fraction of the spin-liquid state under high pressure and to the suppression of the ordered AFM phase. In the hexagonal $YMnO_3$ structure, the Mn and O ions form MnO_5 bipyramids containing four nonequivalent Mn–O bonds: Mn–O1 and Mn–O2 are oriented along the crystallographic axis *c*, and Mn–O3 and two Mn–O4 bonds are arranged in the (*ab*) plane [19]. With increasing pressure, the lengths of various Mn–O bonds (Fig. 3), as well as the unit cell parameters (table) and volume, decrease almost linearly. The obtained linear compressibilities of the Mn–O bond lengths $k_i = -(1/l_{\mathrm{Mn-O}_{i0}})(dl_{\mathrm{Mn-O}_i}/dP)_T$ ($i = 1, 2, 3, 4$) at $T = 295$ K are $k_1 = 0.0097$, $k_2 = 0.0055$, $k_3 = 0.0011$, and $k_4 = 0.0055$ GPa^{-1}. In the treatment of the high-pressure data by the Rietveld method, it was difficult to determine the coordinates of the O1 atom to a sufficient accuracy because of the restricted range of d_{hkl} and the comparatively large number of independent parameters. Therefore, the baric dependence of the Mn–O1 bond length and the value of k_1 were calculated with the fixed O1 coordinates obtained at $P = 0$ (table), and these data should be considered estimated. The calculated values of the linear compressibility of the unit cell parameters $k_i = -(1/a_{i0})(da_i/dP)_T$ ($a_i = a, c$) at $T = 295$ K are $k_a = 0.0027$ and $k_c = 0.0019$ GPa^{-1}. These values are close to the analogous values for manganites of the orthorhombic ($La_{1-x}Ca_xMnO_3$ and $Pr_{1-x}Na_xMnO_3$ [20]), tetragonal ($Pr_{1-x}Sr_xMnO_3$ [21]), and rhombohedral ($La_{1-x}Sr_xMnO_3$ [22]) symmetry. As the pressure increases to 2.5 GPa, the Mn–O3–Mn bond angle increases slightly and the Mn–O4–Mn bond angle remains virtually unchanged. As the pressure increases further, the tendency for a decrease in these angles is observed (Fig. 4). In the hexagonal $YMnO_3$ structure, the O3 and O4 oxygen atoms are arranged near the centers of the triangles formed by Mn ions in the (*ab*) planes [19] and the intraplane 120° superexchange Mn–O3–Mn and Mn–O4–Mn interactions are dominant. Because of the difference in the Mn–O3 and Mn–

Structural parameters of $YMnO_3$ at various pressures and $T = 295$ K. The Y1 and O3 atoms are located in positions 2(a) (0, 0, *z*); Mn, O1, and O2 atoms are in positions 6(c) (*x*, 0, *z*); and Y2 and O4 atoms are in positions 4(b) (1/3, 2/3, *z*) of the space group $P6_3$ cm; for Mn atoms, coordinate $z = 0$. The magnetic moment M of Mn ions and the angle φ characterizing it orientation with respect to the a axis at $T = 10$ K are also presented

P (GPa)	0	2.5	5.0
a (Å)	6.151(3)	6.102(5)	6.067(5)
c (Å)	11.410(5)	11.358(8)	11.305(8)
Y1: z	0.270(2)	0.266(4)	0.269(4)
Y2: z	0.228(2)	0.225(4)	0.223(4)
Mn: x	0.326(5)	0.322(6)	0.325(7)
O1: x	0.308(3)	0.308	0.308
z	0.161(4)	0.157(5)	0.164(6)
O2: x	0.642(3)	0.639(5)	0.630(6)
z	0.336(2)	0.335(4)	0.349(7)
O3: z	0.473(5)	0.506(8)	0.474(8)
O4: z	0.012(3)	0.011(5)	0.014(5)
M (μ_B)	3.27(2)	1.93(7)	1.52(9)
φ	$90.0(5)^0$	$60(3)^0$	$41(2)^0$

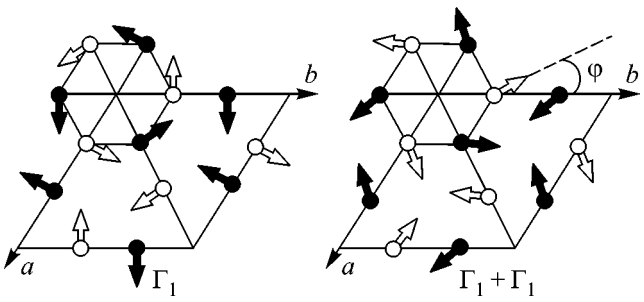

Fig. 2. Triangular antiferromagnetic structures corresponding to the symmetry of (left) the irreducible representation Γ_1 and (right) the combination of the irreducible representations Γ_1 and Γ_2. The orientations of the magnetic moments of Mn in the planes $z = 0$ and $z = 1/2$ are shown in white and black colors, respectively.

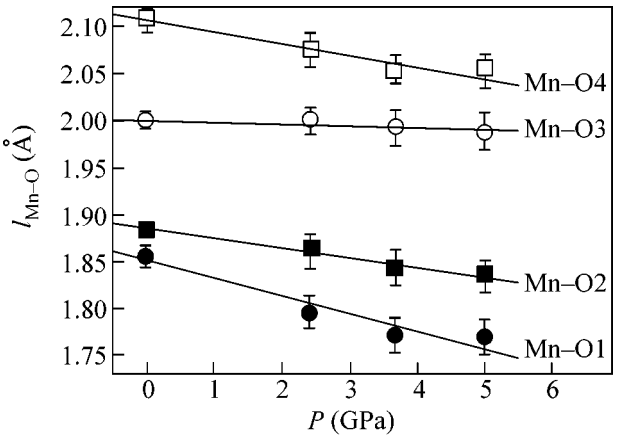

Fig. 3. Baric dependences of Mn–O bond lengths in the hexagonal structure of $YMnO_3$ and their linear interpolation.

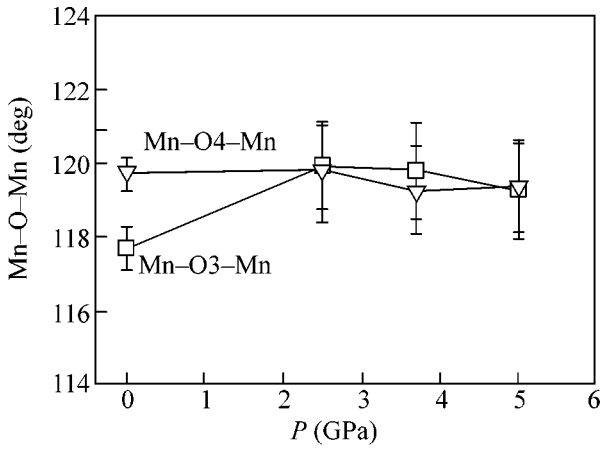

Fig. 4. Baric dependences of Mn–O3–Mn and Mn–O4–Mn bond angles.

O4 bond lengths and Mn–O3–Mn and Mn–O4–Mn bond angles, the strength of these interactions is different, which leads to a partial suppression of the effects of geometrical magnetic frustration. Under high pressure, the degree of nonequivalence of these interactions decreases. The relative difference between the Mn–O3 and Mn–O4 bond lengths decreases from 5% at $P = 0$ to 3% at $P = 5$ GPa, and the Mn–O3–Mn and Mn–O4–Mn bond angles at the pressure $P = 5$ GPa have almost equal values of 119.3°, while these angles at $P = 0$ equal 117.7° and 119.7°, respectively. Symmetrization of the triangular lattice of Mn ions at high pressures enhances the effects of geometrical magnetic frustration, as a result of which the ordered magnetic moment of manganese decreases and the diffuse scattering is enhanced in the vicinity of T_N. The spin reorientation observed in the AFM phase of $YMnO_3$ under high pressure can be induced by the change in the magnetocrystalline energy due to the change in the structural parameters

$$E_a = K_1\sin^2\theta + K_2\sin^4\theta + K_3\sin^6\theta + K_4\cos\theta\sin^3\theta\sin 3\varphi + K_5\sin^6\theta\cos 6\varphi, \quad (1)$$

where φ and θ are spherical coordinates that describe the orientation of the magnetic moments of manganese, and K_1–K_5 are the anisotropy constants [23, 24]. The minimization of Eq. (1) for θ = 90° with respect to φ [24] yields the following possible easy magnetization directions in the (*ab*) plane:

$$\varphi = \begin{cases} 30°, 90°, 150°, \ldots \text{ for } K_5 > 0 \\ 0°, 60°, 120°, \ldots \text{ for } K_5 < 0. \end{cases} \quad (2)$$

The case of $K_5 > 0$ corresponds to the orientation of the magnetic moments in $YMnO_3$ at $P = 0$, while the case of $K_5 < 0$ describes the orientation of the magnetic moments at high pressure. A similar spin-reorientation transition leading to a change in the symmetry of the magnetic structure from the irreducible representation Γ_2 to the combination $\Gamma_1 + \Gamma_2$ was observed in $ScMnO_3$ at normal pressure and low temperatures [6]. The Mn–O3 and Mn–O4 bond lengths in this compound are almost equal, and the triangular configuration of the Mn ions is more symmetric, as in $YMnO_3$ at high pressures.

The results of this work demonstrate that spin reorientation of the magnetic moments of Mn and a change in the symmetry of the ordered antiferromagnetic state occur in $YMnO_3$ at high pressure. The possible reason for this effect is a change in the sign of the anisotropy constant K_5 and the magnetocrystalline energy due to the modification of structural parameters. The decrease in the distortions of the triangular lattice of Mn ions under high pressure leads to a decrease in the difference in the strength of the competing magnetic intraplane interactions, which leads to enhancement of the effects of geometrical magnetic frustration and is manifested in a decrease in the ordered magnetic moment of manganese and in enhancement of the diffuse scattering in the vicinity of T_N. These effects point to the suppression of the ordered antiferromagnetic state and to an increase in the volume fraction of the spin-liquid phase under high pressure.

This work was supported by the Russian Foundation for Basic Research, project no. 03-02-16879. J.G. Park is also grateful to the Center for Strongly Correlated Materials Research and the Ministry of Science and Technology of the Republic of Korea (the CNRF project) for support.

REFERENCES

1. M. A. Gilleo, Acta Crystallogr. **10**, 161 (1957).
2. H. L. Yakel, W. C. Koehler, E. F. Bertaut, *et al.*, Acta Crystallogr. **16**, 957 (1963).

3. T. Katsufuji, M. Masaki, A. Machida, *et al.*, Phys. Rev. B **66**, 134434 (2002).
4. E. F. Bertaut, M. Mercier, and R. Pauthenet, Phys. Lett. **5**, 27 (1963).
5. J. E. Greedan, M. Bieringer, J. F. Britten, *et al.*, J. Solid State Chem. **116**, 118 (1995).
6. A. Munoz, J. A. Alonso, M. J. Martinez-Lope, *et al.*, Phys. Rev. B **62**, 9498 (2000).
7. J. Park, U. Kong, A. Pirogov, *et al.*, Appl. Phys. A **74** (Suppl.), S796 (2002).
8. J. Park, J.-G. Park, G. S. Jeon, *et al.*, Phys. Rev. B **68**, 104426 (2003).
9. W. C. Koehler, H. L. Yakel, E. O. Wollan, *et al.*, Phys. Lett. **9**, 93 (1964).
10. M. Fiebig, D. Fröhlich, K. Kohn, *et al.*, Phys. Rev. Lett. **84**, 5620 (2000).
11. A. Munoz, J. A. Alonso, M. J. Martinez-Lope, *et al.*, Chem. Mater. **13**, 1497 (2001).
12. Th. Lonkai, D. Hohlwein, J. Ihringer, *et al.*, Appl. Phys. A **74** (Suppl.), S843 (2002).
13. O. P. Vajk, M. Kenzelmann, J. W. Lynn, *et al.*, Phys. Rev. Lett. **94**, 087601 (2005).
14. J. Park, U. Kong, S. I. Choi, *et al.*, Appl. Phys. A **74** (Suppl.), S802 (2002).
15. V. L. Aksenov, A. M. Balagurov, V. P. Glazkov, *et al.*, Physica B (Amsterdam) **265**, 258 (1999).
16. V. P. Glazkov and I. N. Goncharenko, Fiz. Tekh. Vys. Davleniĭ **1**, 56 (1991).
17. V. B. Zlokazov and V. V. Chernyshev, J. Appl. Cryst. **25**, 447 (1992).
18. J. Rodriguez-Carvajal, Physica B (Amsterdam) **192**, 55 (1993).
19. B. B. Van Aken and T. T. M. Palstra, Phys. Rev. B **69**, 134113 (2004).
20. D. P. Kozlenko, Z. Jirák, I. N. Goncharenko, *et al.*, J. Phys.: Condens. Matter **16**, 5883 (2004).
21. D. P. Kozlenko, V. P. Glazkov, Z. Jirák, *et al.*, J. Phys.: Condens. Matter **16**, 2381 (2004).
22. D. P. Kozlenko, I. N. Goncharenko, B. N. Savenko, *et al.*, J. Phys.: Condens. Matter **16**, 6755 (2004).
23. R. Fieschi and F. G. Fumi, Nuovo Cimento **10**, 865 (1953).
24. W. Nitsche and W. Kleemann, Phys. Rev. B **36**, 8587 (1987).

Translated by A. Bagatur'yants

JETP Letters, Vol. 82, No. 4, 2005, pp. 198–203. From Pis'ma v Zhurnal Éksperimental'noĭ i Teoreticheskoĭ Fiziki, Vol. 82, No. 4, 2005, pp. 217–222.

Destruction of the Fermi Surface Due to Pseudogap Fluctuations in Strongly Correlated Systems¶

E. Z. Kuchinskii, I. A. Nekrasov, and M. V. Sadovskii*

Institute of Electrophysics, Russian Academy of Sciences, Ural Division, Yekaterinburg, 620016 Russia

** e-mail: sadovski@iep.uran.ru*

Received June 9, 2005

We generalize the dynamical-mean field theory (DMFT) by including into the DMFT equations dependence on the correlation length of the pseudogap fluctuations via the additional (momentum dependent) self-energy $\Sigma_{\mathbf{k}}$. This self-energy describes nonlocal dynamical correlations induced by short-ranged collective SDW-like antiferromagnetic spin (or CDW-like charge) fluctuations. At high enough temperatures, these fluctuations can be viewed as a quenched Gaussian random field with finite correlation length. This generalized DMFT + $\Sigma_{\mathbf{k}}$ approach is used for the numerical solution of the weakly doped one-band Hubbard model with repulsive Coulomb interaction on a square lattice with nearest and next nearest neighbor hopping. The effective single impurity problem is solved by using a numerical renormalization group (NRG). Both types of strongly correlated metals, namely, (i) doped Mott insulator and (ii) the case of the bandwidth $W \lesssim U$ (U—value of local Coulomb interaction) are considered. By calculating profiles of the spectral densities for different parameters of the model, we demonstrate the qualitative picture of Fermi surface destruction and formation of Fermi arcs due to pseudogap fluctuations in qualitative agreement with the ARPES experiments. Blurring of the Fermi surface is enhanced with the growth of the Coulomb interaction. © *2005 Pleiades Publishing, Inc.*

PACS numbers: 71.10.Fd, 71.10.Hf, 71.27.+a, 71.30.+h, 74.72.–h

The pseudogap formation in the electronic spectrum of underdoped copper oxides [1, 2] is an especially striking anomaly of the normal state of high temperature superconductors. Despite continuing discussions on the nature of the pseudogap, we believe that the preferable scenario for its formation is most likely based on the model of strong scattering of the charge carriers by short-ranged antiferromagnetic (AFM, SDW) spin fluctuations [2, 3]. In momentum representation, this scattering transfers momenta of the order of $\mathbf{Q} = (\pi/a, \pi/a)$ (a—lattice constant of a two dimensional lattice). This leads to the formation of structures in the one-particle spectrum that are precursors of the changes in the spectra due to long-range AFM order (period doubling). As a result, we obtain non-Fermi liquidlike behavior (dielectrization) of the spectral density in the vicinity of the so-called hot spots on the Fermi surface appearing at intersections of the Fermi surface with the antiferromagnetic Brillouin zone boundary [2].

Within this spin-fluctuation scenario, a simplified model of the pseudogap state was studied [2, 4, 5] under the assumption that the scattering by dynamic spin fluctuations can be reduced for high enough temperatures to a static Gaussian random field (quenched disorder) of pseudogap fluctuations. These fluctuations are characterized by a scattering vector from the vicinity of $\mathbf{Q}$ with a width determined by the inverse correlation length of short-range order $\kappa = \xi^{-1}$ and by the appropriate energy scale Δ (typically of the order of the crossover temperature T^* to the pseudogap state [2]).

Undoped cuprates are antiferromagnetic Mott insulators with $U \gg W$ (U—value of the local Coulomb interaction, W—bandwidth of the noninteracting band), so that correlation effects are actually very important. It is thus clear that the electronic properties of underdoped (and, probably, also of optimally doped) cuprates are governed by strong electronic correlations too, so that these systems are typical strongly correlated metals. Two types of correlated metals can be distinguished: (i) the doped Mott insulator and (ii) the bandwidth controlled correlated metal $W \approx U$.

A state of the art tool to describe such correlated systems is the dynamical mean-field theory (DMFT) [6–10]. The characteristic features of correlated systems within the DMFT are the formation of incoherent structures (the so-called Hubbard bands) split by the Coulomb interaction U, and a quasiparticle (conduction) band near the Fermi level dynamically generated by the local correlations [6–10].

Unfortunately, the DMFT is not useful for the study of the antiferromagnetic scenario of pseudogap formation in strongly correlated metals. This is due to the basic approximation of the DMFT, which amounts to the complete neglect of nonlocal dynamical correlation effects [6–10]. As a result, within the standard DMFT approach, the Fermi surface of a quasiparticle band is not renormalized by interactions and just coincides

¶ The text was submitted by the authors in English.

with that of the bare quasiparticles [7]. Recently, we have formulated a semiphenomenological DMFT + $\Sigma_{\mathbf{k}}$ approach [11] allowing the introduction of a length scale (nonlocal correlations) into DMFT. Below, we present the basic points of this approach with application to the Fermi surface renormalization due to pseudogap fluctuations.

To include nonlocal effects while remaining within the usual impurity analogy of DMFT, we propose the following procedure. To be definite, let us consider a standard one-band Hubbard model. The major assumption of our approach is that the lattice and Matsubara time Fourier transform of the single-particle Green's function can be written as

$$G_{\mathbf{k}}(\omega) = \frac{1}{i\omega + \mu - \varepsilon(\mathbf{k}) - \Sigma(\omega) - \Sigma_{\mathbf{k}}(\omega)}, \quad (1)$$

where $\Sigma(\omega)$ is the local contribution to self-energy surviving in the DMFT ($\omega = \pi T(2n + 1)$), while $\Sigma_{\mathbf{k}}(\omega)$ is some momentum dependent part. We suppose that this last contribution is due to either electron interactions with some additional collective modes, order parameter fluctuations, or may be due to similar nonlocal contributions within the Hubbard model itself. To avoid possible confusion, we must stress that $\Sigma_{\mathbf{k}}(i\omega)$ can also contain a local (momentum independent) contribution that obviously vanishes in the limit of infinite dimensionality $d \longrightarrow \infty$ and is not taken into account within the standard DMFT. Due to this fact, there is no double counting problem within our approach for the Hubbard model. It is important to stress that the assumed additive form of self-energy $\Sigma(\omega) + \Sigma_{\mathbf{k}}(\omega)$ implicitly corresponds to the neglect of possible interference from these local (DMFT) and nonlocal contributions.

The self-consistency equations of our generalized DMFT + $\Sigma_{\mathbf{k}}$ approach are formulated as follows [11]:

(1) Start with some initial guess of the local self-energy $\Sigma(\omega)$; e.g., $\Sigma(\omega) = 0$.

(2) Construct $\Sigma_{\mathbf{k}}(\omega)$ within some (approximate) scheme taking into account the interactions with collective modes or order parameter fluctuations that in general can depend on $\Sigma(\omega)$ and μ.

(3) Calculate the local Green's function

$$G_{ii}(\omega) = \frac{1}{N}\sum_{\mathbf{k}} \frac{1}{i\omega + \mu - \varepsilon(\mathbf{k}) - \Sigma(\omega) - \Sigma_{\mathbf{k}}(\omega)}. \quad (2)$$

(4) Define the Weiss field

$$\mathcal{G}_0^{-1}(\omega) = \Sigma(\omega) + G_{ii}^{-1}(\omega). \quad (3)$$

(5) Using some impurity solver to calculate the single-particle Green's function for the effective Anderson impurity problem defined by Grassmann integral

$$G_d(\tau - \tau') = \frac{1}{Z_{\text{eff}}}\int Dc_{i\sigma}^{+} Dc_{i\sigma} c_{i\sigma}(\tau) c_{i\sigma}^{+}(\tau') \exp(-S_{\text{eff}}), \quad (4)$$

with effective action for a fixed (impurity) i

$$S_{\text{eff}} = -\int_0^\beta d\tau_1 \int_0^\beta d\tau_2 c_{i\sigma}(\tau_1)\mathcal{G}_0^{-1}(\tau_1 - \tau_2)c_{i\sigma}^{+}(\tau_2) + \int_0^\beta d\tau U n_{i\uparrow}(\tau) n_{i\downarrow}(\tau), \quad (5)$$

$Z_{\text{eff}} = \int Dc_{i\sigma}^{+} Dc_{i\sigma} \exp(-S_{\text{eff}})$, and $\beta = T^{-1}$. This step produces a new set of values $G_d^{-1}(\omega)$.

(6) Define a new local self-energy

$$\Sigma(\omega) = \mathcal{G}_0^{-1}(\omega) - G_d^{-1}(\omega). \quad (6)$$

(7) Using this self-energy as the initial one in step 1, continue the procedure until (and if) convergency is reached to obtain

$$G_{ii}(\omega) = G_d(\omega). \quad (7)$$

Eventually, we get the desired Green's function in the form of (1), where $\Sigma(\omega)$ and $\Sigma_{\mathbf{k}}(\omega)$ are those appearing at the end of our iteration procedure.

For the momentum dependent part of the single-particle self-energy, we concentrate on the effects of scattering of electrons from collective short-range SDW-like antiferromagnetic spin (or CDW-like charge) fluctuations. To calculate $\Sigma_{\mathbf{k}}(\omega)$ for an electron moving in the quenched random field of (static) Gaussian spin (or charge) fluctuations with dominant scattering momentum transfers from the vicinity of some characteristic vector $\mathbf{Q}$ (the hot spots model [2]), we use the following recursion procedure proposed in [12, 4, 5], which takes into account all the Feynman diagrams describing the scattering of electrons by this random field:

$$\Sigma_{\mathbf{k}}(\omega) = \Sigma_{n=1}(\omega\mathbf{k}), \quad (8)$$

with

$$\Sigma_n(\omega\mathbf{k}) = \Delta^2 \frac{s(n)}{i\omega + \mu - \Sigma(\omega) - \varepsilon_n(\mathbf{k}) + in v_n \kappa - \Sigma_{n+1}(\omega\mathbf{k})}. \quad (9)$$

The quantity Δ characterizes the energy scale, and $\kappa = \xi^{-1}$ is the inverse correlation length of short range SDW (CDW) fluctuations; $\varepsilon_n(\mathbf{k}) = \varepsilon(\mathbf{k} + \mathbf{Q})$ and $v_n = |v_{\mathbf{k}+\mathbf{Q}}^x| + |v_{\mathbf{k}+\mathbf{Q}}^y|$ for odd n, while $\varepsilon_n(\mathbf{k}) = \varepsilon(\mathbf{k})$ and $v_n = |v_{\mathbf{k}}^x| + |v_{\mathbf{k}}^y|$ for even n. The velocity projections $v_{\mathbf{k}}^x$ and $v_{\mathbf{k}}^y$ are determined by the usual momentum derivatives of the bare electronic energy dispersion $\varepsilon(\mathbf{k})$. Finally, $s(n)$ represents a combinatorial factor with

$$s(n) = n \quad (10)$$

for the case of commensurate charge (CDW type) fluctuations with $\mathbf{Q} = (\pi/a, \pi/a)$ [12]. For incommensurate CDW fluctuations [12], one finds

$$s(n) = \begin{cases} \dfrac{n+1}{2} & \text{for odd } n \\ \dfrac{n}{2} & \text{for even } n. \end{cases} \quad (11)$$

If we take into account the (Heisenberg) spin structure of the interaction with spin fluctuations in nearly antiferromagnetic Fermi liquid (the spin-fermion (SF) model [4]), the combinatorics of the diagrams becomes more complicated and the factor $s(n)$ acquires the following form [4]:

$$s(n) = \begin{cases} \dfrac{n+2}{3} & \text{for odd } n \\ \dfrac{n}{3} & \text{for even } n. \end{cases} \quad (12)$$

Obviously, with this procedure, we introduce an important length scale ξ not present in standard DMFT. Physically, this scale mimics the effect of the short-range (SDW or CDW) correlations within the fermionic bath surrounding the effective Anderson impurity. Both the parameters Δ and ξ can, in principle, be calculated from the microscopic model at hand [11].

In the following, we will consider both Δ and especially ξ as some phenomenological parameters to be determined from experiments. This makes our approach somehow similar in spirit to the Landau approach to Fermi liquids.

In the following, we discuss a standard one-band Hubbard model on a square lattice. With the nearest (t) and next nearest (t') neighbor hopping integrals, the bare dispersion then reads

$$\varepsilon(\mathbf{k}) = -2t(\cos k_x a + \cos k_y a) - 4t' \cos k_x a \cos k_y a, \quad (13)$$

where a is the lattice constant. The correlations are introduced by a repulsive, local two-particle interaction U. We choose as the energy scale the nearest neighbor hopping integral t and as the length scale the lattice constant a. All the energies below are given in units of t.

For a square lattice, the bare bandwidth is $W = 8t$. To study a strongly correlated metallic state obtained as a doped Mott insulator, we use $U = 40t$ as the value for the Coulomb interaction and a filling $n = 0.8$ (hole doping). The correlated metal in the case of $W \gtrsim U$ is considered for the case of $U = 4t$ and the filling factor $n = 0.8$ (hole doping). For Δ, we choose rather typical values between $\Delta = 0.1t$ and $\Delta = 2t$ (actually, the approximate limiting values obtained in [11]), and, for the correlation length, we took $\xi = 10a$ (being motivated mainly by the experimental data for cuprates [2, 4]).

The DMFT maps the lattice problem onto an effective, self-consistent impurity defined by Eqs. (4), (5). In our work, we employed as an impurity solver the reliable method of a numerical renormalization group (NRG) [13, 14].

As already discussed in the Introduction, the characteristic feature of the strongly correlated metallic state is the coexistence of lower and upper Hubbard bands split by the value of U with a quasiparticle peak at the Fermi level.

Once we get a self-consistent solution of the DMFT + $\Sigma_{\mathbf{k}}$ equations with nonlocal fluctuations, we can compute the spectral functions $A(\omega, \mathbf{k})$ for real ω:

$$A(\omega, \mathbf{k}) = -\frac{1}{\pi}\mathrm{Im}\frac{1}{\omega + \mu - \varepsilon(\mathbf{k}) - \Sigma(\omega) - \Sigma_{\mathbf{k}}(\omega)}, \quad (14)$$

where the self-energy $\Sigma(\omega)$ and chemical potential μ are calculated self-consistently. The densities of states can be calculated by integrating (14) over the Brillouin zone.

Extensive calculations of the densities of states, spectral densities, and ARPES spectra for this model were performed in [11]. In the general case, a pseudogap appears in the density of states within the quasiparticle peak (correlated conduction band). The qualitative behavior of the pseudogap anomalies is similar to those for the case of $U = 0$ [2, 5]; e.g., a decrease of ξ makes the pseudogap less pronounced, while reducing Δ narrows the pseudogap and also makes it more shallow. For the doped Mott insulator, we find that the pseudogap is remarkably more pronounced for the SDW-like fluctuations than for the CDW-like fluctuations. Thus, below, we present mainly the results obtained using combinatorics (12) of the spin-fermion model.

As was noted above, within the standard DMFT approach, the Fermi surface is not renormalized by interactions and just coincides with that of the bare quasiparticles [7]. However, in the case of the nontrivial momentum dependence of the electron self-energy, important renormalization of the Fermi surface appears due to pseudogap formation [4]. There are a number of ways to define a Fermi surface in a strongly correlated system with pseudogap fluctuations. In the following, we use intensity plots (within the Brillouin zone) of the spectral density (14) taken at $\omega = 0$. These are readily measured by ARPES, and the appropriate peak positions define the Fermi surface in the usual Fermi liquid with ease.

In Figs. 1a–1c, we show such plots for the case of uncorrelated metal ($U = 0$) with pseudogap fluctuations obtained directly from the Green's function defined by the recursion procedure (8), (9). For comparison, in Fig. 1d, we show renormalized Fermi surfaces obtained for this model using a rather natural definition of the Fermi surface as defined by the solution of the equation

$$\omega - \varepsilon(\mathbf{k}) + \mu - \mathrm{Re}\Sigma(\omega) - \mathrm{Re}\Sigma_{\mathbf{k}}(\omega) = 0 \quad (15)$$

for $\omega = 0$, which was used, e.g., in [4]. It is seen that this last definition produces Fermi surfaces close to those defined by the intensity plots of the spectral density

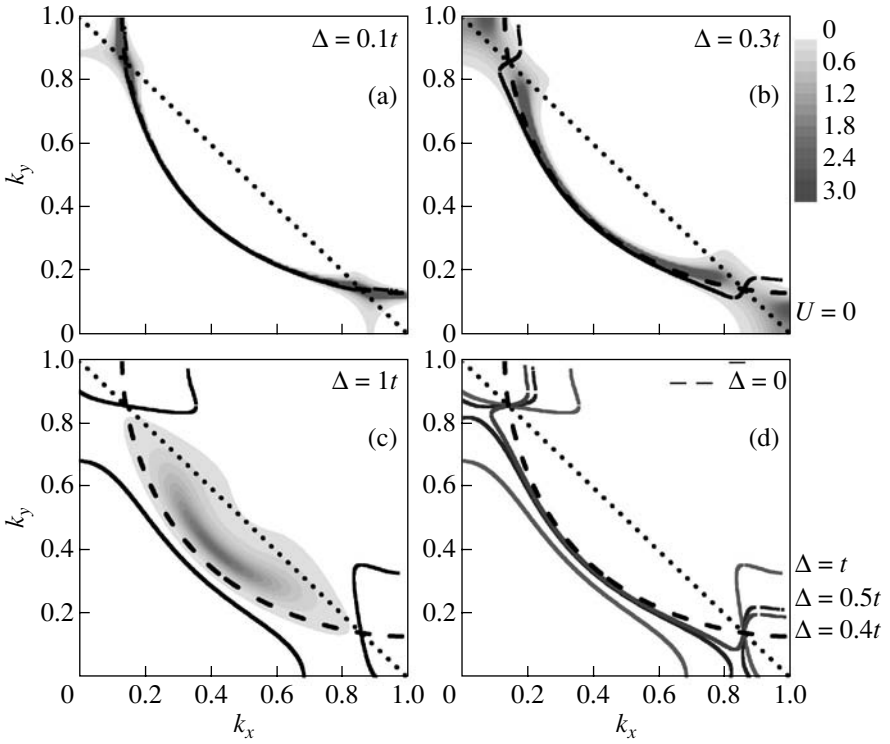

Fig. 1. Fermi surfaces obtained for the uncorrelated case of $U = 0$ and the filling factor $n = 0.8$. Shown are intensity plots of the spectral density (14) for $\omega = 0$. Δ = (a) $0.1t$; (b) $0.3t$; (c) t; (d) Fermi surfaces obtained solving Eq. (15). The dashed line denotes a bare Fermi surface.

only for small values of Δ, while, for larger values, we can see a rather unexpected topological transition. At the same time, the spectral density intensity plots clearly demonstrate destruction of the Fermi surface in the vicinity of the hot spots with Fermi arcs forming with the growth of Δ similar to those seen in the pioneering ARPES experiments of Norman *et al.* [15] and confirmed later in numerous works.

In Fig. 2, we show our results for the case of correlated metal with $U = 4t$, and, in Fig. 3, for the doped Mott insulator with $U = 40t$. Again, we see the qualitative behavior clearly demonstrating the destruction of the well defined Fermi surface in the strongly correlated metal with the growth of the pseudogap amplitude Δ. The role of finite U reduces to a lower intensity of spectral density in comparison with the case of $U = 0$ and leads to additional blurring, thus, making the hot spots less visible. Again, the destruction of the Fermi surface starts in the vicinity of the hot spots for small values of Δ, but, almost immediately, it disappears in the whole antinodal region of the Brillouin zone, while only Fermi arcs remain in the nodal region very close to the bare Fermi surface. These results give a natural explanation for the observed behavior and also for the fact that the existence of regions of hot spots was observed only in some rare cases [16].

For the case of the doped Mott insulator ($U = 40t$) shown in Fig. 3, we see that the Fermi surface is rather poorly defined for all the values of Δ, as the spectral density profiles are much more blurred than in the case of smaller values of U, thus, reflecting the important role of correlations.

It is interesting to note that, from Figs. 2 and 3, it is clearly seen that the natural definition of the Fermi surface from Eq. (15) is quite inadequate for correlated systems with finite U and nonlocal interactions (pseudogap fluctuations), thus, signifying the increased role of strong correlations.

To summarize, we propose a generalized DMFT + $\Sigma_{\mathbf{k}}$ approach that is meant to take into account the important effects due to nonlocal correlations in a systematic but, to some extent, phenomenological fashion. The main idea of this extension is to stay within the usual effective Anderson impurity analogy and introduce length scale dependence due to nonlocal correlation via the effective medium (bath) appearing in the standard DMFT. This becomes possible by incorporating scattering processes of fermions in the bath from nonlocal collective SDW-like antiferromagnetic spin (or CDW-like charge) fluctuations. Such a generalization of the DMFT allows one to overcome the well-known shortcoming of the **k** independence of the self-energy of the standard DMFT. It, in turn, opens the possibility to access the physics of low-dimensional strongly correlated systems where different types of spatial fluctuations (e.g., of some order parameter)

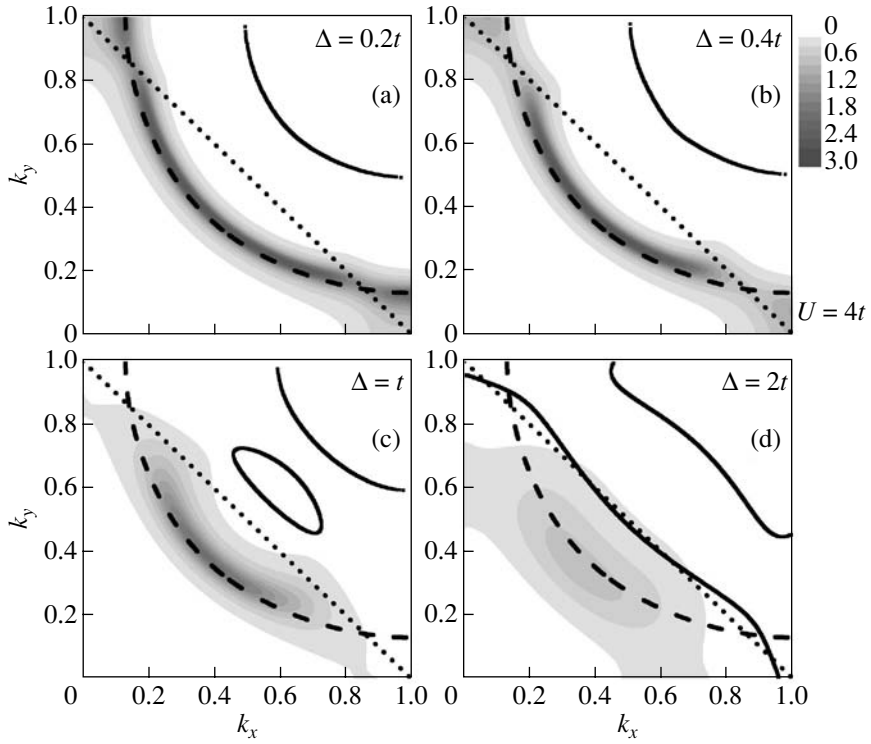

Fig. 2. Destruction of the Fermi surface as obtained from the DMFT + $\Sigma_{\mathbf{k}}$ calculations for $U = 4t$ and $n = 0.8$. The notations are the same as used in Fig. 1. Δ = (a) $0.2t$; (b) $0.4t$; (c) t; (d) $2t$. Black lines show the solution of Eq. (15).

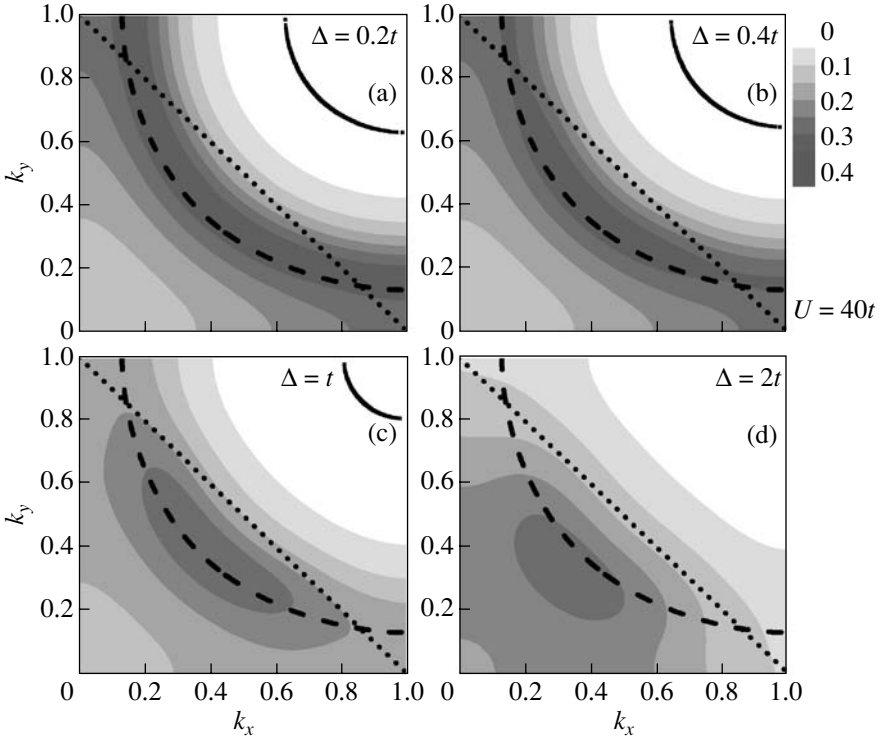

Fig. 3. Fermi surfaces obtained from the DMFT + $\Sigma_{\mathbf{k}}$ calculations for $U = 40t$ and $n = 0.8$. The other parameters and notations are the same as in Fig. 2.

become important in a nonperturbative way (at least with respect to the important local dynamical correlations). However, we must stress that our procedure in no way introduces any kind of systematic $1/d$ expansion, being only a qualitative method to include a length scale into DMFT.

In our present study, we addressed the problem of the Fermi surface renormalization (destruction) by pseudogap fluctuations in the strongly correlated metallic state. Our generalization of DMFT leads to nontrivial and, in our opinion, physically sensible **k** dependence of spectral functions, thus, leading to Fermi surface renormalization quite similar to that observed in ARPES experiments.

Similar results were obtained in recent years using the cluster mean-field theories [17]. The major advantage of our approach over these cluster mean-field theories is that we stay in an effective single-impurity representation. This means that our approach is computationally much less costly and therefore easily generalizable for the description of additional interactions.

We are grateful to Th. Pruschke for providing us with his NRG code and helpful discussions. This work was supported in part by the Russian Foundation for Basic Research (project nos. 05-02-16301, 05-02-17244); the program of the Presidium of the Russian Academy of Sciences (RAS) "Quantum Macrophysics"; and the program of the Division of Physical Sciences of the RAS "Strongly Correlated Electrons in Semiconductors, Metals, Superconductors, and Magnetic Materials." I.N. acknowledges support from the Dynasty Foundation, the International Centre for Fundamental Physics in Moscow "Program for Young Scientists 2005," and the Russian Science Support Foundation "Program for Young Candidates of the Russian Academy of Sciences 2005."

REFERENCES

1. T. Timusk and B. Statt, Rep. Prog. Phys. **62**, 61 (1999).
2. M. V. Sadovskii, Usp. Fiz. Nauk **171**, 539 (2001) [Phys. Usp. **44**, 515 (2001)].
3. D. Pines, cond-mat/0404151.
4. J. Schmalian, D. Pines, and B. Stojkovic, Phys. Rev. B **60**, 667 (1999).
5. E. Z. Kuchinskii and M. V. Sadovskii, Zh. Éksp. Teor. Fiz. **115**, 1765 (1999) [JETP **88**, 347 (1999)].
6. W. Metzner and D. Vollhardt, Phys. Rev. Lett. **62**, 324 (1989).
7. D. Vollhardt, in *Correlated Electron Systems*, Ed. by V. J. Emery (World Sci., Singapore, 1993), p. 57.
8. Th. Pruschke, M. Jarrell, and J. K. Freericks, Adv. Phys. **44**, 187 (1995).
9. A. Georges, G. Kotliar, W. Krauth, and M. J. Rozenberg, Rev. Mod. Phys. **68**, 13 (1996).
10. G. Kotliar and D. Vollhardt, Phys. Today **57** (3), 53 (2004).
11. M. V. Sadovskii, I. A. Nekrasov, E. Z. Kuchinskii, *et al.*, cond-mat/0502612.
12. M. V. Sadovskii, Zh. Éksp. Teor. Fiz. **77**, 2070 (1979) [Sov. Phys. JETP **50**, 989 (1979)].
13. K. G. Wilson, Rev. Mod. Phys. **47**, 773 (1975); H. R. Krishna-murthy, J. W. Wilkins, and K. G. Wilson, Phys. Rev. B **21**, 1003 (1980); Phys. Rev. B **21**, 1044 (1980); A. C. Hewson, *The Kondo Problem to Heavy Fermions* (Cambridge Univ. Press, Cambridge, 1993).
14. R. Bulla, A. C. Hewson, and Th. Pruschke, J. Phys.: Condens. Matter **10**, 8365 (1998); R. Bulla, Phys. Rev. Lett. **83**, 136 (1999).
15. M. R. Norman, M. Randeria, J. C. Campuzano, *et al.*, Nature **382**, 51 (1996).
16. N. P. Armitage, D. H. Lu, C. Kim, *et al.*, Phys. Rev. Lett. **87**, 147003 (2001).
17. Th. Maier, M. Jarrell, Th. Pruschke, and M. Hettler, Rev. Mod. Phys. (in press); cond-mat/0404055.

JETP Letters, Vol. 82, No. 4, 2005, pp. 204–209. From Pis'ma v Zhurnal Éksperimental'noĭ i Teoreticheskoĭ Fiziki, Vol. 82, No. 4, 2005, pp. 223–227.

Type-IV Superconductivity: Cooper Pairs with Broken Inversion and Time-Reversal Symmetries in Conventional Superconductors¶

A. G. Lebed

Department of Physics, University of Arizona, 1118 E. 4th Street, Tucson, AZ 85721, USA
Landau Institute for Theoretical Physics, ul. Kosygina 2, Moscow, 117940 Russia

Received June 29, 2005

The vortex phase in a singlet superconductor in the absence of impurities is shown to be absolutely unstable with respect to the appearance of a triplet component that breaks both the inversion and time-reversal symmetries of Cooper pairs. The symmetry breaking paramagnetic effects are demonstrated to be of the order of unity if the orbital upper critical field, $H_{c2}(0)$, is of the order of the Clogston paramagnetic limiting field, H_p. We suggest a generic phase diagram of such a type-IV superconductor that is a singlet one at $H = 0$ and characterized by a mixed singlet–triplet order parameter with broken time-reversal symmetry in the vortex phase. The possibility to observe type-IV superconductivity in clean organic, high-T_c, MgB_2, and other superconductors is discussed. © *2005 Pleiades Publishing, Inc.*

PACS numbers: 74.20.Rp, 74.25.Op, 74.70.–b

It is well known that the Meissner effect, which is the main feature of superconductivity phenomenon, is used to classify superconducting materials. In type-I superconductors, where the Meissner effect is complete, the superconductivity is destroyed at $H > H_c$ (where H_c is the thermodynamic critical field), whereas, in type-II superconductors, the superconductivity phenomenon survives at higher magnetic fields, $H_{c1} < H < H_{c2}$ (where $H_{c1} < H_c < H_{c2}$), in the form of Abrikosov vortices [1, 2]. Type-II superconductors can be subdivided into two main classes: superconducting alloys (or dirty superconductors) [1, 2] and relatively clean superconductors, where the type-II superconductivity is due to the anisotropy of their electron spectra and the relatively high effective masses of quasiparticles [3]. Due to the success in the synthesis of novel materials, a number of new classes of relatively clean type-II superconductors were discovered during the last 30 years, including organic [4, 5], heavy-fermion [6], high-T_c [7], Sr_2RuO_4 [8], MgB_2 [9], and other superconductors. Currently, the above mentioned relatively clean type-II superconductors are the most interesting and important materials both from the fundamental point of view and from point of view of their possible applications.

Usually, the orbital superconducting order parameter, $\Delta(\mathbf{r}_1, \mathbf{r}_2)$, corresponding to the pairing of two electrons in a Cooper pair can be expressed in the form $\Delta(\mathbf{r}_1, \mathbf{r}_2) = \Delta(\mathbf{R})\hat{\Delta}(\mathbf{r})$. [Here, the external order parameter $\Delta(\mathbf{R})$ is related to the motion of the center of mass of the Cooper pair, $\mathbf{R} = (\mathbf{r}_1 + \mathbf{r}_2)/2$, whereas the internal order parameter $\hat{\Delta}(\mathbf{r})$ describes the relative motion of the electrons in the Cooper pair, $\mathbf{r} = \mathbf{r}_1 - \mathbf{r}_2$.] From this point of view, type-II superconductors in their vortex phases are characterized by broken symmetries of the external order parameter, $\Delta(\mathbf{r})$, which is responsible for Meissner currents [1, 2].

Other important issues are the symmetries of the internal orbital order parameter, $\hat{\Delta}(\mathbf{r})$ (or its Fourier component $\hat{\Delta}(\mathbf{k})$), and the related spin part of the superconducting order parameter $\hat{\Delta}(\sigma_1, \sigma_2)$. In accordance with Fermi statistics, the internal order parameter $\hat{\Delta}(\mathbf{k})$ is an even function of variable $\mathbf{k}$ in the case of singlet superconductivity (where the total spin of the Cooper pair $|\mathbf{S}| = 0$), whereas $\hat{\Delta}(\mathbf{k})$ is an odd function of $\mathbf{k}$ in the case of triplet superconductivity (where $|\mathbf{S}| = 1$) [10, 11]. Depending on the symmetry properties of $\hat{\Delta}(\mathbf{k})$, superconductors are subdivided into conventional ones [1, 2] (where the superconductivity can be described in terms of BCS *s*-wave singlet pairing) and unconventional ones [10, 11] (where the symmetry of $\hat{\Delta}(\mathbf{k})$ is lower than the underlying symmetry of the crystalline lattice).

It is commonly believed [1, 2, 10, 11] that the magnetic field does not change the internal superconducting order parameters (i.e., the wave functions $\hat{\Delta}(\mathbf{k})$ and $\hat{\Delta}(\sigma_1, \sigma_2)$) and, thus, Cooper pairs can be considered as

¶ The text was submitted by the author in English.

unchanged elementary particles in the Abrikosov vortex phase. Moreover, although related to the external degrees of freedom, Meissner currents break the time-reversal symmetry of $\Delta(\mathbf{R})$; the internal orbital and spin order parameters, $\hat{\Delta}(\mathbf{k})$ and $\hat{\Delta}(\sigma_1, \sigma_2)$, are believed to preserve $t \longrightarrow -t$ symmetry. The main goal of our letter is to show that type-IV superconductors [12] have to exist that exhibit qualitatively different magnetic properties and are characterized by Cooper pairing with broken time reversal, $t \longrightarrow -t$, and inversion, $\mathbf{k} \longrightarrow -\mathbf{k}$, symmetries of internal order parameters in the vortex phase. (Note that we define type-IV superconductivity as singlet superconductivity at $H = 0$ and in the Meissner phase that exhibits broken symmetries of Cooper pairs' internal wave functions in the vortex phase.)

More precisely, below, we suggest and prove the following theorem: each singlet type-II superconductor in the absence of impurities is actually a type-IV superconductor with broken $t \longrightarrow -t$ and $\mathbf{k} \longrightarrow -\mathbf{k}$ symmetries of internal order parameters in the vortex phase provided that the effective constant responsible for triplet (p-wave) superconducting pairing is not zero, $g_t \neq 0$. We show that the above mentioned theorem is due to careful account for paramagnetic spin splitting effects in the vortex phase, which have been dealt with so far only in the case $g_t = 0$ [1, 2, 10, 11, 13]. In particular, we demonstrate that the superconducting internal order parameter is a mixture of a singlet component $\hat{\Delta}_s(\mathbf{k})$ with a triplet component $i\hat{\Delta}_t(\mathbf{k})$, which breaks both the inversion $\mathbf{k} \longrightarrow -\mathbf{k}$ and time-reversal $t \longrightarrow -t$ symmetries due to an imaginary coefficient i. We point out that the above mentioned effects of singlet–triplet mixing are expected to be of the order of unity in a number of modern relatively clean type-II superconductors, where $H_{c2}(0) \sim H_p$ (see the Discussion at the end of this letter). Here, $H_{c2}(0)$ is the orbital upper critical field at $T = 0$ [1, 2, 10, 11] and H_p is the Clogston paramagnetic limiting field [13, 1].

Although, in this letter, we consider the vortex phase with broken symmetries only in the Ginzburg–Landau (GL) region of an s-wave layered superconductor in a parallel magnetic field, we stress that the suggested theorem is very general and based only on symmetry arguments. As we argue below, the above mentioned theorem is a consequence of broken spin symmetry (due to paramagnetic spin splitting effects) [13] and the broken translational symmetry of the external orbital order parameter $\Delta(\mathbf{R})$ in the vortex phase. As a result, the theorem suggested in the letter has to be valid for any s- and d-wave singlet superconductor [14] for both attractive and repulsive electron–electron interactions in a triplet (p-wave) channel.

In other words, our main message is that Cooper pairs cannot be considered as unchanged elementary particles in a magnetic field in modern type-II superconductors, where $H_{c2}(0) \sim H_p$. As shown below, magnetic fields of the order of $H \sim H_p$ qualitatively change the nature of Cooper pairs in the vortex phase. We suggest that, in relatively clean conventional type-II superconductors, there has to exist the forth critical magnetic field, $H_{c4}(T)$, corresponding to phase transition (or crossover) between the Abrikosov vortex phase and exotic vortex phase, where the inversion and time-reversal symmetries of Cooper pairs are broken and, thus, topologic properties of vortices are unusual (see Fig. 1).

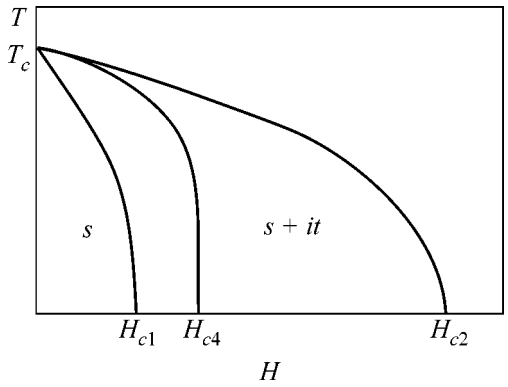

Fig. 1. A phase diagram of a type-IV superconductor, which is a singlet one at $H = 0$ and in the Meissner phase, $0 < H < H_{c1}(T)$, and characterized by broken inversion and time-reversal symmetries at low temperatures and high magnetic fields, $H_{c4}(T) < H < H_{c2}(T)$. In the intermediate region of magnetic fields $H_{c1}(T) < H < H_{c4}(T)$, broken symmetries may be absent or marginal.

First, let us qualitatively explain why paramagnetic effects lead to the appearance of a triplet component in the vortex phase of a conventional singlet superconductor. It is well known [10, 11] that the spin component of a singlet order parameter is an antisymmetric function of spin variables, $\hat{\Delta}_s(+, -) = -\hat{\Delta}_s(-, +)$. In the presence of Abrikosov vortices, the external order parameter $\Delta(\mathbf{R})$ varies with the coordinate $\mathbf{R}$, which corresponds to the superconducting pairing of electrons with nonzero total momenta of Cooper pairs of the order of $|\mathbf{p}| \simeq \hbar/\xi$, where ξ is the coherence length [1, 2, 10, 11]. Let us consider superconducting pairing of two electrons with the total momentum $|\mathbf{p}_0| \neq 0$ in the presence of spin splitting paramagnetic effects (see Fig. 2). As is seen from Fig. 2, the absolute value of the spin component $\Delta(+, -)$ is not equal to the absolute value of the spin component $\Delta(-, +)$ if $|\mathbf{p}_0| \neq 0$. This means that $\Delta(+, -) \neq -\Delta(-, +)$ and, in addition to the singlet order parameter, a triplet component corresponding to superconducting pairing with $|\mathbf{S}| = 1$ and $S_y = 0$ appears, where S_y is a component of the total spin of the Cooper pair along the magnetic field direction.

Below, we quantitatively describe superconducting pairing with an internal order parameter exhibiting broken inversion and time-reversal symmetries in a singlet

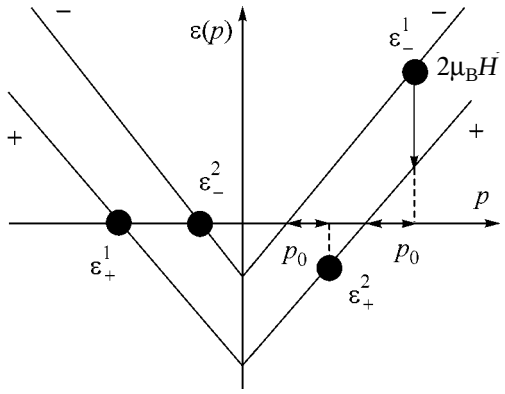

Fig. 2. In a magnetic field, electron spectra with spin up and spin down are split, $\epsilon_+(p) = \epsilon_0(p) - \mu_B H$ and $\epsilon_-(p) = \epsilon_0(p) + \mu_B H$, respectively. Two Cooper pairs with spin parts of internal wave functions, $\Delta(+, -)$ and $\Delta(-, +)$, and total momenta $p_0 \neq 0$ are characterized by different probabilities to exist since the energy difference $|\epsilon_+^1 - \epsilon_-^1| = p_0 v_F + 2\mu_B H$ is not equal to the energy difference $|\epsilon_-^2 - \epsilon_+^2| = -p_0 v_F + 2\mu_B H$ if $p_0 \neq 0$. (For simplicity, a linearized one-dimensional electron spectrum, $\epsilon(p) = v_F|p|$, is considered.)

s-wave superconductor with a layered electron spectrum,

$$\epsilon_0(\mathbf{p}) = (p_x^2 + p_y^2)/2m + 2t_z\cos(p_z d), \quad \epsilon_F = m v_F^2/2, \tag{1}$$

in a magnetic field:

$$\mathbf{H} = (0, H, 0), \quad \mathbf{A} = (0, 0, -Hx). \tag{2}$$

In the case where the electron–electron interactions do not depend on the electron spins, the total Hamiltonian of the electron system can be written as follows:

$$\hat{H} = \hat{H}_0 + \hat{H}_{\text{int}}, \quad \hat{H}_0 = \sum_{\mathbf{p},\sigma} \epsilon_\sigma(\mathbf{p}) c_\sigma^+(\mathbf{p}) c_\sigma(\mathbf{p}),$$

$$\hat{H}_{\text{int}} = \frac{1}{2}\sum_{\mathbf{q},\sigma}\sum_{\mathbf{p},\mathbf{p}_1} U(\mathbf{p}, \mathbf{p}_1) c_\sigma^+\left(\mathbf{p} + \frac{\mathbf{q}}{2}\right) \tag{3}$$

$$\times c_{-\sigma}^+\left(-\mathbf{p} + \frac{\mathbf{q}}{2}\right) c_{-\sigma}\left(-\mathbf{p}_1 + \frac{\mathbf{q}}{2}\right) c_\sigma\left(\mathbf{p}_1 + \frac{\mathbf{q}}{2}\right),$$

where $\sigma = \pm 1$, $\epsilon_\sigma(\mathbf{p}) = \epsilon_0(\mathbf{p}) - \sigma\mu_B H$, and $c_\sigma^+(\mathbf{p})$ and $c_\sigma(\mathbf{p})$ are electron creation and annihilation operators. As usual [10, 11], electron–electron interactions are subdivided into singlet and triplet channels:

$$U(\mathbf{p}, \mathbf{p}_1) = U_s(\mathbf{p}, \mathbf{p}_1) + U_t(\mathbf{p}, \mathbf{p}_1),$$
$$U_s(\mathbf{p}, \mathbf{p}_1) = U_s(-\mathbf{p}, \mathbf{p}_1) = U_s(\mathbf{p}, -\mathbf{p}_1), \tag{4}$$
$$U_t(\mathbf{p}, \mathbf{p}_1) = -U_t(-\mathbf{p}, \mathbf{p}_1) = -U_t(\mathbf{p}, -\mathbf{p}_1).$$

Below, we define normal and anomalous (Gorkov) Green functions in the standard way [15, 16]:

$$G_{\sigma,\sigma}(\mathbf{p}, \mathbf{p}_1; \tau) = -\langle T_\tau c_\sigma(\mathbf{p}, \tau) c_\sigma^+(\mathbf{p}_1, 0)\rangle,$$
$$F_{\sigma,-\sigma}(\mathbf{p}, \mathbf{p}_1; \tau) = \langle T_\tau c_\sigma(\mathbf{p}, \tau) c_{-\sigma}(-\mathbf{p}_1, 0)\rangle, \tag{5}$$
$$F_{\sigma,-\sigma}^+(\mathbf{p}, \mathbf{p}_1; \tau) = \langle T_\tau c_\sigma^+(-\mathbf{p}, \tau) c_{-\sigma}^+(\mathbf{p}_1, 0)\rangle,$$

where $\langle\ldots\rangle$ stands for the Gibbs averaging procedure with Hamiltonian (3).

If we define the singlet and triplet superconducting order parameters [10, 11],

$$\Delta_s(\mathbf{p}, \mathbf{q}) = -\frac{1}{2}\sum_{\mathbf{p}_1} U_s(\mathbf{p}, \mathbf{p}_1) T$$
$$\times \sum_{\omega_n}\left[F_{+,-}\left(i\omega_n; \mathbf{p}_1 + \frac{\mathbf{q}}{2}, \mathbf{p}_1 - \frac{\mathbf{q}}{2}\right)\right.$$
$$\left. - F_{-,+}\left(i\omega_n; \mathbf{p}_1 + \frac{\mathbf{q}}{2}, \mathbf{p}_1 - \frac{\mathbf{q}}{2}\right)\right], \tag{6}$$
$$\Delta_t(\mathbf{p}, \mathbf{q}) = -\frac{1}{2}\sum_{\mathbf{p}_1} U_t(\mathbf{p}, \mathbf{p}_1) T$$
$$\times \sum_{\omega_n}\left[F_{+,-}\left(i\omega_n; \mathbf{p}_1 + \frac{\mathbf{q}}{2}, \mathbf{p}_1 - \frac{\mathbf{q}}{2}\right)\right.$$
$$\left. + F_{-,+}\left(i\omega_n; \mathbf{p}_1 + \frac{\mathbf{q}}{2}, \mathbf{p}_1 - \frac{\mathbf{q}}{2}\right)\right],$$

then, using the Green-function technique [10, 11, 15, 16], we obtain the following equations:

$$[i\omega_n - \epsilon_\sigma(\mathbf{p})] G_{\sigma,\sigma}(i\omega_n; \mathbf{p}, \mathbf{p}_1)$$
$$+ \sum_{\mathbf{q}} [\sigma\Delta_s(\mathbf{p}, \mathbf{q}) + \Delta_t(\mathbf{p}, \mathbf{q})]$$
$$\times F_{-\sigma,\sigma}^+(i\omega_n; \mathbf{p} - \mathbf{q}, \mathbf{p}_1) = \delta(\mathbf{p} - \mathbf{p}_1),$$
$$[i\omega_n - \epsilon_\sigma(\mathbf{p})] F_{\sigma,-\sigma}(i\omega_n; \mathbf{p}, \mathbf{p}_1)$$
$$- \sum_{\mathbf{q}} [\sigma\Delta_s(\mathbf{p}, \mathbf{q}) + \Delta_t(\mathbf{p}, \mathbf{q})] \tag{7}$$
$$\times G_{-\sigma,-\sigma}(-i\omega_n; -\mathbf{p}_1, -\mathbf{p} + \mathbf{q}) = 0,$$
$$[i\omega_n + \epsilon_\sigma(\mathbf{p})] F_{\sigma,-\sigma}^+(i\omega_n; \mathbf{p}, \mathbf{p}_1)$$
$$+ \sum_{\mathbf{q}} [\sigma\Delta_s^+(\mathbf{p}, \mathbf{q}) + \Delta_t^+(\mathbf{p}, \mathbf{q})]$$
$$\times G_{\sigma,\sigma}(i\omega_n; \mathbf{p} + \mathbf{q}, \mathbf{p}_1) = 0,$$

which extend the Gorkov equations [15, 16] to the case of the coexistence of singlet and triplet order parameters (6). (Note that Eqs. (7), which were suggested in the letter, are rather general and describe the coexistence of triplet and singlet order parameters for spin independent electron–electron interactions at arbitrary temperatures.)

The goal of our letter is to solve Eqs. (7) in the case when layered superconductor (1) is placed in a parallel magnetic field (2). Below, we consider a phase transition line between the metallic and singlet–triplet mixed superconducting phases in the GL region (i.e., at $(T_c - T)/T_c \ll 1$), where T_c is the transition temperature from the metallic state to the *s*-wave singlet phase at $H = 0$. For this purpose, we linearize [17, 10, 11] Eqs. (7) with respect to the superconducting order parameters $\Delta_s(\mathbf{p}, \mathbf{q})$ and $\Delta_t(\mathbf{p}, \mathbf{q})$. As a result, we obtain the following system of linear equations:

$$\begin{aligned}
\Delta_s(\mathbf{p}, \mathbf{q}) &= -\frac{1}{2}\sum_{\mathbf{p}_1} U_s(\mathbf{p}, \mathbf{p}_1)T \\
&\times \sum_{\omega_n} [\Delta_s(\mathbf{p}_1, \mathbf{q})S_+(i\omega_n; \mathbf{p}_1, \mathbf{q}) \\
&+ \Delta_t(\mathbf{p}_1, \mathbf{q})S_-(i\omega_n; \mathbf{p}_1, \mathbf{q})], \\
\Delta_t(\mathbf{p}, \mathbf{q}) &= -\frac{1}{2}\sum_{\mathbf{p}_1} U_t(\mathbf{p}, \mathbf{p}_1)T \\
&\times \sum_{\omega_n} [\Delta_t(\mathbf{p}_1, \mathbf{q})S_+(i\omega_n; \mathbf{p}_1, \mathbf{q}) \\
&+ \Delta_s(\mathbf{p}_1, \mathbf{q})S_-(i\omega_n; \mathbf{p}_1, \mathbf{q})], \\
S_+(i\omega_n; \mathbf{p}_1, \mathbf{q}) &= G_+^0\left(i\omega_n, \mathbf{p}_1 + \frac{\mathbf{q}}{2}\right)G_-^0\left(-i\omega_n, -\mathbf{p}_1 + \frac{\mathbf{q}}{2}\right) \\
&+ G_-^0\left(i\omega_n, \mathbf{p}_1 + \frac{\mathbf{q}}{2}\right)G_+^0\left(-i\omega_n, -\mathbf{p}_1 + \frac{\mathbf{q}}{2}\right), \\
S_-(i\omega_n; \mathbf{p}_1, \mathbf{q}) &= G_+^0\left(i\omega_n, \mathbf{p}_1 + \frac{\mathbf{q}}{2}\right)G_-^0\left(-i\omega_n, -\mathbf{p}_1 + \frac{\mathbf{q}}{2}\right) \\
&- G_-^0\left(i\omega_n, \mathbf{p}_1 + \frac{\mathbf{q}}{2}\right)G_+^0\left(-i\omega_n, -\mathbf{p}_1 + \frac{\mathbf{q}}{2}\right),
\end{aligned} \tag{8}$$

where $G_\sigma^0(i\omega_n, \mathbf{p}) = 1/[i\omega_n - \epsilon_\sigma(\mathbf{p})]$ is the Green function of a free electron in the presence of paramagnetic spin splitting effects. One of the main results of our letter is that the terms with $S_-(i\omega_n, \mathbf{p}_1, \mathbf{q})$, mixing singlet and triplet superconducting pairings, are not equal to zero (see Fig. 2). Therefore, in the Abrikosov vortex phase, the singlet component of the superconducting order parameter always coexists with the triplet one, which breaks the inversion symmetry of the Cooper pairs.

As an example, let us consider the coexistence of singlet *s*-wave and triplet *p*-wave order parameters where

$$\begin{aligned}
U_s(\mathbf{p}, \mathbf{p}_1) &= -(2\pi/v_F)g_s, \\
U_t(\mathbf{p}, \mathbf{p}_1) &= -(4\pi/v_F)g_t\cos(\phi - \phi_1), \\
g_s &> 0, \quad g_s > g_t,
\end{aligned} \tag{9}$$

with ϕ and ϕ_1 being polar angles corresponding to the momenta $\mathbf{p}$ and $\mathbf{p}_1$, respectively. [Note that the inequalities $g_s > 0$ and $g_s > g_t$ correspond to stabilization of singlet *s*-wave superconductivity at $H = 0$.] After substituting Eqs. (9) in Eqs. (8), we can represent the singlet and triplet components of the order parameter as follows: $\Delta_s(\mathbf{p}, \mathbf{q}) = \Delta_s(\mathbf{q})$ and $\Delta_t(\mathbf{p}, \mathbf{q}) = \cos\phi\Delta_t(\mathbf{q})$, which satisfy the equations

$$\begin{aligned}
\Delta_s(\mathbf{q}) &= g_sA\Delta_s(\mathbf{q}) + g_sB\Delta_t(\mathbf{q}), \\
\Delta_t(\mathbf{q}) &= g_tC\Delta_t(\mathbf{q}) + g_tD\Delta_s(\mathbf{q}).
\end{aligned} \tag{10}$$

Since the *z*-component of the vector potential (2) depends only on the coordinate *x*, we may consider that $q_y = 0$ in Eqs. (10). Below, we calculate the quantities *A*, *B*, *C*, and *D* in the GL region [3, 18, 10, 11], which corresponds to their expansions as power series in the small parameters $v_Fq_x/T_c \ll 1$, $t_zdq_z/T_c \ll 1$, and $\mu_BH/T_c \ll 1$. As a result, we obtain

$$\begin{aligned}
A &\simeq (\pi T)\sum_{\omega_n > 0}^{\Omega}\left[\frac{2}{\omega_n} - \frac{1}{4\omega_n^3}(v_F^2q_x^2 + 4t_z^2q_z^2d^2 + 8\mu_b^2H^2)\right], \\
B &\simeq -\sqrt{2}\mu_BHv_Fq_x(\pi T_c)\sum_{\omega_n > 0}^{\infty}\frac{1}{\omega_n^3}, \\
C &\simeq (\pi T)\sum_{\omega_n > 0}^{\Omega}\left[\frac{2}{\omega_n}\right. \\
&\left. - \frac{1}{4\omega_n^3}(3v_F^2q_x^2/2 + 4t_z^2q_z^2d^2 + 8\mu_b^2H^2)\right], \\
D &= B,
\end{aligned} \tag{11}$$

where Ω is the cut-off energy.

We introduce magnetic field (2) in Eqs. (11) using a standard quasi-classical eiconal approximation [17, 18, 10, 11]: $q_x \longrightarrow -i(d/dx)$, $q_z/2 \longrightarrow eA_z/c = eHx/c$, which

leads to the following matrix GL equations extended to the case of triplet–singlet coexistence

$$\left[\tau + \xi_{\|}^2\frac{d^2}{dx^2} - \frac{(2\pi\xi_{\perp})^2}{\phi_0^2}H^2x^2\right]\Delta_s(x)$$
$$+ i\frac{\sqrt{7\zeta(3)}}{\sqrt{2}\gamma}\xi_{\|}\left(\frac{H}{H_p}\right)\frac{d\Delta_t(x)}{dx} = 0,$$
$$\left[\frac{g_t - g_s}{g_t g_s} + \frac{3}{2}\xi_{\|}^2\frac{d^2}{dx^2} - \frac{(2\pi\xi_{\perp})^2}{\phi_0^2}H^2x^2\right]\Delta_t(x) \quad (12)$$
$$+ i\frac{\sqrt{7\zeta(3)}}{\sqrt{2}\gamma}\xi_{\|}\left(\frac{H}{H_p}\right)\frac{d\Delta_s(x)}{dx} = 0,$$

where $\tau = (T_c - T)/T_c \ll 1$, $\xi_{\|} = \sqrt{7\zeta(3)}\,v_F/4\sqrt{2}\,\pi T_c$, $\xi_{\perp} = \sqrt{7\zeta(3)}\,t_z d/2\sqrt{2}\,\pi T_c$ are the GL coherence lengths [3, 1, 2]; ϕ_0 is a flux quantum; $\zeta(z)$ is the Riemann zeta-function; γ is the Euler constant; and H_p is the Clogston paramagnetic limiting field [13].

In the case where $g_s - g_t \sim g_s$, Eqs. (12) have the following solutions:

$$\Delta_s(x) = \exp\left(-\frac{\tau x^2}{2\xi_{\|}^2}\right),$$
$$\Delta_t(x) = i\frac{\sqrt{7\zeta(3)}}{\gamma}\left(\frac{g_t g_s}{g_t - g_s}\right)\sqrt{\tau}\left(\frac{H}{H_p}\right) \quad (13)$$
$$\times\left(\frac{\sqrt{\tau}x}{\sqrt{2}\xi_{\|}}\right)\exp\left(-\frac{\tau x^2}{2\xi_{\|}^2}\right).$$

Equations (12), (13) are the main results of our letter. They extend the GL equations [3, 1, 2] and the famous Abrikosov solution for a superconducting nucleus [19, 1, 2] to the case $g_t \neq 0$. Equations (12) and (13) directly demonstrate that the Abrikosov solution [19, 1, 2] is absolutely unstable in the absence of impurities; thus, a singlet order parameter is always mixed with a triplet one in the vortex phase for both attractive $-g_t < 0$ and repulsive $-g_t > 0$ interactions in a triplet (p-wave) channel. From Eqs. (12), (13), it also follows that the triplet component breaks not only the inversion symmetry but also the time reversal symmetry since $\Delta_t^*(x) \neq \Delta_t(x)$ due to the imaginary coefficient i.

We hope that our results (8)–(13) open a new area of research: theoretical and experimental studies of exotic vortex superconducting phases in singlet superconductors with their properties being even more unusual than that in so-called unconventional superconductors [10, 11]. We stress that the type-IV superconductivity phenomenon suggested in the letter is an inherent and very common property of singlet superconductivity. In fact, we have shown that each s-wave [14] pure type-II superconductor is actually a type-IV superconductor. A finite amount of impurities may result in the appearance of the forth critical field $H_{c4}(T)$, which may correspond to the phase transition (or crossover) between phase $H_{c1}(T) < H < H_{c4}(T)$, where broken symmetries of Cooper pairs do not exist (or marginally), and phase $H_{c4}(T) < H < H_{c2}(T)$, where broken inversion and time-reversal symmetries are essential (see Fig. 1). From Eqs. (13), it is directly seen that the symmetry breaking triplet component is of the order of unity at low temperatures in such modern strongly correlated superconductors as organic, high-T_c, MgB_2, and some others, where $|g_t| \sim |g_s|$ and $H_{c2}(0) \sim H_p$. In conclusion, we point out that spin splitting and broken translational symmetry effects have been studied in [20–23] in a different context.

I dedicate the results obtained in this work to my wife Natalia, whose enormous support has given him the courage to set and attack the type-IV superconductivity problem.

REFERENCES

1. A. A. Abrikosov, *Fundamentals of the Theory of Metals* (Nauka, Moscow, 1987; Elsevier, Amsterdam, 1988).
2. P. G. de Gennes, *Superconductivity of Metals and Alloys* (Westview Press, Boulder, 1999; Mir, Moscow, 1968).
3. L. P. Gorkov and T. K. Melik-Barkhudarov, Zh. Éksp. Teor. Fiz. **45**, 1493 (1963) [Sov. Phys. JETP **18**, 1031 (1964)].
4. D. Jerome, A. Mazaud, M. Ribault, and K. Bechgaard, J. Phys. Lett. **41**, L-95 (1980).
5. T. Ishiguro, K. Yamaji, and G. Saito, *Organic Superconductors*, 2nd ed. (Springer, Heidelberg, 1998).
6. F. Steglich, J. Aarts, C. D. Bredl, *et al.*, Phys. Rev. Lett. **43**, 1892 (1979).
7. J. G. Bednortz and K. Muller, Z. Phys. B **64**, 189 (1986).
8. Y. Maeno, H. Hashimoto, K. Yoshida, *et al.*, Nature **372**, 532 (1994).
9. J. Nagamatsu, N. Nakagawa, T. Muranaka, *et al.*, Nature **410**, 63 (2001).
10. M. Sigrist and K. Ueda, Rev. Mod. Phys. **63**, 239 (1991).
11. V. P. Mineev and K. V. Samokhin, *Introduction to Unconventional Superconductivity* (Gordon and Breach, Amsterdam, 1999).
12. We do not use term "type-III superconductivity" in order to distinguish between suggested in the letter novel bulk phenomenon and a so-called surface superconductivity, which is characterized by critical field $H_{c3}(T)$ [1, 2].
13. A. M. Clogston, Phys. Rev. Lett. **9**, 266 (1962); B. S. Chandrasekhar, Appl. Phys. Lett. **1**, 7 (1962).

14. Type-IV superconductivity phenomenon in layered *d*-wave superconductors is considered in A.G. Lebed, Phys. Rev. Lett. (submitted).

15. L. P. Gorkov, Zh. Éksp. Teor. Fiz. **34**, 735 (1958) [Sov. Phys. JETP **7**, 505 (1958)].

16. A. A. Abrikosov, L. P. Gorkov, and I. E. Dzyaloshinskiĭ, *Methods of Quantum Field Theory in Statistical Physics* (Fizmatgiz, Moscow, 1962; Prentice-Hall, Englewood Cliffs, N.J., 1963).

17. L. P. Gorkov, Zh. Éksp. Teor. Fiz. **37**, 833 (1959) [Sov. Phys. JETP **10**, 593 (1960)].

18. L. P. Gorkov, Zh. Éksp. Teor. Fiz. **36**, 1918 (1959) [Sov. Phys. JETP **9**, 1364 (1959)].

19. A. A. Abrikosov, Zh. Éksp. Teor. Fiz. **32**, 1442 (1957) [Sov. Phys. JETP **5**, 1174 (1957)].

20. M. M. Salomaa and G. E. Volovik, Rev. Mod. Phys. **59**, 533 (1987).

21. S. Matsuo, H. Shimahara, and K. Nagai, J. Phys. Soc. Jpn. **63**, 2499 (1994).

22. H. Shimahara, Phys. Rev. B **62**, 3524 (2000).

23. L. P. Gorkov and E. I. Rashba, Phys. Rev. Lett. **87**, 037004 (2001).

JETP Letters, Vol. 82, No. 4, 2005, pp. 210–214. Translated from Pis'ma v Zhurnal Éksperimental'noĭ i Teoreticheskoĭ Fiziki, Vol. 82, No. 4, 2005, pp. 228–233.

Parity and Abrupt Broadening of Resonance Levels in Triple-Barrier Structures

A. B. Pashkovskiĭ

Research and Production Enterprise "Istok," Fryasino, Moscow region, 141190 Russia

Received June 30, 2005

Expressions for resonance active high-frequency small-signal conductivity and resonance level widths have been derived for asymmetric triple-barrier resonance–tunneling structures with thin high barriers. It is found that if the levels forming a common resonance level have different parities in each of double-barrier structures, the width of the common level and, accordingly, the total conductance of the entire structure may increase manifold for a certain choice of the triple-barrier structure parameters. Consequently, the lifetime of electrons on this level also decreases drastically; hence, the conditions of coherent transport (departure of electrons from the structure without their collision with phonons) can be easily realized. © *2005 Pleiades Publishing, Inc.*

PACS numbers: 73.40.–c

INTRODUCTION

Semiconducting heterostructures with coherent (collisionless) electron transport have been actively studied in recent years [1–6]. The average time of electron departure from the active region in such structures, which usually has the form of one or several quantum wells, is much shorter than the characteristic time of any process disturbing the coherence of the electron wavefunction. After the development of the theoretical basis for a quantum cascade laser based on coherent electron transport for specific structures available at that time [2], analysis of intersubband electron transitions in such structures made it possible to predict a number of new physical effects and to outline ways for their application to effectively generate terahertz electromagnetic oscillations [3, 4]. One of the fundamental difficulties in designing lasers, as well as other devices based on coherent electron transport, is the high conductivity required for their operation; i.e., the active structures must have narrow resonance levels, on the one hand, and short electron lifetimes in the structure (which is necessary for collisionless departure of electrons from the structure and for conservation of the wavefunction phase) and, accordingly, broad resonance levels, on the other hand. To increase the high-frequency active conductivity and, hence, the intensity of the quantum transitions in a coherent quantum cascade laser, it was proposed [4] to use triple-barrier structures in which transitions occur in the first well (double-barrier structure), while one of the levels in the second well coincides, to a certain extent, with the lower level in the first well, thus forming a common (output) level of the triple-barrier structure (Fig. 1a). However, the effect of parity of the coinciding levels was not studied in that work, while this effect (as was found later) may lead to a very surprising result. As will be showed below, the coincidence of levels with different parities makes it possible to considerably increase the width of the common level without noticeably changing the conductance and, hence, the intensity of the quantum transitions in the structure. This possibility is of fundamental importance for operation of coherent quantum cascade lasers and other analogous devices, because it allows one to reduce the electron time of flight through the active region of the structure, thus, increasing the degree of coherence of the electron transport without a simultaneous decrease in the conductance (the intensity of quantum transitions).

RESULTS OF CALCULATIONS

Let us consider an asymmetric triple-barrier structure with thin (δ-shaped) barriers (see Fig. 1a) to which a uniform rf electric field varying as $E(t) = 2E\cos\omega t = E(e^{i\omega t} + e^{-i\omega t})$ is applied. For definiteness, we assume that a monochromatic electron beam with energy ε is incident from the left on the Kth resonance level of the first double-barrier structure. The rf field frequency corresponds to transitions to the Lth level of the same structure (see Fig. 1), and the Nth resonance level of the second double-barrier structure lies near the Lth level of the first structure, thus, forming a common resonance level of the entire structure. In this case, the time-dependent Schrödinger equation has the form

$$\begin{aligned} i\hbar\frac{\partial\psi}{\partial t} &= -\frac{\hbar^2}{2m^*}\frac{\partial^2\psi}{\partial x^2} + H(x)\psi + H(x,t)\psi, \\ H(x) &= U(\theta(x) - \theta(x-a)) \\ &+ U_1(\theta(x-a) - \theta(x-a-l)) + U_2\theta(x-a-l) \\ &+ \alpha\delta(x) + \alpha\rho\delta(x-a) + \alpha\gamma\delta(x-a-l), \end{aligned} \quad (1)$$

0021-3640/05/8204-0210$26.00

$$H(x,t) = -qE[x(\theta(x)-\theta(x-a-l)) + (a+l)\theta(x-a-l)](e^{i\omega t}+e^{-i\omega t}).$$

Here, q and m^* are the electron charge and mass, respectively; $\alpha = \varphi_b b$ is the intensity of the first barrier, where φ_b and b are its height and width, respectively; $\theta(x)$ is the unit step function; γ and ρ are the numerical coefficients; a and l are the distances between the barriers; and U, U_1, and U_2 are the jumps of the bottom of the conduction band at the barriers. In this case, the unperturbed wave function of an electron has the form

$$\psi_0(x) = \begin{cases} \exp(ik_0x) + D_0\exp(-ik_0x), & x<0 \\ A_0\sin(kx) + B_0\cos(kx), & 0<x<a \\ Z_0\sin(k_1(x-a)) + W_0\cos(k_1(x-a)), & a<x<a+l \\ C_0\exp(ik_2(x-a-l)), & x>a+l, \end{cases} \quad (2)$$

$$k_0 = (2m^*\varepsilon/\hbar^2)^{1/2}, \quad k = (2m^*(\varepsilon+U)/\hbar^2)^{1/2},$$
$$k_1 = (2m^*(\varepsilon+U_1)/\hbar^2)^{1/2}, \quad k_2 = (2m^*(\varepsilon+U_2)/\hbar^2)^{1/2}.$$

The effect described here is as simple as ridiculous and surprising at first glance. However, for transitions in a structure with an rf field, this effect is masked by a cumbersome (although basically elementary) expression. Consequently, it is reasonable to first solve the much simpler and clear problem of the passage of electrons through a common resonance level of a triple-barrier structure that is formed by the resonance levels in each double-barrier structure (quantum well; see Fig. 1b). The system of equations describing the passage of electrons through a triple-barrier structure (including the matching conditions for the wave function at the barriers [7]) has the matrix form

$$\begin{pmatrix} 1 & 0 & -1 & 0 & 0 & 0 \\ ik_0-y & k & 0 & 0 & 0 & 0 \\ 0 & \sin k\alpha & \cos ka & 0 & -1 & 0 \\ 0 & -k\cos ka & k\sin ka & k_1 & -\rho y & 0 \\ 0 & 0 & 0 & \sin k_1a & \cos k_1a & -1 \\ 0 & 0 & 0 & -k_1\cos k_1a & k_1\sin k_1a & ik_2-\gamma y \end{pmatrix} \begin{pmatrix} D_0 \\ A_0 \\ B_0 \\ Z_0 \\ W_0 \\ C_0 \end{pmatrix} = \begin{pmatrix} f_1 \\ f_2 \\ f_3 \\ f_4 \\ f_5 \\ f_6 \end{pmatrix} = \begin{pmatrix} -1 \\ ik_0+y \\ 0 \\ 0 \\ 0 \\ 0 \end{pmatrix}. \quad (3)$$

Here, $y = 2m^*\alpha/\hbar^2$ is the resonance parameter in structures with δ-shaped barriers. For intense barriers and, accordingly, narrow resonance levels, we have $y \gg k$.

We will seek the solution of the system using the Kramer method. To determine the transmittance of electrons through the structure, we calculate the coefficient C_0 of wave function (2) as $C_0 = \Delta C_0/\Delta$, where Δ is the determinant of system (3) and ΔC_0 is the determinant obtained from the determinant Δ by substituting the right-hand side of Eq. (3) for the last column. Elementary calculations show that

$$\Delta C_0 = 2ikk_0k_1 \quad (4)$$

is independent of the barrier thickness and is a monotonic, slowly increasing function of the electron energy. Consequently, the transmittance is maximal (resonant) when the determinant of system (3) is minimal.

Under the conditions

$$\cos ka \approx (-1)^L, \quad \cos k_1l \approx (-1)^N,$$
$$\sin ka \approx -\frac{\chi k}{y}, \quad \sin k_{1-}l \approx -\frac{\lambda k_1}{y}, \quad (5)$$
$$\lambda = (-1)^{L+N+1}\frac{(-1)^{L+1}(1+\gamma+\rho)+\chi(\gamma+\rho)}{\gamma(1+\rho+(-1)^{L+1}\chi\rho)},$$

the determinant of the system becomes imaginary and small in the resonance parameter (this is likely a common property of all systems with δ-shaped barriers):

$$\Delta_r = (-1)^{L+N+1} \times \frac{ikk_1(k_0\gamma^2 + k_2(1+\rho(-1)^{L+1}\chi\rho)^2)}{\gamma(1+\rho+(-1)^{L+1}\chi\rho)}. \quad (6)$$

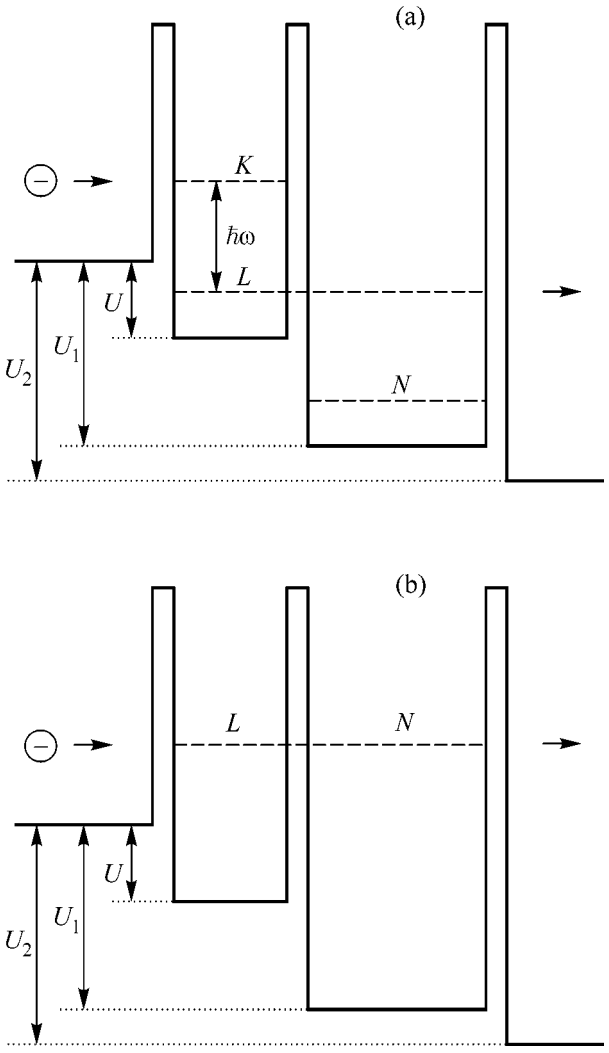

Fig. 1. Schematic band diagram of the triple-barrier structures under study: (a) triple-barrier structure with resonance transitions and (b) triple-barrier structure with through tunneling.

It is easily seen that, for small deviations of the electron energy from resonance (accordingly, the deviations of the wave vectors are δk and δk_1), the determinant becomes

$$\Delta = \Delta_r + \delta\Delta = \Delta_r - y^3\gamma\rho\delta k a\delta k_1 l - \frac{y^2\gamma((-1)^{L+N}k_1\delta k\_a \pm k\delta k_1 l(1+\rho+(-1)^{L+1}\chi\rho)^2)}{1+\rho+(-1)^{L+1}\chi\rho}. \quad (7)$$

The properties of the determinants ΔC_0 and Δ suggest a simple method for determining the resonance level width. The resonance level half-width $\Gamma/2$ (the distance from its center over which the square of the wave function in the structure is halved) is determined by the doubling condition for the squared modulus of the system determinant:

$$|\Delta|^2 = 2|\Delta_r|^2. \quad (8)$$

Since the resonance determinant is imaginary and its correction is real, we have

$$|\Delta_r| = |\delta\Delta|. \quad (9)$$

If the parities of levels in each quantum well are the same [the plus sign in Eq. (7)], the first term in the correction to the resonance determinant in Eq. (7) can be neglected if the two conditions $k/y \ll 1$ and $(k/y)^{1/2} \ll 1$ are satisfied simultaneously (the second condition is required to disregard the resonance level asymmetry). In this case, nothing peculiar happens and the resonance level width is determined as

$$\Gamma_L = \Gamma^l_{\rm sym}\frac{k_0\gamma^2 + k_2(1+\rho+(-1)^{L+1}\chi\rho)^2}{2\gamma^2 k\left(1+\frac{L^2l^3}{N^2a^3}(1+\rho+(-1)^{L+1}\chi\rho)^2\right)}. \quad (10)$$

Here, $\Gamma_{\rm sym}$ is the level width in a symmetric double-barrier structure with width a and δ-shaped barriers of intensity α and a level height Σ_L from the bottom of the conduction band:

$$\Gamma^L_{\rm sym} = \frac{8k^2\Sigma_a}{\pi L y^2}, \quad \Sigma_L = \frac{\pi^2\hbar^2L^2}{2m^*a^2}, \quad \Sigma_N = \frac{\pi^2\hbar^2N^2}{2m^*l^2}. \quad (11)$$

In other words, if the levels forming the common resonance level have the same parity, the level width in the triple-barrier structure has the same degree of smallness in the large resonance parameter y/k as the level width of the symmetric double-barrier structure.

It is immediately seen that the situation for the levels with different parities substantially differs from the case of the levels with the same parity. In this case, the terms with δk_a and $\delta k_1 l$ in the last term of formula (7) are separated by the minus rather than plus sign. Consequently, even when the two conditions $k\_/y \ll 1$ and $(k\_/y)^{1/2} \ll 1$ are satisfied simultaneously (exact resonance), the structure parameters can be chosen so that the entire correction

$$\chi = (-1)^L\frac{1+\rho\pm(Na/Ll)^{3/2}}{\rho}, \quad (12)$$

to the determinant is small as compared to the penultimate term and the resonance level width is determined as

$$\Gamma_L = \frac{\Gamma^L_{\rm sym}}{2}\left(\frac{a}{l}\right)^{3/4}\left(\frac{N}{L}\right)^{1/4} \times\left[\frac{k_0g^2 + k_2(Na/Ll)^3}{\gamma^2\rho k}\right]^{1/2}\left(\frac{y}{k}\right)^{1/2}. \quad (13)$$

Thus, when the parities of the levels forming the common level in the triple-barrier structure are different and condition (12) is valid, the width of the resonance level increases strongly (in proportion to the root of the large resonance parameter y/k) as compared to the case of identical parities of the levels.

It should be noted that the parameter χ for each resonance energy may assume two values (as in the case of the split level in a symmetric double-barrier structure); however, the resonance conditions imposed on the parameter λ virtually rule out the existence of two closely spaced broad levels (in fact, a single split broad level).

It is also interesting that, under the additional condition

$$k_0\gamma^2 = k_2(Na/Ll)^3, \tag{14}$$

the level becomes not only very broad but also completely transparent (with an accuracy of k/y) at the center.

Let us now consider the structure shown in Fig. 1a with an applied rf field. For intense barriers with $y \gg k$ (the system with resonance levels is meaningful only for such barriers), the coefficients of wave function (2) have the form

$$D_0 = 1, \quad B_0 = 2, \quad A_0 = \frac{2y}{k}, \quad W_0 = \frac{2(-1)^K}{\rho},$$
$$Z_0 = \frac{2\cot(k_1 l)}{\rho}, \quad C_0 = -\frac{2k_1}{\gamma\rho y \sin k_1 l}. \tag{15}$$

In the small signal approximation, the first-order correction ψ_1 to the wave function of the ground state exhibits the time dependence $\psi_1 = \psi_+(x)e^{-i(\omega_0+\omega)t} + \psi_-(x)e^{-i(\omega_0-\omega)t}$ [3] corresponding to the emission or absorption of a photon with energy $\hbar\omega$. In the particular case of a triple-barrier structure, we have

$$\psi_\pm(x) = \begin{cases} D_\pm \exp(-ik_{0\pm}x), & x < 0 \\ A_\pm \sin(kx) + B_\pm \cos(kx) + \varphi_\pm(x), & 0 < x < a \\ Z_\pm \sin(k_{1\pm}(x-a)) & \\ + W_\pm \cos(k_{1\pm}(x-a)) + \chi_\pm(x), & a < x < a+l \\ C_\pm \exp(ik_{2\pm}(x-a-l)) & \\ + P_\pm \exp(ik_2(x-a-l)), & x > a+l, \end{cases} \tag{16}$$

where

$$k = (2m^*(\hbar\omega - \varepsilon)/\hbar^2)^{1/2},$$
$$k_{i\pm} = (2m^*(\varepsilon + U_i \pm \hbar\omega)/\hbar^2)^{1/2},$$

and

$$P_\pm = \mp\frac{qEa}{\hbar\omega}\psi_0(a+l),$$
$$\varphi_\pm, \chi_\pm = \mp\frac{qEa}{\hbar\omega}\psi_0(x) + \frac{qE}{m^*\omega^2}\psi_0'(x)$$

are the corresponding particular solutions of the equations for $\psi_\pm$ (see [3, 4]). Let us consider the structure shown in Fig. 1a and the frequency corresponding to transitions to the lower resonance level. In this case, the correction ψ_+ to the wave function corresponding to photon absorption is small and the system of equations for determining the coefficients A_-, B_-, C_-, D_-, Z_-, and W_- has matrix form (3), with the change $k_0 \longrightarrow ik$ and $k_i \longrightarrow k_{i-}$ and the right-hand side in the form

$$f_1 = \varphi_-(0), \quad f_2 = -\varphi_-'(0),$$
$$f_3 = \chi_-(a) - \varphi_-(a),$$
$$f_4 = \rho y\chi_-(a) - \chi_-'(a) + \varphi_-'(a), \tag{17}$$
$$f_5 = P_- - \chi_-(a+l), \quad f_6 = (\gamma y - ik_2)P_- - \chi_-'(a+l).$$

Under the conditions

$$\cos k_- a \approx (-1)^L, \quad \cos k_{1-} l \approx (-1)^N,$$
$$\sin k_- a \approx -\frac{k_-}{y}\left(\beta + \frac{\Delta\beta}{y}\right),$$
$$\sin k_{1-} l \approx -\frac{k_{1-}}{y}\left(\xi + \frac{\Delta\xi}{y}\right), \tag{18}$$
$$\beta = \frac{1 + \rho + \gamma + \gamma\xi + (-1)^{L+1}\gamma\xi\rho}{\gamma + \rho + (-1)^{L+1}\gamma\xi\rho}(-1)^L,$$
$$\Delta\beta = (-1)^{L+1}\kappa - \frac{\gamma^2\Delta\xi}{(\gamma + \rho + (-1)^{L+1}\gamma\xi\rho)^2}$$

[these resonance conditions slightly differ from conditions (5), because the bottom of the conduction band lies higher than the resonance level on the left of the structure], the determinant becomes small in the large resonance parameter y:

$$\Delta_r = \frac{ik_-k_{1-}k_{2-}(-1)^{2L+N+1}}{\gamma + \rho + (-1)^{2L+N+1}\gamma\xi\rho}. \tag{19}$$

For small deviations of the electron energy from resonance (accordingly, for the deviations δk_- and δk_{1-} of the wave vectors), the determinant is given by

$$\Delta = \Delta_r + \delta\Delta = \Delta_r - y^3\gamma\rho\delta k_- a\delta k_{1-} l$$
$$-\frac{y^2(k_-\gamma^2\delta k_{1-} l + (-1)^{L+N}k_{1-}\delta k_- a(\gamma + \rho + (-1)^L\gamma\xi\rho)^2)}{\gamma + \rho + (-1)^L\gamma\xi\rho}. \tag{20}$$

For levels with the same parity, the penultimate term in the resultant expression can be neglected if $k_-/y \ll 1$ and $(k_-/y)^{1/2} \ll 1$. In this case, the width of the lower level in the triple-barrier structure can be calculated by the formula

$$\Gamma_L = \frac{\Gamma_{\text{sym}}^L}{2}\frac{k_{2-}}{k_-((Ll/Na)^3 + (\gamma + \rho + (-1)^L\gamma\zeta\rho)^2)}. \quad (21)$$

For the Lth and the Nth levels with different parities, the terms containing $\delta k_- a$ and $\delta k_- l$ in the last term of relation (20) are separated by the minus rather than plus sign as in the case considered above. Consequently, even if the conditions $k_-/y \ll 1$ and $(k_-/y)^{1/2} \ll 1$ are satisfied simultaneously (exact resonance), the structure parameters can be chosen so that the entire correction

$$\xi = (-1)^{L+1}\left(\frac{1}{\rho} \pm \frac{L}{\rho N}\sqrt{\frac{l^3}{a^3}} + \frac{1}{\gamma}\right), \quad (22)$$

to the determinant is small as compared to the penultimate term. In this case, the level width is determined as

$$\Gamma_L = \frac{\Gamma_{\text{sym}}^L}{2}\left(\frac{yk_{2-}}{\gamma\rho k_-^2}\right)^{1/2}\left(\frac{N}{L}\right)^{3/2}\left(\frac{a}{l}\right)^{9/4}. \quad (23)$$

Thus, in this case, the level width is also proportional to $(k_-/y)^2$ rather than to $(k_-/y)^{3/2}$; i.e., the resonance level is broadened manifold. Accordingly, the total conductance of the structure also increases. Naturally, the total conductance generally depends not only on the width of the lower level but also on the width of the upper level and on the electron distribution function in the vicinity of the middle of the level. However, in the simplest case, where the upper level is noticeably broader than the lower level and the electron distribution function $f(\varepsilon)$ varies insignificantly over energy intervals on the order of the upper level width, the total conductance increases in proportion to the width of the lower level and is given by the expression

$$\sigma_{\text{int}} = \frac{\pi\sigma f(\varepsilon)\Gamma_L}{2}. \quad (24)$$

Here,

$$\sigma = 8\sigma_{\text{sym}}\frac{\gamma^2 k_-}{k_{2-}}\left(\frac{L^2}{N^2}\frac{l^3}{a^3}\right) \quad (25)$$

is the monoenergetic conductivity of the structure and

$$\sigma_{\text{sym}} = -\frac{8q^2 m^*\alpha^4}{\pi L\hbar^6\omega^3}[1 - (-1)^{K-L}] \quad (26)$$

is the active resonance conductance of a symmetric double-barrier structure with a barrier intensity of α, in which electrons with unit concentration pass from the upper Kth level to the lower Lth level.

For the total conductivity, we finally obtain

$$\sigma_{\text{int}} = \frac{\pi\sigma f(\varepsilon)\Gamma_L}{2} = 4\sigma_{\text{sym}}\Gamma_{\text{sym}}^L\left(\frac{y}{\gamma\rho k_{2-}}\right)^{1/2}\left(\frac{L}{N}\right)^{1/2}\left(\frac{l}{a}\right)^{3/4}\frac{\pi f(\varepsilon)}{2}. \quad (27)$$

It is seen that the total conductivity may sharply increase in this case as compared to the case of the common level formed by the levels of the same parity.

CONCLUSIONS

It has been found that if the parities of the levels forming a common resonance level in an asymmetric triple-barrier structure are different in each well, even in the case of an absolutely transparent structure, the width of the common level may be much larger than the width of the level formed by the levels of the same parity. For resonance transition of electrons in the asymmetric triple-barrier structure, which are induced by a weak rf field; for different parities of the levels forming the common lower resonance level; and for a certain choice of the structure parameters, the width of the common level and, accordingly, the total conductivity of the entire structure may increase manifold. Accordingly, the lifetime of electrons on such a level decreases noticeably and, hence, the conditions of electron departure from the structure without collisions with phonons can be easily realized. In addition, under certain conditions, this may lead to a sharp increase in the total conductivity of the structure. Thus, such structures may become very promising for both the creation of quantum cascade lasers with ballistic electron transport and the development of other devices with coherent electron transport.

This study was supported by the Russian Foundation for Basic Research (project no. 04-02-17177).

REFERENCES

1. S. Blaser, M. Rochat, M. Beck, and J. Faist, Phys. Rev. B **61**, 8369 (2000).
2. E. I. Golant, A. B. Pashkovskiĭ, and A. S. Tager, Pis'ma Zh. Tekh. Fiz. **20** (21), 74 (1994) [Tech. Phys. Lett. **20**, 886 (1994)].
3. E. I. Golant and A. B. Pashkovskiĭ, Pis'ma Zh. Éksp. Teor. Fiz. **63**, 559 (1996) [JETP Lett. **63**, 590 (1996)].
4. E. I. Golant and A. B. Pashkovskiĭ, Pis'ma Zh. Éksp. Teor. Fiz. **67**, 372 (1998) [JETP Lett. **67**, 394 (1998)].
5. D. V. Pozdnyakov, V. M. Borzdov, and F. F. Komarov, Fiz. Tekh. Poluprovodn. (St. Petersburg) **38**, 1097 (2004) [Semiconductors **38**, 1061 (2004)].
6. C. Gmachl, F. Capasso, D. L. Sivco, and A. Y. Cho, Rep. Prog. Phys. **64**, 1533 (2001).
7. V. M. Galitskiĭ, B. M. Karnakov, and V. I. Kogan, *Problems in Quantum Mechanics* (Nauka, Moscow, 1992) [in Russian].

Translated by N. Wadhwa

JETP Letters, Vol. 82, No. 4, 2005, pp. 215–219. From Pis'ma v Zhurnal Éksperimental'noĭ i Teoreticheskoĭ Fiziki, Vol. 82, No. 4, 2005, pp. 234–238.

Hall Coefficient in Heavy Fermion Metals¶

V. R. Shaginyan*, [a], K. G. Popov[b], and S. A. Artamonov[a]

[a] *Petersburg Nuclear Physics Institute, Russian Academy of Sciences, Gatchina, 188300 Russia*
** e-mail: vrshag@thd.pnpi.spb.ru*
[b] *Komi Science Center, Ural Division, Russian Academy of Sciences, Syktyvkar, 167982 Russia*

Received June 30, 2005

Experimental studies of the antiferromagnetic (AF) heavy fermion metal $YbRh_2Si_2$ in a magnetic field B indicate the presence of a jump in the Hall coefficient at a magnetic-field tuned quantum state in the zero temperature limit. This quantum state occurs at $B \geq B_{c0}$ and induces the jump even though the change of the magnetic field at $B = B_{c0}$ is infinitesimal. We investigated this by using the model of heavy electron liquid with the fermion condensate. Within this model, the jump takes place when the magnetic field reaches the critical value B_{c0} at which the ordering temperature $T_N(B = B_{c0})$ of the AF transition vanishes. We show that at $B \longrightarrow B_{c0}$, this second order AF phase transition becomes the first order one, making the corresponding quantum and thermal critical fluctuations vanish at the jump. At $T \longrightarrow 0$ and $B = B_{c0}$ the Grüneisen ratio as a function of the temperature T diverges. We demonstrate that both the divergence and the jump are determined by the specific low temperature behavior of the entropy $S(T) \propto S_0 + a\sqrt{T} + bT$ with S_0; a and b are temperature independent constants.

PACS numbers: 71.10.Hf, 71.27.+a, 74.72.–h

The most outstanding puzzle of heavy fermion (HF) metals is what determines their universal behavior, which drastically differs from the behavior of ordinary metals. It is widely accepted that the fundamental physics observed in the HF metals is controlled by quantum phase transitions. A quantum phase transition is driven by control parameters such as composition, pressure, number density x of electrons (holes), magnetic field B, etc., and takes place at a quantum critical point (QCP) when the temperature $T = 0$. In the case of conventional quantum phase transitions (CQPT), the physics is dominated by thermal and quantum fluctuations near the CQP. This critical state is characterized by the absence of quasiparticles. It is believed that the absence of quasiparticle-like excitations is the main cause of the non-Fermi liquid (NFL) behavior, see, e.g., [1]. However, theories based on CQPT fail to explain the experimental observations of the universal behavior related to the divergence of the effective mass M^* at the magnetic field tuned QCP, the specific behavior of the spin susceptibility, its scaling properties, etc.

It is possible to explain the observed universal behavior of the HF metals on the basis of the fermion condensation quantum phase transition (FCQPT) which takes place at $x = x_{FC}$ and allows the existence of the Landau quasiparticles down to the lowest temperatures [2]. It is the quasiparticles that define the universal behavior of the HF metals at low temperatures [2, 3]. In contrast to the conventional Landau quasiparticles, these are characterized by an effective mass that strongly depends on the temperature T, applied magnetic field B, and the number density x of the heavy electron liquid of the HF metal. Thus, we come back again to the key role of the effective mass.

On the other hand, it is plausible to probe the other properties of the heavy electron liquid that are not directly determined by the effective mass. Behind the point of FCPT, when $x < x_{FC}$, the heavy electron liquid possesses unique features directly determined by its quasiparticle distribution function $n_0(\mathbf{p})$ formed by the presence of the fermion condensate (FC) [4]. Therefore, the function $n_0(\mathbf{p})$ drastically differs from the quasiparticle distribution function of a typical Landau Fermi liquid (LFL) [5]. For example, it was predicted that, at low temperatures, the tunneling differential conductivity between an HF metal with FC and a simple metallic point can be noticeably dissymmetrical with respect to the change of the voltage bias [6]. As we shall see below, the magnetic field dependence of the Hall coefficient $R_H(B)$ can also provide information about electronic systems with FC.

Recent experiments have shown that the Hall coefficient in the antiferromagnetic (AF) HF metal $YbRh_2Si_2$ in a magnetic field B undergoes a jump in the zero temperature limit upon magnetic-field tuning of the metal from the AF to a paramagnetic state [7]. At some critical value B_{c0}, the magnetic field B induces the jump even though the change of the magnetic field at the critical value B_{c0} is infinitesimal.

¶ The text was submitted by the authors in English.

In this letter, we show that the abrupt change in the Hall coefficient is determined by the presence of FC and investigate this jump by using the model of the heavy electron liquid with FC, which is represented by a uniform electron liquid near FCQPT. Within this model, the jump takes place when the magnetic field reaches the critical value B_{c0} at which the Néel temperature $T_N(B = B_{c0})$ of the AF transition vanishes. At some temperature $T_{\rm crit}$ when $B \longrightarrow B_{c0}$, this second order AF phase transition becomes the first order one, making the corresponding quantum and thermal critical fluctuations vanish at the point where $T_N(B = B_{c0}) \longrightarrow 0$. At $T \longrightarrow 0$ and $B = B_{c0}$, the Grüneisen ratio $\Gamma(T) = \alpha(T)/C(T)$ as a function of the temperature T diverges. Here, $\alpha(T)$ is the thermal expansion coefficient and $C(T)$ is the specific heat. We show that both the divergence and the jump are determined by the specific low temperature behavior of the entropy $S(T) \simeq S_0 + a\sqrt{T/T_f} + bT/T_f$ with S_0, a, and b being temperature independent constants and T_f being the temperature at which the influence of FC vanishes.

To study the universal behavior of the HF metals at low temperatures, we use the heavy electron liquid model in order to get rid of the specific peculiarities of an HF metal. It is possible since we consider processes related to the low-power divergences of the corresponding physical quantities. These divergences are determined by small momenta transferred as compared to the momenta of the order of the reciprocal lattice; therefore, the contribution coming from the lattice can be ignored. On the other hand, we can simply use the common concept of the applicability of the LFL theory when describing electronic properties of metals [5]. Thus, we may safely ignore the complications due to the anisotropy of the lattice regarding the medium as a homogeneous heavy electron isotropic liquid.

At first, we briefly describe the heavy electron liquid with FC. Dealing with FCQPT, we have to put $T = 0$. In that case, the ground state energy $E_{\rm gs}$ of a system in the superconducting state is given by the BSC theory formula

$$E_{\rm gs}[\kappa(\mathbf{p})] = E[n(\mathbf{p})] + E_{\rm sc}[\kappa(\mathbf{p})], \quad (1)$$

where the occupation numbers $n(\mathbf{p})$ are connected to the factors $v(\mathbf{p})$, $u(\mathbf{p})$, and the order parameter $\kappa(\mathbf{p})$,

$$n(\mathbf{p}) = v^2(\mathbf{p}); \quad v^2(\mathbf{p}) + u^2(\mathbf{p}) = 1;$$
$$\kappa(\mathbf{p}) = v(\mathbf{p})u(\mathbf{p}) = \sqrt{n(\mathbf{p})(1-n(\mathbf{p}))}. \quad (2)$$

The second term $E_{\rm sc}[\kappa_p]$ on the right hand side of Eq. (1) is defined by the superconducting contribution that, in the simplest case of the weak coupling regime, is of the form

$$E_{\rm sc}[\kappa_p] = \lambda\int V_{pp}(\mathbf{p}_1, \mathbf{p}_2)\kappa(\mathbf{p}_1)\kappa^*(\mathbf{p}_2)\frac{d\mathbf{p}_1 d\mathbf{p}_2}{(2\pi)^4}, \quad (3)$$

where $\lambda V_{pp}(\mathbf{p}, \mathbf{p}_1)$ is the pairing interaction. Varying $E_{\rm gs}$ given by Eq. (1) with respect to $v(\mathbf{p})$, one finds

$$\varepsilon(\mathbf{p}) - \mu = \Delta(\mathbf{p})\frac{1-2v^2(\mathbf{p})}{2\kappa(\mathbf{p})}. \quad (4)$$

Here $\varepsilon(\mathbf{p})$ is defined by the Landau equation $\delta E[n(\mathbf{p})]/\delta n(\mathbf{p}) = \varepsilon(\mathbf{p})$, μ is the chemical potential, and the gap is

$$\Delta(\mathbf{p}) = -\lambda\int V_{pp}(\mathbf{p}, \mathbf{p}_1)\sqrt{n(\mathbf{p}_1)(1-n(\mathbf{p}_1))}\frac{d\mathbf{p}_1}{4\pi^2}. \quad (5)$$

If $\lambda \longrightarrow 0$, then $\Delta(\mathbf{p}) \longrightarrow 0$, and Eq. (4) reduces to the equation

$$\frac{\delta E[n(\mathbf{p})]}{\delta n(\mathbf{p})} - \mu = \varepsilon(\mathbf{p}) - \mu = 0, \text{ if } \kappa(\mathbf{p}) \neq 0. \quad (6)$$

As a result, at $x < x_{\rm FC}$, the function $n(\mathbf{p})$ is determined by the standard equation to search the minimum of the functional $E[n(\mathbf{p})]$ [8, 9]. Equation (6) determines the quasiparticle distribution function $n_0(\mathbf{p})$ that delivers the minimum value to the ground state energy E. The function $n_0(\mathbf{p})$, being the signature of the new state of the quantum liquids [10], does not coincide with the step function in the region $(p_f - p_i)$, where $\kappa(\mathbf{p}) \neq 0$, so that $0 < n_0(\mathbf{p}) < 1$ and $p_i < p_F < p_f$, with $p_F = (3\pi^2 x)^{1/3}$ being the Fermi momentum. We note the remarkable peculiarity of the FCQPT at $T = 0$: this transition is related to spontaneous breaking of gauge symmetry, when the superconducting order parameter $\kappa(\mathbf{p}) = \sqrt{n_0(\mathbf{p})(1-n_0(\mathbf{p}))}$ has a nonzero value over the region occupied by the fermion condensate, with the entropy $S = 0$ [2, 9], while the gap $\Delta(\mathbf{p})$ vanishes provided that $\lambda \longrightarrow 0$ [8, 9]. Thus, the state with FC cannot exist at any finite temperatures and is driven by the parameter x: at $x > x_{\rm FC}$, the system is on the disordered side of FCQPT; at $x = x_{\rm FC}$, Eq. (6) possesses the nontrivial solutions $n_0(\mathbf{p})$ with $p_i = p_F = p_f$; and, at $x < x_{\rm FC}$, the system is on the ordered side [2].

At finite temperatures $0 < T \ll T_f$, the function $n_0(\mathbf{p})$ determines the entropy $S_{\rm NFL}(T)$ of the heavy electron liquid in its NFL state

$$S_{\rm NFL}[n(p)] = -2\int[n(\mathbf{p}, T)\ln n(\mathbf{p}, T) + (1-n(\mathbf{p}, T)) \times \ln(1-n(\mathbf{p}, T))]\frac{d\mathbf{p}}{(2\pi)^3}, \quad (7)$$

with T_f being the temperature at which the influence of FC vanishes [8, 9]. Inserting into Eq. (7) the function $n_0(\mathbf{p})$, one can check that, behind the point of FCQPT, there is a temperature independent contribution $S_0(r) \propto (p_f - p_F) \propto |r|$, where $r = x_{\rm FC} - x$. Another specific contribution is related to the spectrum $\varepsilon(\mathbf{p})$ that insures the connection between the dispersionless region $(p_f - p_i)$ occupied by FC and the normal quasiparticles located at $p < p_i$ and at $p > p_f$, and, therefore, it is of the form

$\varepsilon(\mathbf{p}) \sim (p - p_f)^2 \sim (p_i - p)^2$. Such a form of the spectrum can be verified in exactly solvable models for systems with FC and leads to the contribution of this spectrum to the specific heat $C \sim \sqrt{T/T_f}$ [4]. Thus, at $0 < T \ll T_f$, the entropy can be approximated as

$$S_{\mathrm{NFL}}(T) \simeq S_0(r) + a\sqrt{\frac{T}{T_f}} + b\frac{T}{T_f}, \qquad (8)$$

with a and b being constants. The third term on the right hand side of Eq. (8) comes from the contribution of the temperature independent part of the spectrum $\varepsilon(\mathbf{p})$ and gives a relatively small contribution to the entropy.

The temperature independent term $S_0(r)$ determines the specific NFL behavior of the system. For example, the thermal expansion coefficient $\alpha(T) \propto x\partial(S/x)/\partial x$ determined mainly by the contribution coming from $S_0(r)$ becomes constant at $T \longrightarrow 0$ [11], while the specific heat $C = T\partial S(T)/\partial T \simeq (a/2)\sqrt{T/T_f}$. As a result, the Grüneisen ratio $\Gamma(T)$ diverges as $\Gamma(T) = \alpha(T)/C(T) \propto \sqrt{T_f/T}$.

We see that, at $0 < T \ll T_f$, the heavy electron liquid behaves as if it were placed at QCP; in fact, it is placed at the quantum critical line $x < x_{\mathrm{FC}}$; that is, the critical behavior is observed at $T \longrightarrow 0$ for all $x \le x_{\mathrm{FC}}$. At $T \longrightarrow 0$, the heavy electron liquid undergoes a first-order quantum phase transition because the entropy is not a continuous function: at finite temperatures, the entropy is given by Eq. (8), while $S(T = 0) = 0$. Therefore, the entropy undergoes a sudden jump $\delta S = S_0(r)$ in the zero temperature limit. We reach the conclusion that, due to the first order phase transition, the critical fluctuations are suppressed at the quantum critical line and the corresponding divergences, for example, the divergence of $\Gamma(T)$, are determined by the quasiparticles rather than by the critical fluctuations as one could expect in the case of CQPT, see, e.g., [1]. Note that, according to the well known inequality $\delta Q \le T\delta S$, the heat δQ of the transition from the ordered phase to the disordered one is equal to zero, because $\delta Q \le S_0(r)T \longrightarrow 0$ at $T \longrightarrow 0$.

To study the nature of the abrupt change in the Hall coefficient, we consider the case when the LFL behavior arises by the suppression of the AF phase upon applying a magnetic field B, for example, as takes place in the HF metals $YbRh_2Si_2$ and $YbRh_2(Si_{0.95}Ge_{0.05})_2$ [12, 13]. The AF phase is represented by the heavy electron LFL with the entropy vanishing as $T \longrightarrow 0$. For magnetic fields exceeding the critical value B_{c0} at which the Néel temperature is $T_N(B \longrightarrow B_{c0}) \longrightarrow 0$, the weakly ordered AF phase transforms into weakly polarized heavy electron LFL. At $T = 0$, the application of the magnetic field B splits the FC state occupying the region $(p_f - p_i)$ into the Landau levels and suppresses the superconducting order parameter $\kappa(\mathbf{p})$ destroying the FC state. Such a state is given by the multiconnected Fermi sphere, where the smooth quasiparticle distribution function $n_0(\mathbf{p})$ in the $(p_F - p_i)$ range is replaced by a multiconnected distribution. Therefore, the LFL behavior is restored, being represented by the weakly polarized heavy electron LFL and characterized by quasiparticles with the effective mass $M^*(B)$ [2, 14]

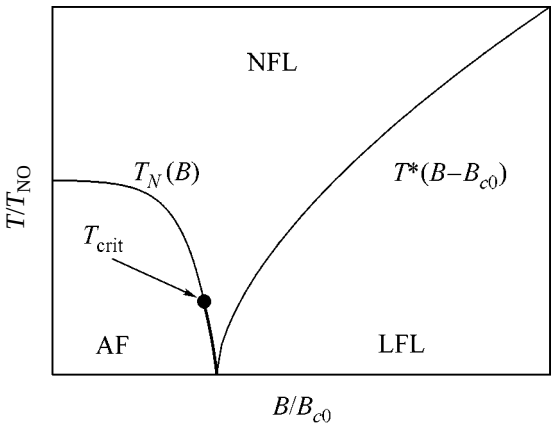

Fig. 1. T–B phase diagram of the heavy electron liquid. The $T_N(B)$ curve represents the field dependence of the Néel temperature. The line separating the AF and the NFL states is a guide for the eye. The black dot at $T = T_{\mathrm{crit}}$ shown by the arrow is the critical temperature at which the second order AF phase transition becomes the first one. At $T < T_{\mathrm{crit}}$, the thick solid line represents the field dependence of the Néel temperature when the AF phase transition is of the first order. The NFL state is characterized by the entropy S_{NFL} given by Eq. (8). The line separating the NFL state and the weakly polarized heavy electron LFL is $T^*(B - B_{c0}) \propto \sqrt{B - B_{c0}}$.

$$M^*(B) \propto \frac{1}{\sqrt{B - B_{c0}}}. \qquad (9)$$

At elevated temperatures $T > T^*(B - B_{c0}) \propto \sqrt{B - B_{c0}}$, the NFL state is restored and the entropy of the heavy electron liquid is given by Eq. (8). This behavior is displayed in the T–B phase diagram shown in Fig. 1.

In accordance with the experimental facts, we assume that, at relatively high temperatures $T/T_{\mathrm{NO}} \sim 1$, the AF phase transition is of the second order [12]. When T_{NO} is the Néel temperature in the absence of the magnetic field, the entropy and the other thermodynamic functions are continuous functions at the transition temperature $T_N(B)$. This means that the entropy of the AF phase $S_{\mathrm{AF}}(T)$ coincides with the entropy of the NFL state given by Eq. (8),

$$S_{\mathrm{AF}}(T \longrightarrow T_N(B)) = S_{\mathrm{NFL}}(T \longrightarrow T_N(B)). \qquad (10)$$

Since the AF phase demonstrates the LFL behavior, that is, $S_{\mathrm{AF}}(T \longrightarrow 0) \longrightarrow 0$, Eq. (10) cannot be satisfied at sufficiently low temperatures $T \le T_{\mathrm{crit}}$ due to the temperature-independent term $S_0(r)$, see Eq. (8). Thus, the second order AF phase transition becomes the first

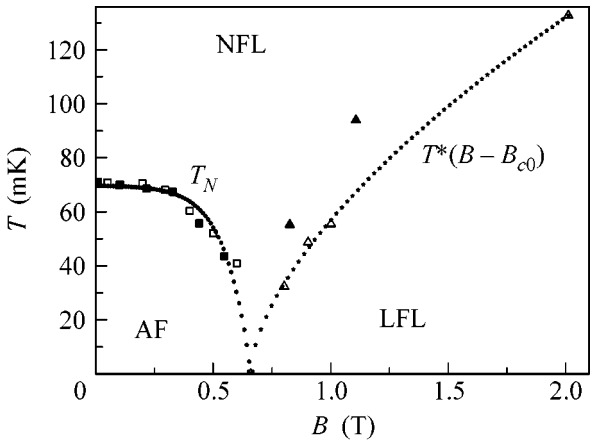

Fig. 2. T–B-phase diagram for $YbRh_2Si_2$. The T_N curve represents the field dependence of the Néel temperature. The line separating the AF and the NFL state is a guide for the eye. The NFL state is characterized by the entropy S_{NFL} given by Eq. (8). The line separating the NFL state and the LFL is $T^*(B - B_{c0}) = c\sqrt{B - B_{c0}}$, with c being an adjustable factor.

order one at $T = T_{crit}$ as is shown in Fig. 1. At $T = 0$, the critical field B_{c0} at which the AF phase becomes the heavy LFL is determined by the condition that the ground state energy of the AF phase coincides with the ground state energy $E[n_0(\mathbf{p})]$ of the heavy LFL; that is, the ground state of the AF phase becomes degenerated at $B = B_{c0}$. Therefore, the Néel temperature $T_N(B \longrightarrow B_{c0}) \longrightarrow 0$, and the behavior of the effective mass $M^*(B \geq B_{c0})$ is given by Eq. (9); that is, $M^*(B)$ diverges when $B \longrightarrow B_{c0}$. We note that the corresponding quantum and thermal critical fluctuations vanish at $T < T_{crit}$ because we are dealing with the first order AF phase transition. We can also safely conclude that the critical behavior observed at $T \longrightarrow 0$ and $B \longrightarrow B_{c0}$ is determined by the corresponding quasiparticles rather than by the critical fluctuations accompanying second order phase transitions. When $r \longrightarrow 0$, the heavy electron liquid approaches FCQPT from the ordered phase. Obviously, $T_{crit} \longrightarrow 0$ at the point $r = 0$, and we are led to the conclusion that the Néel temperature vanishes at the point when the AF second order phase transition becomes the first order one. As a result, one can expect that the contributions coming from the corresponding critical fluctuations can only lead to the logarithmic corrections to the Landau theory of the phase transitions [15], and the low-power critical behavior is again defined by the corresponding quasiparticles.

Now, we are in a position to consider the recently observed jump in the Hall coefficient at $B \longrightarrow B_{c0}$ in the zero temperature limit [7]. At $T = 0$, the application of the critical magnetic field B_{c0} suppressing the AF phase (with the Fermi momentum $p_{AF} \simeq p_F$) restores the LFL with the Fermi momentum $p_f > p_F$. At $B < B_{c0}$, the ground state energy of the AF phase is lower than that of the heavy LFL, while, at $B > B_{c0}$, we are dealing with the opposite case, and the heavy LFL wins the competition. At $B = B_{c0}$, both AF and LFL have the same ground state energy being degenerated. Thus, at $T = 0$ and $B = B_{c0}$, the infinitesimal change in the magnetic field B leads to a finite jump in the Fermi momentum. In response, the Hall coefficient $R_H(B) \propto 1/x$ undergoes a corresponding sudden jump. Here, we have assumed that the low temperature $R_H(B)$ can be considered as a measure of the Fermi volume and, therefore, as a measure of the Fermi momentum [7]. As a result, we obtain

$$\frac{R_H(B = B_{c0} - \delta)}{R_H(B = B_{c0} + \delta)} \simeq 1 + 3\frac{p_f - p_F}{p_F} \simeq 1 + d\frac{S_0(r)}{x_{FC}}. \quad (11)$$

Here, δ is an infinitesimal magnetic field; $S_0(r)/x_{FC}$ is the entropy per one heavy electron; and d is a constant, where $d \sim 5$. It follows from Eq. (11) that the abrupt change in the Hall coefficient tends to zero when $r \longrightarrow 0$ and vanishes when the system in question is on the disordered side of FCQPT.

As an application of the above consideration, we studied the T–B phase diagram for the HF metal $YbRh_2Si_2$ [12] shown in Fig. 2. The LFL behavior is characterized by the effective mass $M^*(B)$, which diverges as $1/\sqrt{B - B_{c0}}$ [12]. We can conclude that Eq. (9) gives a good description of this experimental fact, and $M^*(B)$ diverges at the point $B \longrightarrow B_{c0}$ with $T_N(B = B_{c0}) = 0$. It is seen from Fig. 2 that the line separating the LFL state and NFL can be approximated by the function $c\sqrt{B - B_{c0}}$ with c being a parameter. Taking into account that the behavior of $YbRh_2Si_2$ strongly resembles the behavior of $YbRh_2(Si_{0.95}Ge_{0.05})_2$ [13, 16, 17], we can conclude that, in the NFL state, the thermal expansion coefficient $\alpha(T)$ does not depend on T and the Grüneisen ratio as a function of the temperature T diverges [13]. We are led to the conclusion that the entropy of the NFL state is given by Eq. (8). Taking into account that, at relatively high temperatures, the AF phase transition is of the second order [12], we predict that at lower temperatures this becomes the first order phase transition. Then, the described behavior of the Hall coefficient $R_H(B)$ is in good agreement with the experimental facts [7].

In summary, we have shown that the T–B phase diagram of the heavy electron liquid with FC is in good agreement with the experimental T–B phase diagram obtained in measurements on the HF metals $YbRh_2Si_2$ and $YbRh_2(Si_{0.95}Ge_{0.05})_2$. We have also demonstrated that the abrupt jump in the Hall coefficient $R_H(B)$ is determined by the presence of FC. We observed that, at decreasing temperatures $T \leq T_{crit}$, the second order AF phase transition becomes the first order one, thus, making the corresponding quantum and thermal critical

fluctuations vanish at the jump. Therefore, the abrupt jump and the divergence of the effective mass taking place at $T_N \longrightarrow 0$ are defined by the behavior of quasiparticles rather than by the corresponding thermal and quantum critical fluctuations.

This work was supported by the Russian Foundation for Basic Research, project no. 05-02-16085.

REFERENCES

1. M. Vojta, Rep. Prog. Phys. **66**, 2069 (2003).
2. V. R. Shaginyan, JETP Lett. **79**, 286 (2004); V. R. Shaginyan, A. Z. Msezane, and M. Ya. Amusia, Phys. Lett. A **338**, 393 (2005).
3. J. W. Clark, V. A. Khodel, and M. V. Zverev, Phys. Rev. B **71**, 012 401 (2005).
4. V. A. Khodel and V. R. Shaginyan, JETP Lett. **51**, 553 (1990); V. A. Khodel, V. R. Shaginyan, and V. V. Khodel, Phys. Rep. **249**, 1 (1994).
5. E. M. Lifshitz and L. P. Pitaevskiĭ, *Statistical Physics* (Fizmatlit, Moscow, 2000; Butterworth, Oxford, 1999), Part 2.
6. V. R. Shaginyan, JETP Lett. **81**, 222 (2005).
7. S. Paschen *et al.*, Nature **432**, 881 (2004).
8. J. Dukelsky, V. A. Khodel, P. Schuck, and V. R. Shaginyan, Z. Phys. **102**, 245 (1997); V. A. Khodel and V. R. Shaginyan, Condens. Matter Theor. **12**, 222 (1997).
9. V. R. Shaginyan, Phys. Lett. A **249**, 237 (1998); M. Ya. Amusia and V. R. Shaginyan, Phys. Rev. B **63**, 224507 (2001).
10. G. E. Volovik, JETP Lett. **53**, 222 (1991).
11. M. V. Zverev, V. A. Khodel, V. R. Shaginyan, and M. Baldo, JETP Lett. **65**, 863 (1997).
12. P. Gegenwart *et al.*, Phys. Rev. Lett. **89**, 056402 (2002).
13. R. Küchler *et al.*, Phys. Rev. Lett. **91**, 066405 (2003).
14. Yu. G. Pogorelov and V. R. Shaginyan, JETP Lett. **76**, 532 (2002).
15. E. M. Lifshitz and L. P. Pitaevskiĭ, *Course of Theoretical Physics*, Vol. 5: *Statistical Physics* (Nauka, Moscow, 1978; Pergamon, New York, 1980).
16. J. Custers *et al.*, Nature **424**, 524 (2003).
17. P. Gegenwart *et al.*, Phys. Rev. Lett. **94**, 076402 (2005).

JETP Letters, Vol. 82, No. 4, 2005, pp. 220–223. Translated from Pis'ma v Zhurnal Éksperimental'noĭ i Teoreticheskoĭ Fiziki, Vol. 82, No. 4, 2005, pp. 239–242.

New Half-Metallic Ferromagnets: Double Perovskites $Sr(FeM)O_3$ (M = Sn, Ti, Zr)

I. R. Shein, V. L. Kozhevnikov, and A. L. Ivanovskiĭ

Institute of Solid State Chemistry, Ural Division, Russian Academy of Sciences, Yekaterinburg, 620219 Russia

e-mail: shein@ihim.uran.ru

Received July 5, 2005

In calculations using the local spin density approximation, a new group of half-metallic ferromagnets is predicted. This group comprises double perovskites Sr_2FeSnO_6, Sr_2FeTiO_6, and Sr_2FeZrO_6—systems with one type of magnetic ions that can be obtained by diluting the magnetic sublattice of $SrFeO_3$ with ions of nonmagnetic p^n and d^0 metals. © *2005 Pleiades Publishing, Inc.*

PACS numbers: 71.15.Mb, 71.20.–b, 72.80.Ga

Half-metallic magnets (HMMs) are defined [1, 2] as strong magnets whose spectrum exhibits metallic behavior for one spin subsystem (the carrier density at the Fermi level $N\uparrow(E_F) > 0$ but contains an energy gap for the opposite spin projection ($N\downarrow(E_F) = 0$). With the 100% spin polarization of electronic states near the Fermi level, HMMs exhibit nontrivial spin-dependent properties promising for spin electronics [3]. Heusler alloys and a number of chalcogenides and pnictides are widely known HMMs, see the reviews [2, 4].

Much attention in searching for HMMs is attracted by perovskite-like oxides, whose electrophysical and magnetic properties are determined by nonstandard combinations of spin, charge, and orbital ordering effects.

Half-metallic magnets have not been found among the simplest cubic perovskites of the ideal composition AMO_3 (where A is a rare- or alkaline-earth metal and M is a transition *d* metal). The HMM and pseudo-HMM behavior of perovskite-like systems can be achieved by controlling the type of carriers and the width of the M *d* band via hole or electron doping of the initial AMO_3 perovskite. At present, this is achieved by two methods.

1. Doping the nonmagnetic sublattice A with nonmagnetic ions. The perovskite $La_{2/3}Ca_{1/3}MnO_3$ [4], which has attracted particular attention in connection with the discussion of the nature of the colossal magnetoresistance effect in manganites, is the best known example of such HMM systems.

2. Doping the magnetic sublattice M with magnetic ions. This method turned out to be efficient in searching for half-metallic antiferromagnets and ferrimagnets. All the proposed materials (so-called double perovskites $A_2MM'O_6$, for example, Sr_2FeMoO_6, Sr_2FeReO_6, Sr_2CrWO_6, etc. [4, 5]) involve combinations of two different magnetic ions. As a rule, a 3*d* transition-metal ion and a 3*d*–5*d* transition-metal ion with open d^n shells ($1 \le n \le 9$) serve as one of them and as the second, respectively. The mechanism of the formation of the half-metallic state in these magnets is rather complex and is determined by the combination of superexchange interactions in M–O–M' chains and the competition of pd_σ, pd_π hybridization effects of M–M' pairs with oxygen. Recently, the possibility of double doping for obtaining half-metallic antiferromagnets $LaAVRuO_6$ (A = Ca, Sr, Ba) has been considered in [6].

In this work, the possibility of obtaining HMM materials by *doping the magnetic sublattice M with nonmagnetic ions* is considered. A new group of perovskite-like *half-metallic ferromagnets* (HMFMs) Sr_2FeSnO_6, Sr_2FeTiO_6, Sr_2FeZrO_6 is predicted theoretically as systems with one type of magnetic ions that can be obtained by diluting the magnetic sublattice of $SrFeO_3$ with nonmagnetic p^n and d^0 metal ions.

The base for our search was the suggestion that the half-metallic behavior of materials of the A_2MBO_6 type (where M is a magnetic d^n metal and B is a nonmagnetic p^n or d^0 metal) can be achieved by combining the properties of the magnet AMO_3 and the nonmagnetic semiconductor ABO_3. In other words, it was expected that the B ions in the double perovskites A_2MBO_6 will favor the creation of an energy gap in the spectrum and the adjustment of $Md^n\uparrow\downarrow$ orbitals can cause the fulfillment of the wanted condition $N\uparrow(E_F) > 0$ and $N\downarrow(E_F) = 0$.

At the first stage, the system $SrFeO_3$–$SrSnO_3$, for which a continuous series of solid solutions $Sr(Fe_{1-x}Sn_x)O_{3-\delta}$ with the cubic structure (space group $Fm3m$) was obtained in [7], was studied in a wide range of concentrations $0.1 < x < 0.7$. The starting perovskites $SrFeO_3$ and $SrSnO_3$ and their mutual solid solution of

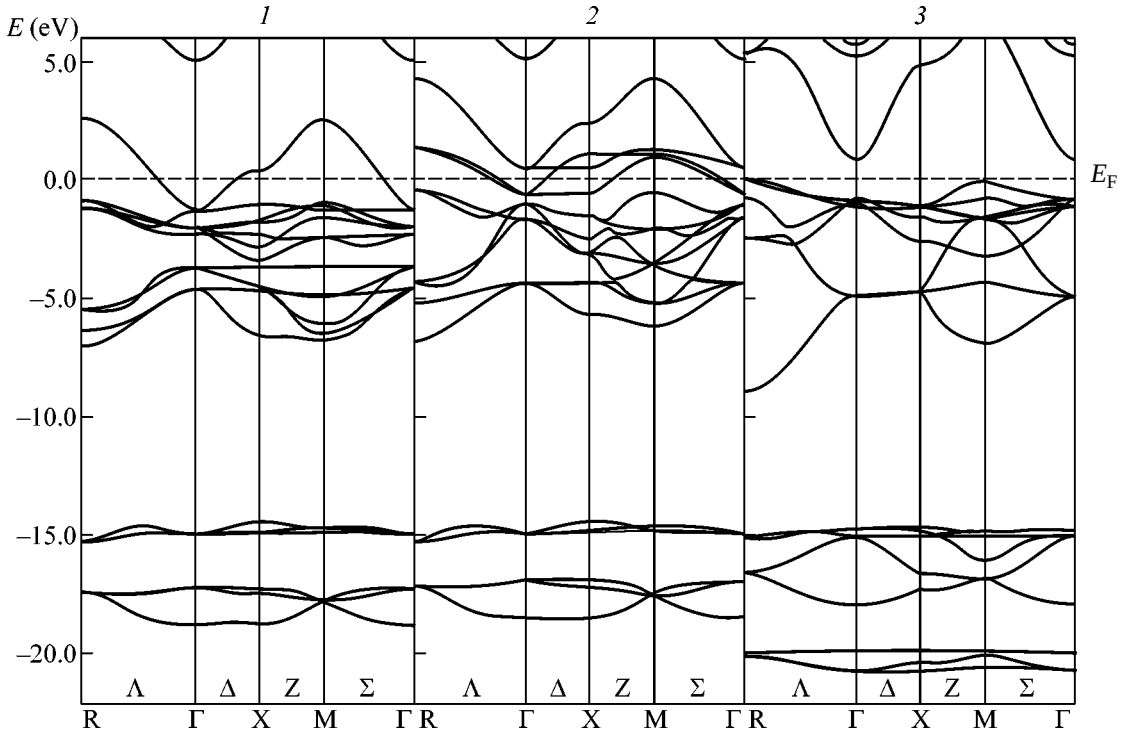

Fig. 1. Energy bands of ferromagnetic $SrFeO_3$ for (*1*) up and (*2*) down spin projections and (*3*) for the nonmagnetic phase of $SrSnO_3$.

the stoichiometric composition Sr_2FeSnO_6 were considered.

The calculations were performed within the local spin density functional approximation (LSDA) using the full-potential linearized-augmented-plane-wave (FLAPW) method (the WIEN2k code) [8]. The geometry of all the systems was optimized by the minimum condition for the total energy E_{tot}. For $SrFeO_3$, a comparative analysis of collinear magnetic FM and AFM (A, C, and G type) structures was performed; for $SrSnO_3$, two modifications were considered: the low-temperature orthorhombic (space group *Pbmn*) structure and the high-temperature cubic (space group *Fm*3*m*) structure.

According to the LSDA calculations, the ground state of $SrFeO_3$ is the FM phase and the others are arranged (in descending order of their stability) in the series FM > AFM(A) > AFM(C) > AFM(G). The features of the band structure of FM $SrFeO_3$ are determined by the spin polarization of the Fe3*d* bands and the differences in the hybridization of the $t_{2g}\downarrow, \uparrow$ and $e_g\uparrow, \downarrow$ orbitals with the $2p_{x,y,z}$ oxygen states (in the range from –7.2 eV to E_F, Fig. 1).The t_{2g} states are split into the mainly occupied $t_{2g}\uparrow$ band and the vacant $t_{2g}\downarrow$* band ($\Delta(t_{2g}\uparrow - t_{2g}\downarrow^*) \sim 1.9$ eV). The e_g states form a broad band and are responsible for the pd_σ Fe–O bonds. The metallic properties of the ferrite are determined by the Fe($t_{2g}\downarrow$, $e_g\uparrow$) orbitals, which make the main contribution (~64%) to $N(E_F)$. The intrinsic magnetic moments (MMs) for Fe equal 2.85 μ_B; the induced (through the iron–oxygen orbital overlap) magnetic moments of oxygen atoms are insignificant (~0.16 μ_B). Strontium is in a cationic form close to Sr^{2+}.

Both $SrSnO_3$ phases are nonmagnetic semiconductors. The energy gaps of the cubic and orthorhombic $SrSnO_3$ phases equal 1.03 and 1.70 eV, respectively.

According to our calculations, Sr_2FeSnO_6 differs radically in its electronic and magnetic properties from the starting systems and this material represents a half-metallic ferromagnet, Fig. 2. In Sr_2FeSnO_6, the Sr and Sn states are only slightly polarized (MM < 0.01 μ_B) and the induced MMs of oxygen atoms decrease two times as compared to those in FM $SrFeO_3$ (to ~0.08 μ_B) because of the appearance of nonmagnetic tin atoms in their nearest environment. On the contrary, the MMs of iron ions increase sharply (to 3.23 μ_B).

The spin-polarization effects of Fe3*d* $\uparrow\downarrow$ bands and the composition of the near-Fermi region of the spectrum are of particular interest. For the high-spin subsystem, the $t_{2g}\uparrow$ orbitals dominate in the occupied band and $e_g\uparrow$ orbitals dominate in the vacant band. The spectrum is of the metallic type. For the low-spin subsystem, the $e_g\downarrow$ and $t_{2g}\downarrow$ orbitals are entirely split into groups of occupied bonding (providing the σ and π Fe–O bonds) and vacant antibonding states; the spectrum is of the insulator type. The energy gap (~0.8 eV)

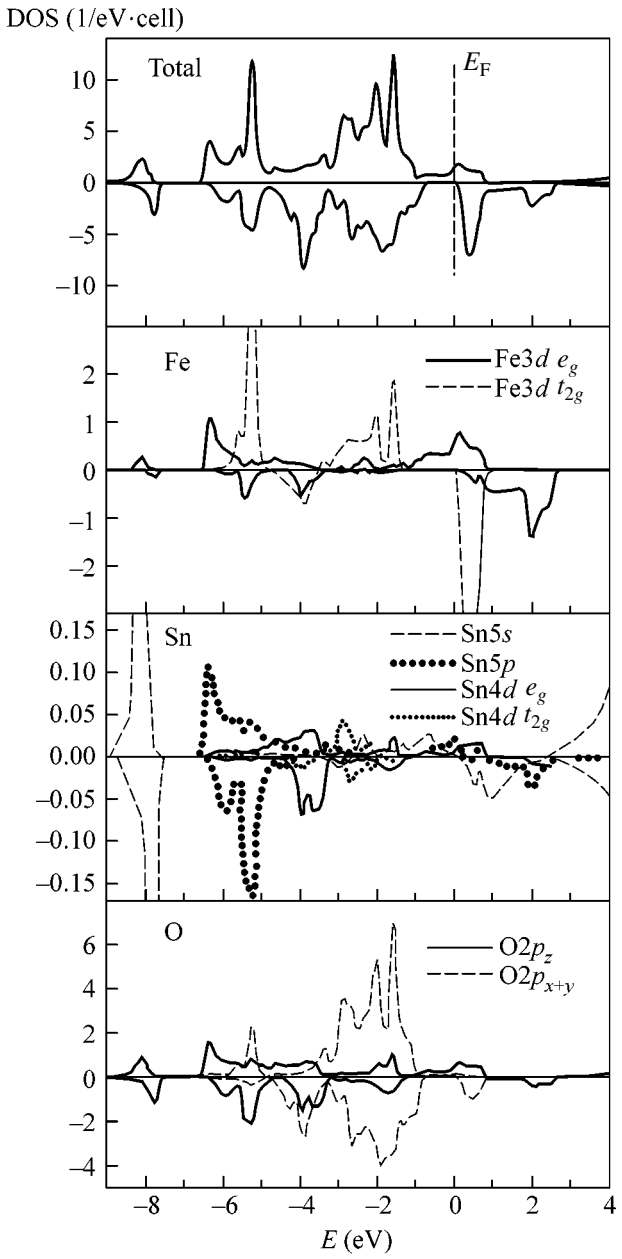

Fig. 2. (Upper panel) Total and (lower panels) partial densities of states of the half-metallic ferromagnet Sr_2FeSnO_6.

is indirect with a transition between the Γ–X points of the upper occupied Fet_{2g} ↓ and lower vacant Fet_{2g} ↓* bands. We emphasize that the splitting of the Fet_{2g} ↓, ↑ bands in Sr_2FeSnO_6 is large ($\Delta(t_{2g}\uparrow - t_{2g}\downarrow^*) \sim 4.7$ eV) and much larger than in $SrFeO_3$. As a result, the conductivity of the HMFM perovskite will be completely due to the Fee_g ↑ states.

The nature of the formation of the half-metallic state of Sr_2FeSnO_6 will be discussed starting with FM $SrFeO_3$. For this purpose, consider the main factors that affect the $SrFeO_3$ spectrum upon partial Sn⟶Fe substitution. The following properties change in this case: (i) the electron concentration (n_e, from 5.6 to 5.2 e/atom), (ii) the dimension factor (the lattice parameter a, relaxation of the oxygen sublattice), and (iii) conditions for the hybridization of the spin states Fe3d ↑↓–O2p upon changes in the nearest environment of oxygen (Fe–O–Fe ⟶ Fe–O–Sn).

Because the band spectrum of FM $SrFeO_3$ is continuous for both spin systems, the *concentration effect*, that is, the decrease in n_e (the shift of E_F down in the energy scale within the rigid band model), is not the reason for the formation of HMFM. In the analysis of the *dimension effect*, we will take into account that both an increase in the parameter a (by ~0.29 Å) and displacements of oxygen atoms from their ideal positions $d_{Fe-O}/a = 0.250$ (d_{Fe-O} is the Fe–O distance) to the positions $d_{Fe-O}/a = 0.242$ occur upon transition from $SrFeO_3$ to Sr_2FeSnO_6. Test calculations for $SrFeO_3$ with the parameter a equal to the optimized lattice parameter of Sr_2FeSnO_6 and with the relaxed oxygen sublattice, that is, with oxygen atoms displaced from their ideal positions to $d_{Fe-O}/a = 0.242$, revealed no substantial changes in the ferrite spectrum. Hence, the *hybridization effects* play the main role in the formation of the half-metallic state of Sr_2FeSnO_6. In this case, nonmagnetic tin atoms lead to the formation of an energy gap and modify the hybridization of spin states Fe3d ↑↓–O2p so that the condition of 100% spin polarization is fulfilled for the low-spin system.

It is evident that $SrSnO_3$ is not the only perovskite that can be used in searching for new HMFM materials. The families of $ASnO_3$ perovskites (A = Ca, Ba, Cd) and A_2SnO_3 pyrochlores (A = Y, La, Lu)—semiconductors with an energy gap from 3.0 to 4.8 eV [9]—can be indicated as the nearest candidates. Because of the closeness of the ionic radii of Sn^{n+} and Fe^{n+}, it is reasonable to expect the possibility of partial Fe⟶Sn substitution and the formation of mixed systems in which nonmagnetic (p^n) and magnetic (Fe) metal ions are present simultaneously. Their analysis represents a separate problem.

Here, we only present the results of LSDA calculations for systems of different type in which magnetic (Fe) and nonmagnetic (d^0) metal ions are present simultaneously: Sr_2FeTiO_6 and Sr_2FeZrO_6. As well as in the previous case, $Sr(Fe_{1-x}Ti_x)O_{3-\delta}$ and $Sr(Fe_{1-x}Zr_x)O_{3-\delta}$ solid solutions can be synthesized by known procedures [10, 11]. The data in Fig. 3, in which the results for Sr_2FeZrO_6 are demonstrated as an example, indicate that these double perovskites are also half-metallic ferromagnets. Their conductivity will be caused by the Fee_g ↑ states. Note that the replacement of the d^0 metal (Ti ⟷ Zr) leads to some changes in the distribution of high-spin near-Fermi states (the partial composition $N\uparrow(E_F)$) and in the energy gaps in the spectra of low-

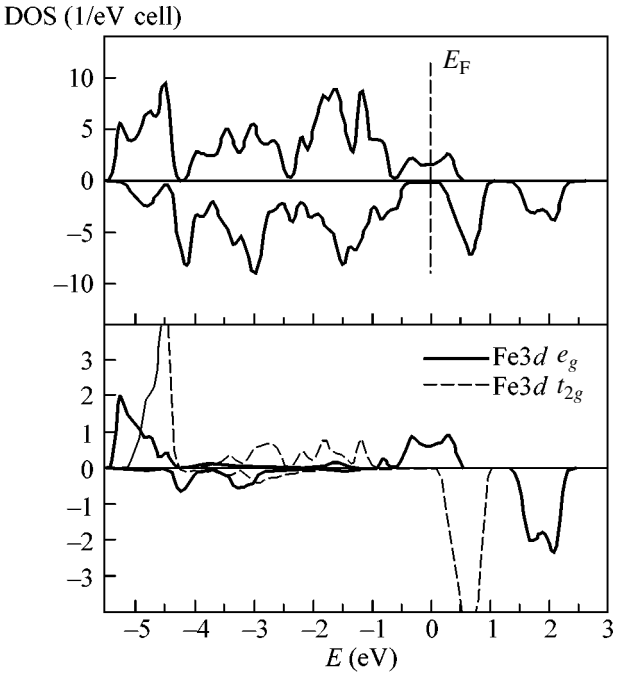

Fig. 3. (Upper panel) Total and (lower panel) partial Fed ↑↓ densities of states of the half-metallic ferromagnet Sr_2FeZrO_6.

spin states, which comprise 1.1 and 0.6 eV for Sr_2FeTiO_6 and Sr_2FeZrO_6, respectively.

Note that the proposed half-metallic ferromagnets represent only one, equiatomic (Fe/(Sn, Ti, Zr) = 1) composition of really synthesized continuous solid solutions $Sr(Fe_x(Sn, Ti, Zr)_{1-x})O_{3-\delta}$. This points to the possibility of controlling the properties of such materials by varying their composition "inside" the system without introducing other doping impurities. Additional methods of affecting the features of the distribution of spin states in the particular HMFM materials are associated with the nonstoichiometric effects in the oxygen sublattice and (or) with the doping of the sublattice A with atoms of alkaline-earth or *f* elements.

This work was supported by the Russian Academy of Sciences, program "Hydrogen Power and Fuel Cells."

REFERENCES

1. R. A. De Groot, F. M. Mueller, P. G. van Engen, and K. H. J. Buschow, Phys. Rev. Lett. **50**, 2024 (1983).
2. V. Yu. Irkhin and M. I. Katsnelson, Usp. Fiz. Nauk **164**, 705 (1994) [Phys. Usp. **37**, 659 (1994)].
3. I. Zutic, J. Fabian, and S. Das Sarma, Rev. Mod. Phys. **76**, 323 (2004).
4. W. E. Pickett and J. S. Moodera, Phys. Today **54**, 39 (2001).
5. H.-T. Jeng and G. Y. Guo, Phys. Rev. B **67**, 094438 (2003).
6. J. H. Park, S. K. Kwon, and B. I. Min, Phys. Rev. B **65**, 174401 (2002).
7. V. Thangadurai, P. Schmid Beurmann, and W. Weppner, Mater. Sci. Eng. B **100**, 18 (2003).
8. P. Blacha, K. Schwarz, G. K. H. Madsen, *et al.*, *WIEN2k, An Augmented Plane Wave Plus Local Orbitals Program for Calculations Crystal Properties* (Vienna Univ. of Technology, Vienna, 2001).
9. H. Mizoguchi, H. W. Eng, and P. M. Woodward, Inorg. Chem. **43**, 1667 (2004).
10. P. Adler and S. Eriksson, Z. Anorg. Allg. Chem. **626**, 118 (2000).
11. M. Wyss, A. Reller, and H. R. Oswald, Solid State Ionics **101**–**103**, 547 (1997).

Translated by A. Bagatur'yants

JETP Letters, Vol. 82, No. 4, 2005, pp. 224–227. From Pis'ma v Zhurnal Éksperimental'noĭ i Teoreticheskoĭ Fiziki, Vol. 82, No. 4, 2005, pp. 243–246.

Phase Transition with Suppression of Magnetism in $BiFeO_3$ at High Pressure¶

A. G. Gavriliuk[a, b, c], V. V. Struzhkin[a], I. S. Lyubutin[b], M. Y. Hu[d], and H. K. Mao[a]

[a] *Geophysical Laboratory, Carnegie Institution of Washington, Washington DC 20015, USA*

[b] *Institute of Crystallography, Russian Academy of Sciences, Moscow, 119333 Russia*

e-mail: lyubutin@ns.crys.ras.ru

[c] *Institute for High Pressure Physics, Russian Academy of Sciences, Troitsk, Moscow region, 142190 Russia*

[d] *HPCAT, Carnegie Institution of Washington, Advanced Photon Source, ANL, Argonne, IL 60439, USA*

Received July 5, 2005

The magnetic behavior of a $Bi^{57}FeO_3$ powdered sample was studied at high pressures by the method of nuclear forward scattering (NFS) of synchrotron radiation. The NFS spectra from ^{57}Fe nuclei were recorded at room temperature under high pressures up to 61.4 GPa, which were created in a diamond anvil cell. In the pressure interval $0 < P < 47$ GPa, the magnetic hyperfine field H^{Fe} at the ^{57}Fe nuclei increased reaching a value of ~52.5 T at 30 GPa, and then it slightly decreased to ~49.6 T at $P = 47$ GPa. As the pressure was increased further, the field H^{Fe} abruptly dropped to zero testifying a transition from the antiferromagnetic to a nonmagnetic state (magnetic collapse). In the pressure interval $47 < P < 61.4$ GPa, the value of H^{Fe} remained zero. The field H^{Fe} recovered to the low-pressure values during decompression. © *2005 Pleiades Publishing, Inc.*

PACS numbers: 71.27.+a, 71.30.+h, 81.40.Vw, 81.40.Tv

INTRODUCTION

The bismuth ferrite $BiFeO_3$ belongs to a class of ferromagnetoelectric materials (multiferroics) that have both a spontaneous electrical polarization and a spontaneous magnetization [1, 2]. Due to the record high antiferromagnetic Néel temperature (T_N = 643 K) and the ferroelectric's Curie temperature (T_C = 1083 K) between multiferroics [3, 4], the $BiFeO_3$ crystal is very attractive from both fundamental and applied aspects of science. It has the rhombohedrally distorted perovskite structure with space group $R3c$, and the unit cell parameters in the hexagonal representation are a = 5.58 and c = 13.9 Å (or a_r = 3.96 Å and $a_r = 0.6°$ in the rhombohedral setting) [5, 6].

In a local atomic scale, $BiFeO_3$ has the G-type antiferromagnetic structure, in which each iron ion has six iron neighbors with opposite spin directions [7]. However, the antiferromagnetic order is not homogeneous and a complex spatially modulated cycloid spin structure is present with a long wavelength of about 620 Å, which is incommensurate with the crystal lattice [8–11].

As was shown by Zvezdin and Pyatakov [1], the crystal symmetry of $BiFeO_3$ allows the existence of a linear magneto electric effect, spontaneous magnetization, and toroidal moment. However, due to the spatially modulated spin structure, these effects average to zero over the crystal volume and they can be observed only when the spatially modulated structure is destroyed [1]. Several mechanisms can suppress the modulated structure, and one of them is a strong applied magnetic field. The measurements in pulsed and static magnetic fields revealed an appearance of all three effects at the critical field of about 180–200 kOe when the modulated spin structure is transformed to a uniform state [12–14]. The substitution of rare-earth ions for bismuth ions in $BiFeO_3$ can also destroy (suppress) the spin modulation, and the magnetoelectric effect appears [15].

In the present study, external high pressures were applied to a $BiFeO_3$ crystal to modify its magnetic properties. The method of resonant nuclear forward scattering (NFS) of synchrotron radiation at ^{57}Fe nuclei was used to investigate the parameters of the magnetic hyperfine interactions.

EXPERIMENT

High-quality $BiFeO_3$ powder samples in which iron was enriched with ^{57}Fe isotope to 98% were prepared. For the high-pressure studies, a plate of $BiFeO_3$ was made by precompression of the initial powder between diamond anvils. The thickness of the plate was about 5–10 microns. In an optical microscope, the plate had a transparent deep red color. To perform the NFS studies at high pressures, a $Bi^{57}FeO_3$ plate with the dimensions

¶ The text was submitted by the authors in English.

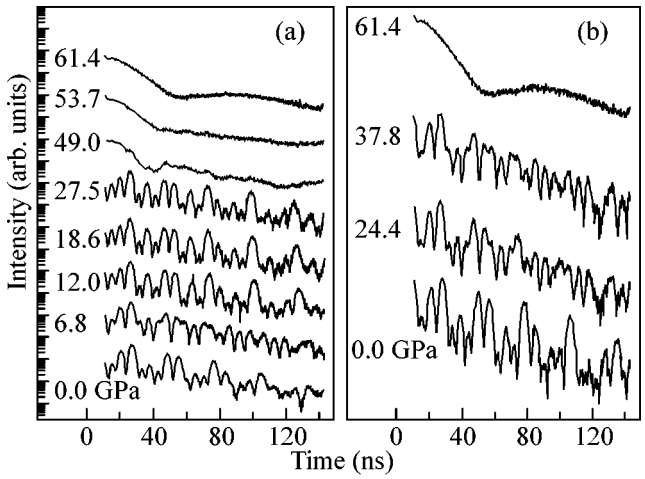

Fig. 1. Evolution of NFS time spectra in the $Bi^{57}FeO_3$ powder sample with pressure increase (a) and pressure decrease (b) runs. The spectra are recorded at room temperature without applying an external magnetic field.

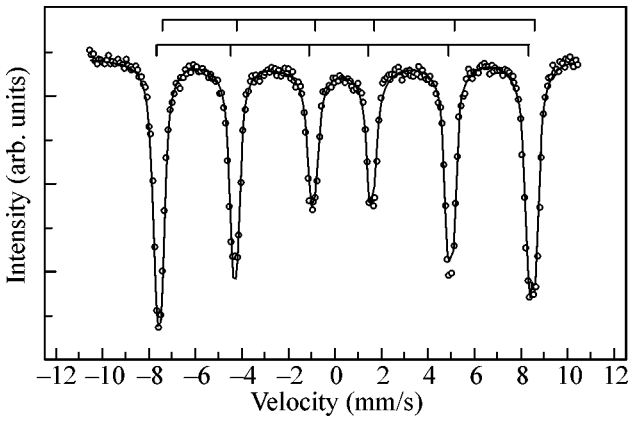

Fig. 2. The ^{57}Fe-Mössbauer absorption spectrum of the $Bi^{57}FeO_3$ powder sample recorded at room temperature in transmission geometry. The symbols are the experimental points. The resulting fit to two subspectra is shown by a solid line.

$\sim 90 \times 90\ \mu m^2$ was placed into a high-pressure cell with diamond anvils. The diameter of the working surface of the diamonds in the cell was about 300 μm, and the diameter of the hole in the rhenium gasket where the sample was placed was about 100 μm. To create a quasi-hydrostatic pressure, the working volume of the cell was filled with the polyethyl-siloxane liquid PES-5. The pressure value was determined by the standard ruby fluorescence technique. Several ruby chips with dimensions of about 1 μm were placed into the cell along with the sample. They were placed at different distances from the center of the working volume to evaluate the pressure gradient in the chamber.

The NFS experiments were performed at the 16-ID-D beamline at the Advanced Photon Source at Argonne National Laboratory. The time spectra of the NFS from the ^{57}Fe nuclei (which may be considered as the *time-domain* Mössbauer spectra [16]) were recorded at room temperature in the pressure range up to $P = 61.4$ GPa during compression and decompression runs. A high-resolution monochromator with a 2.2 meV bandwidth was tuned to the nuclear resonance energy of 14.4125 keV of the Mössbauer transition in the ^{57}Fe [17]. The polarization vector of the gamma rays was horizontal and parallel to the sample plane.

Figure 1 presents the scattered radiation intensity versus the time that elapsed after the nuclear excitation by an incident pulse. The measurements for different pressure values were performed in the 24 bunches mode of operation. These bunches were evenly distributed with 154 ns separation between them. The damped decay of the nuclear excitation was modulated in time by quantum and dynamic beats. The quantum beats were caused by the interference of the scattered radiation components with different frequencies as a result of the nuclear level splitting into sublevels due to the hyperfine interaction. The period of the quantum beats is inversely proportional to the hyperfine splitting and, in the case under study, to the magnetic field H^{Fe} at the iron nuclei. The dynamic beats are caused by multiple scattering processes and are determined by the sample thickness. A detailed description of the method can be found in review [18].

Under pressures below 47 GPa, the main feature of the spectra is pronounced quantum beats. The spectra indicate that, over the whole pressure range from ambient pressure to 47 GPa, the period of beats slightly decreases indicating an increase of the magnetic hyperfine field H^{Fe} under pressure. When the pressure increases above 47 GPa, the high frequency quantum beats disappear signaling the disappearance of the magnetic field H^{Fe} at the ^{57}Fe nuclei (Fig. 1). At decompression from the maximum pressure of 61.4 GPa to below 47 GPa, high frequency quantum beats appeared again indicating the reversibility of the magnetic transition. At ambient pressure, the value of the field H^{Fe} calculated from the NFS spectra is 49.3 T, which is consistent with that obtained from previous Mössbauer [19, 20] and NMR [21, 10] experiments.

We also recorded the ^{57}Fe-Mössbauer absorption spectrum of our $Bi^{57}FeO_3$ sample in transmission geometry (Fig. 2). At room temperature, the six-line spectrum has slightly broadened resonance lines with a noticeable asymmetry of the first and sixth lines. As it was suggested by Zalesskii *et al.* [21] from analysis of the NMR data, such features of the spectrum may appear due to a distribution of values of the magnetic hyperfine fields at iron nuclei. In the spatially modulated cycloid spin structure of the $BiFeO_3$ crystal, the magnetic moments of Fe ions turn in the plane perpendicular to the hexagonal plane along the propagation

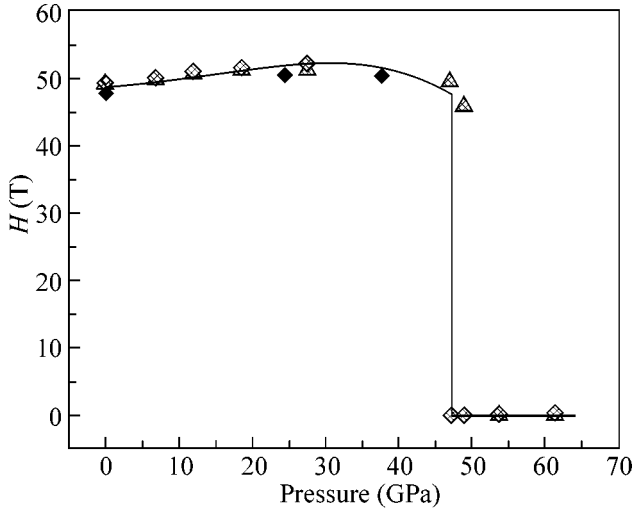

Fig. 3. Pressure dependence of the magnetic hyperfine field at ^{57}Fe nuclei in $Bi^{57}FeO_3$ for the pressure increase (gray triangles and diamonds) and pressure decrease (black triangles) regimes. The solid line is a guide for the eye. The value of H^{Fe} from the Mössbauer absorption spectrum under normal conditions is represented by the white diamond symbol.

direction of the spin-modulated wave (*c*-axis). Due to a variation of the dipole contribution to the magnetic hyperfine field H^{Fe}, this field becomes a periodic function of a coordinate in the crystal lattice with two maxima corresponding to the spin alignments parallel $H_\parallel$ and perpendicular $H_\perp$ to the crystal *c*-axis [10]. Taking into account these ideas, we successfully fit the Mössbauer spectrum (Fig. 2) to two six-line components and obtained the following parameters: $H_\parallel^{Fe} = 49.96(8)$ T, and $H_\perp^{Fe} = 49.73(8)$ T.

RESULTS AND DISCUSSION

The NFS spectra were processed by the MOTIF program, which was developed by Shvyd'ko [22, 23]. The large number of quantum beats in each spectrum (more than 20) allows us to obtain the value of the magnetic field H^{Fe} at the ^{57}Fe nuclei with high accuracy. The field H^{Fe}, being the main parameter of this study, practically does not correlate with the other parameters of the spectrum such as the sample thickness, the quadrupole hyperfine splitting, and the azimuthal orientation of the iron magnetic moment. All these parameters may affect only the relative heights of individual peaks of the high frequency quantum beats.

The room-temperature pressure dependence of the magnetic hyperfine field H^{Fe} is shown in Fig. 3. The field increases from ~49.3 T at ambient pressure to a maximum value of ~52.5 T at $P \sim 30$ GPa, and then it slightly decrease to about 49.6 T at further pressure increase. At $P \sim 47$ GPa, the magnetic field drops to zero, pointing to an abrupt transition of the sample from the magnetically ordered to a nonmagnetic state. Observations with an optical microscope revealed that, after this transition, the sample, having been deep red in color at ambient pressure, darkens and becomes opaque. Presumably, this effect is due to a drastic decrease in the optical gap and may imply a transition from the insulating to a metallic state.

It follows from Fig. 3 that the increase in the magnetic field with pressure up to 30 GPa is almost linear. The pressure dependence of the field can be given as $H^{Fe} = H_0^{Fe} + k_H P$ with the parameters $H_0^{Fe} = 49.5 \pm 0.2$ T and $k_H = 0.09 \pm 0.01$ T/GPa. Apparently, the magnetic field increase with pressure is due to the increase in the exchange interaction as a result of enhancing of covalent bonding owing to the decrease in the Fe–O–Fe interionic distances. A nonlinear behavior of the field with further pressure increase to 47 GPa is under question and may be related to some transformation in the crystal structure or/and possibly electronic and magnetic transitions.

The most important effect is the abrupt disappearance of the magnetic field at the iron nuclei at $P \sim 47$ GPa. This effect occurs due to the transition of the $BiFeO_3$ crystal to a nonmagnetic state, thus, demonstrating the collapse of the localized magnetic moment of iron. Several mechanisms for explaining such a magnetic collapse can be proposed.

(1) A structural phase transition resulting in the formation of a new $BiFeO_3$ phase with the Néel point T_N below room temperature. In this case, the magnetic transition at $P = 47$ GPa is a transition from an antiferromagnetic to a paramagnetic insulating state.

(2) An insulator-to-metal transition at which the 3*d* electrons of the Fe^{3+} ions are delocalized and form a conduction band. In this case, the magnetic state of the material is determined by the band mechanism and depends on the band structure. Then, the magnetic transition at $P = 47$ GPa can be a transition from an antiferromagnetic to a paramagnetic metallic state.

(3) A transition of the iron ions from the high-spin to the low-spin state analogous to the phenomenon that was recently observed in several complex iron oxides in the pressure range of 30–50 GPa [24–27]. As follows from the Mössbauer spectra parameters (Fig. 2), the trivalent iron ions in $BiFeO_3$ are in the high-spin state $S = 5/2$ at normal pressure. The low-spin state $S = 1/2$ of the Fe^{3+} ions is not diamagnetic, but the Néel point T_N of such a material should be much lower than for materials with Fe^{3+} ions in the high-spin state. For example, in the mean-field approximation, it follows from the ratio $k_B T_N \propto AJS(S + 1)$, where J is an exchange integral, k_B is Bolzman's parameter, and A is a constant. In this case, the observed magnetic transition is a transition from the high-spin antiferromagnetic to the low-spin paramagnetic state.

The measurements of the nuclear isomer shifts (IS) and quadruple splitting (QS) would give direct information about the iron spin states [28]. In our study of the NFS spectra, we did not intend to measure the IS and QS parameters, which would require a more sophisticated experimental technique. However, the IS and QS values can be reasonably obtained from conventional Mössbauer absorption spectroscopy at high pressures, which we are going to perform in the near future. Additional information about the spin states of ions can be obtained from the high resolution X-ray emission spectroscopy technique, which is now available using synchrotron radiation facilities (a description of this method can be seen elsewhere [29]). These types of experiments, as well as high-pressure X-ray diffraction studies of the $BiFeO_3$ crystal structure, are part of our next plan.

We are grateful to Prof. A.A. Bush for preparation of the $BiFeO_3$ compound enriched with Fe-57 isotope and to Dr. K.V. Frolov for help in the Mössbauer absorption measurements. This work was supported by DOE grant no. DE-FG02-02ER45955, by the Russian Foundation for Basic Research (project nos. 04-02-16945-a and 05-02-16142-a), and by the Program of the Physical Branch of the Russian Academy of Sciences under the project "Strongly Correlated Electronic Systems." HP-CAT is a collaboration among the Carnegie Institution, Lawrence Livermore National Laboratory, the University of Hawaii, the University of Nevada in Las Vegas, and the Carnegie/DOE Alliance Center (CDAC) and is supported by the DOE-BES, DOE-NNSA, NSF, DOD-TACOM, and the W.M. Keck Foundation. The use of the Advanced Photon Source is supported by the U.S. Department of Energy, Basic Energy Sciences, Office of Science (under Contract no. W-31-109-EN).

REFERENCES

1. A. K. Zvezdin and A. P. Pyatakov, Phys. Usp. **47** (4), 8 (2004).
2. G. A. Smolenskii and I. Chupis, Sov. Phys. Usp. **25**, 475 (1982).
3. G. A. Smolenskii, V. Yudin, E. Sher, *et al.*, Sov. Phys. JETP **16**, 622 (1963).
4. Yu. N. Venevtsev, G. Zhdanov, and S. Solov'ev, Sov. Phys. Crystallogr. **4**, 538 (1960).
5. P. Fischer, M. Polomskya, I. Sosnowska, *et al.*, J. Phys. C **13**, 1931 (1980).
6. J. D. Bucci, B. K. Robertson, and W. J. James, J. Appl. Crystallogr. **5**, 187 (1972).
7. S. V. Kiselev, R. P. Ozerov, and G. S. Zhdanov, Sov. Phys. Dokl. **7**, 742 (1963).
8. I. Sosnowska, T. Peterlin-Neumaier, and E. Steichele, J. Phys. C **15**, 4835 (1982).
9. I. Sosnowska, M. Loewenhaupt, W. I. F. David, *et al.*, Physica B (Amsterdam) **180–181**, 117 (1992).
10. A. V. Zalesskii, JETP **95**, 101 (2002).
11. J. Wang, J. Neaton, and H. Zheng, Science **299**, 1719 (2003).
12. Yu. F. Popov, Ferroelectrics **162**, 135 (1994).
13. Yu. F. Popov, A. M. Kadomtseva, S. Krotov, *et al.*, Low Temp. Phys. **27**, 478 (2001).
14. B. Ruette, Phys. Rev. B **69**, 064114 (2004).
15. A. M. Kadomtseva, Physica B (Amsterdam) **211**, 327 (1995).
16. R. Ruffer and A. I. Chumakov, Hyperfine Interact. **97–98**, 589 (1996).
17. Yu. V. Shvyd'ko, M. Lerche, J. Jäschke, *et al.*, Phys. Rev. Lett. **85**, 495 (2000).
18. G. V. Smirnov, Hyperfine Interact. **123–124**, 31 (1999).
19. C. Blaauw and F. van der Woude, J. Phys. C **6**, 1422 (1973).
20. J. De Sitter *et al.*, Solid State Commun. **18**, 645 (1976).
21. A. V. Zalesskii, A. K. Zvezdin, A. A. Frolov, and A. A. Bush, JETP Lett. **71**, 465 (2000).
22. Yu. V. Shvyd'ko, Phys. Rev. B **59**, 9132 (1999).
23. Yu. V. Shvyd'ko, Hyperfine Interact. **125**, 173 (2000).
24. A. G. Gavriliuk, I. A. Trojan, I. S. Lyubutin, *et al.*, JETP **100**, 688 (2005).
25. A. G. Gavriliuk, I. A. Trojan, S. G. Ovchinnikov, *et al.*, JETP **99**, 566 (2004).
26. A. G. Gavriliuk, S. A. Kharlamova, I. S. Lyubutin, *et al.*, JETP Lett. **80**, 426 (2004).
27. A. G. Gavriliuk, I. A. Troyan, R. Boehler, *et al.*, JETP Lett. **77**, 619 (2003).
28. V. A. Sarkisyan, I. A. Troyan, I. S. Lyubutin, *et al.*, JETP Lett. **76**, 664 (2002).
29. J. Badro, G. Fiquet, V. V. Struzhkin, *et al.*, Phys. Rev. Lett. **89**, 205504 (2002).

JETP Letters, Vol. 82, No. 4, 2005, pp. 228–231. Translated from Pis'ma v Zhurnal Éksperimental'noĭ i Teoreticheskoĭ Fiziki, Vol. 82, No. 4, 2005, pp. 247–250.

Nonmonotonic Behavior of the Absorption of the Tightly Focused Femtosecond Radiation of a Cr:Forsterite Laser in a Dielectric Due to an Increase in the Number of Photons Involved in the Process

V. M. Gordienko, P. M. Mikheev, and V. S. Syrtsov

Faculty of Physics and International Laser Center, Moscow State University, Vorob'evy gory, Moscow, 119992 Russia

e-mail: mikheev@femto.phys.msu.ru

Received July 7, 2005

In the tight focusing mode of the femtosecond radiation of a Cr:forsterite laser system in the transparent-dielectric bulk, the nonmonotonic behavior of absorption has been revealed as the laser pulse energy increases. The effect is caused by a change in the number of photons involved in ionization due to an increase in the effective ionization potential. © *2005 Pleiades Publishing, Inc.*

PACS numbers: 42.25.Bs, 42.70.Mp

The tight focusing of femtosecond laser radiation of sub- and microjoule energy levels into the bulk of transparent condensed matter makes it possible to achieve an intensity of ~10^{13} W/cm^2 in the beam waist without the breakdown of the sample surface. For the laser pulse power exceeding the critical self-focusing power, the field ionization of a substance occurs due to an increase in intensity, which finally results in the formation of a plasma channel [1–4]. After the passage of a light pulse, the energy of the electron component of the plasma is transferred to the crystal lattice of the substance and residual modification can arise in the dielectric bulk when the fraction of the absorbed energy is sufficient. Thus obtained micromodifications are of interest for the three-dimensional recording of information [5] and creation of waveguide structures [6–9]. The laser pulse energy absorbed in the dielectric is a key parameter determining the sizes of the plasma channel [4, 10]. In available experimental works performed with visible radiation, the dependence of the absorbed energy on the incident energy is monotonic [10, 11].

In this paper, we report on the experimental effect of the nonmonotonic energy dependence of the absorption of tightly focused femtosecond laser radiation. In the experiment, we used the radiation of femtosecond Cr:forsterite laser system generating light pulses 100 fs in duration at a wavelength of 1.24 μm. The pulse energy varied in a range of 0.1–10 μJ by means of neutral light filters. We investigated a KDP crystal into the bulk of which laser radiation was directed by means of an aspheric lens with a focal length of 2 mm ($F/D \sim 1$). After each pulse, the crystal was shifted by 20 μm for further interaction with an unmodified volume. The energies of the initial radiation and radiation passed through the crystal were measured by photodiodes, and the aperture of the detector at the crystal output is twice as large as the diameter of the laser beam that has passed.

The pulse energy dependence of the laser energy transmission measured for the KDP crystal is shown in Fig. 1. We note that the propagation of intense laser radiation through the crystal was accompanied by the generation of the second harmonic with a maximum

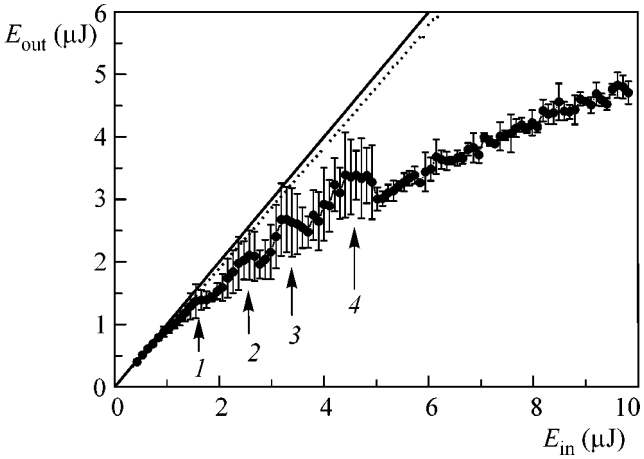

Fig. 1. Nonlinear transmission of laser energy in the KDP crystal: points are experimental data, the solid straight line corresponds to the absence of absorption in the crystal, and the dotted line corresponds to the transmission with allowance for only losses on the generation of the second harmonic. The arrows with digits indicate the regions where the number of photons involved in absorption changes.

0021-3640/05/8204-0228$26.00

efficiency of no more than 8%, which was detected by a Solar TII SL-40-2-3648USB spectrometer. Losses of the main radiation are shown by the dotted line in Fig. 1. Their contribution to the crystal transmission is evidently immaterial. The use of the tight focusing of radiation in the crystal in the experiment made it possible to exclude the generation of the supercontinuum.

The laser radiation absorption in the crystal begins at a pulse energy of about 1 μJ corresponding to a power of 10 MW, which is close to the theoretical critical power of self-focusing $P_{cr} = \lambda^2/2\pi n_0 n_2 \approx 7$ MW (where $n_0 = 1.5$ and $n_2 = 2.5 \times 10^{-16}$ cm^2/W is the nonlinear refractive index [12]). In this case, four pronounced steplike changes (they are indicated by the arrows in Fig. 1) are observed in the dependence of nonlinear transmission of light energy in the crystal. The measurement errors are obtained by averaging over 30–40 pulses at each point in an energy range of 1–5 μJ and over 5–10 pulses in the remaining region.

To interpret the experimental results, we used the following interaction model. We assume that radiation propagates in a homogeneous plasma channel with constant intensity, which increases with the laser pulse energy.

At the initial stage, basic energy losses in the crystal are caused by the field ionization of the medium [10, 13]. In the general case, the efficiency of the field ionization of the dielectric, including multiphoton and tunnel ionizations, is described by the general Keldysh formula for crystalline media [14], where the parameters of the medium are the effective ionization potential:

$$\Delta_{\text{eff}} = \frac{2}{\pi}\Delta\frac{\sqrt{1+\gamma^2}}{\gamma}E\left(\frac{1}{\sqrt{1+\gamma^2}}\right). \quad (1)$$

Here, Δ is the energy gap of the crystal, $E(x)$ is the elliptic integral of the second kind, and the Keldysh parameter is given by the expression [14]

$$\gamma = \omega\sqrt{m_r\Delta}/(eE_L), \quad (2)$$

where E_L and ω are the amplitude and frequency of the electric field, respectively; e is the elementary charge; and m_r is the reduced electron mass. The reduced electron mass for the KDP crystal is unknown. For this reason, the calculations were performed with a value of $0.6m_e$ (m_e is the electron mass) for the other dielectric, fused silica [2]. A change in the reduced electron mass leads to a proportional change in the laser radiation intensity and does not affect the physical essence of the estimates. The general Keldysh formula is used due to the necessity of taking into account both the multiphoton and tunnel ionizations of the medium, because the parameter γ is about 1 for a laser radiation intensity of 10^{13} W/cm^2.

The effective ionization potential is a monotonically increasing function of the laser radiation intensity. In turn, the number of photons involved in the process is defined as

$$N_{\text{ph}} = \left[\frac{\Delta_{\text{eff}}}{\hbar\omega}\right] + 1, \quad (3)$$

where the square brackets stand for the integer part of the number. Thus, the number of photons involved in the process can increase stepwise when the radiation intensity in the plasma channel increases. This behavior leads to a sharp decease in the ionization rate and, as a consequence, to a nonmonotonic dependence of the laser radiation absorption in the crystal. Figure 2a shows the volume field-ionization rate calculated as a function of the laser radiation intensity by the general

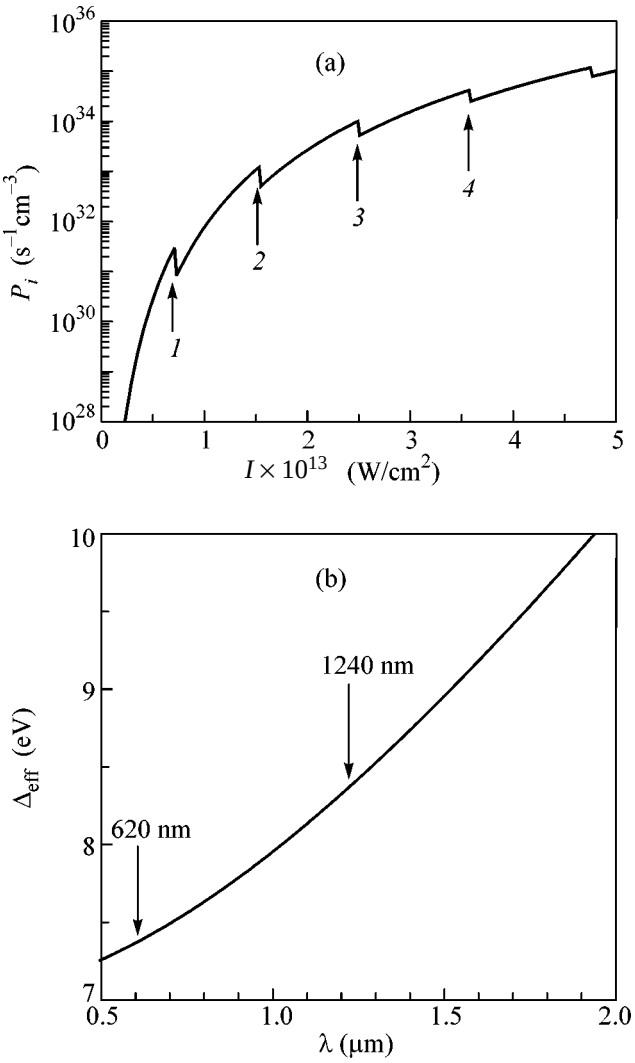

Fig. 2. (a) Laser radiation intensity dependence of the volume ionization rate calculated for the KDP crystal by the general Keldysh formula and (b) the effective ionization potential of the KDP crystal vs. the laser radiation wavelength ($I \sim 10^{13}$ W/cm^2, $m_r = 0.6m_e$). The arrows with digits indicate the regions where the number of photons involved in the absorption changes.

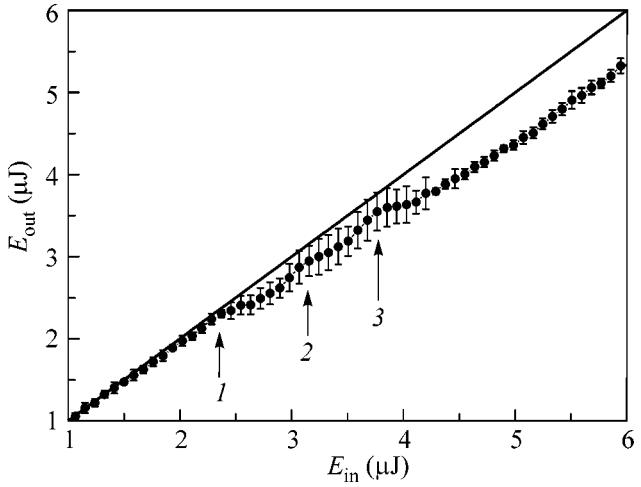

Fig. 3. Nonlinear transmission of laser energy in the $LiNbO_3$ crystal: the points are experimental data and the solid straight line corresponds to the absence of absorption in the crystal. The arrows with digits indicate the regions where the number of photons involved in absorption changes.

Keldysh formula for the KDP crystal. The arrows indicate regions where the number of photons involved in the process increases.

For the KDP crystal with the energy gap $\Delta \approx 7$ eV [15] and photon energy $\hbar\omega \approx 1$ eV, we obtain $N_{ph} = 8$. According to Eqs. (1)–(3) with the data shown in Fig. 2a, the number of photons involved in the process increases first to 9 at a radiation intensity of about 0.7×10^{13} W/cm^2, and the second, third, and fourth increases (to 10, 11, and 12, respectively) occur at $I_3 \sim 1.5 \times 10^{13}$ W/cm^2, $I_4 \sim 2.5 \times 10^{13}$ W/cm^2, and $I_5 \sim 3.6 \times 10^{13}$ W/cm^2, respectively. For higher pulse energies, the radiation intensity in the plasma channel is stabilized [3, 10], which is manifested in the absence of a further increase in the number of photons involved in absorption. We emphasize that considerable suppression of the radiation absorption has been achieved in a number of experimental realizations.

According to the numerical calculations presented in [11], a considerable increase in the measurement error in the regions, where the number of photons involved in the process increases, can be caused by a change in the intensity in the plasma channel. In the regions where the number of photons increases a transmission change is expected to be sensitive to intensity fluctuations. The dependence shown in Fig. 1 is smoothed, because it is obtained by averaging over a large number of experimental realizations.

According to Eqs. (1)–(3), the effective ionization potential and, therefore, the number of photons involved in the process depend strongly on the laser radiation wavelength (see Fig. 2b). This means that the nonmonotonic behavior of the nonlinear transmission of the crystal for IR radiation is necessarily much more pronounced than that for visible radiation. The nonmonotonic incident energy dependence of the absorbed laser energy was not observed for the KDP crystal in our previous similar measurements with tightly focused visible femtosecond laser radiation with a wavelength of about 0.6 μm [10, 16]. Such a dependence is absent in the results of recent experiments on the interaction of 0.8-μm tightly focused laser radiation with fused silica [11].

The theoretical estimates confirm the measurement results. In particular, for 620-nm radiation ($\hbar\omega = 2$ eV), the initial number of photons involved in absorption in the KDP crystal is equal to four. For the first and second changes in this number (to five and six, respectively), laser radiation intensities of 3×10^{13} W/cm^2 and 10^{14} W/cm^2, respectively, are necessary in the plasma channel. In [17], as well as in our experiments on the formation of plasma channels in fused silica and the KDP crystal [4, 10], the laser radiation intensity is no more than 3×10^{13} W/cm^2. The situation for quartz is similar. Thus, only a single change in the number of photons involved in absorption can be observed in the best case when visible laser radiation is used.

According to Eqs. (1)–(3), an increase in the effective ionization potential depends slightly on the energy gap of the crystal. Therefore, a step change in the laser radiation transmission is expected to be a general effect. We also measured the transmission of the tightly focused radiation of a Cr:forsterite laser system in the $LiNbO_3$ crystal (see Fig. 3). The statistics of the measurements were similar to the measurements with the KDP crystal. The dependence exhibits three pronounced step changes in the transmission. The initial number of photons involved in ionization in the $LiNbO_3$ crystal is equal to four. The first (to five photons), second, and third changes in the number of photons involved in ionization occur at laser radiation intensities of 5×10^{12}, 2×10^{13}, and 3.7×10^{13} W/cm^2, respectively. Similar to the case of the KDP crystal, the intensity in the channel for higher energies of a pulse is stabilized and this stabilization is manifested in the absence of a further increase in the number of photons involved in the process.

The effect of a step change in the absorption of femtosecond IR laser radiation with an intensity of about 10^{13} W/cm^2 in a transparent dielectric is consistent with the prediction of the Keldysh theory concerning an increase in the number of photons involved in field ionization in crystal media due to an increase in the effective ionization potential in a field of intense laser radiation.

Moreover, a change in the number of photons involved in ionization can occur in gaseous media, because the effective atomic ionization potential depends on the oscillatory electron energy [14]. This circumstance should be taken into account in numerical simulation of the propagation and filamentation of intense IR laser radiation in the atmosphere. In the lat-

ter case, a decrease in the radiation absorption due to an increase in the number of photons involved in ionization in the central part of the beam can lead to a change in the dynamics of the channel formation accompanying the radiation propagation.

This work was supported by the Russian Foundation for Basic Research (project no. 03-02-16973).

REFERENCES

1. P. Audebert, Ph. Daguzan, A. Dos Santos, *et al.*, Phys. Rev. Lett. **73**, 1990 (1994).
2. L. Sudrie, A. Couairon, M. Franco, *et al.*, Phys. Rev. Lett. **89**, 186601 (2002).
3. V. M. Gordienko, I. A. Makarov, and P. M. Mikheev, in *Program of Conference ICONO/LAT 2005* (St. Petersburg, 2005), p. 63.
4. E. A. Chutko, M. Gordienko, B. A. Kirillov, *et al.*, Laser Phys. **13**, 1102 (2003).
5. Y. Kawata, H. Ishitobi, and S. Kawata, Opt. Lett. **23**, 756 (1998).
6. M. Kamata, K. Ohta, M. Obara, *et al.*, Proc. SPIE **4977**, 394 (2003).
7. J. W. Chan, T. R. Huser, S. H. Risbud, *et al.*, Appl. Phys. Lett. **82**, 2371 (2003).
8. R.-X. Gao, J.-H. Zhang, L.-G. Zhang, *et al.*, Chin. Phys. Lett. **19**, 1424 (2002).
9. V. Mizeikis, H.-B. Suna, A. Marcinkevicius, *et al.*, J. Photochem. Photobiol. A **145**, 41 (2001).
10. V. M. Gordienko, I. A. Makarov, P. M. Mikheev, *et al.*, Quantum Electron. (Moscow) **35**, 627 (2005).
11. A. Couairon, L. Sudrie, M. Franco, *et al.*, Phys. Rev. B **71**, 125435 (2005).
12. R. A. Ganeev, I. A. Kulagin, A. I. Ryasnyansky, *et al.*, Opt. Commun. **229**, 403 (2004).
13. A. Kaiser, B. Rethfeld, M. Vicanek, and G. Simon, Phys. Rev. B **61**, 11 437 (2000).
14. L. V. Keldysh, Zh. Éksp. Teor. Fiz. **47**, 1945 (1964) [Sov. Phys. JETP **20**, 1307 (1964)].
15. V. G. Dmitriev, G. G. Gurzadyan, and D. N. Nikogosyan, *Handbook of Nonlinear Optical Crystals* (Springer, Berlin, 1997).
16. V. M. Gordienko, I. A. Makarov, P. M. Mikheev, *et al.*, Proc. SPIE **5399**, 96 (2004).
17. S. Tzortzakis, L. Sudrie, B. Prade, *et al.*, Phys. Rev. Lett. **87**, 213902 (2001).

Translated by R. Tyapaev

JETP Letters, Vol. 82, No. 4, 2005, pp. 232–235. From Pis'ma v Zhurnal Éksperimental'noĭ i Teoreticheskoĭ Fiziki, Vol. 82, No. 4, 2005, pp. 251–254.

Josephson Vortex Lattice Melting in Bi-2212 Probed by Commensurate Oscillations of Josephson Flux-Flow¶

Yu. I. Latyshev[a, *], V. N. Pavlenko[a], A. P. Orlov[a], and X. Hu[b]

[a] *Institute of Radio Engineering and Electronics, Russian Academy of Sciences, Moscow, 125009 Russia*

** e-mail: lat@cplire.ru*

[b] *National Institute for Materials Science, 305-0047 Ibaraki, Japan*

Received July 7, 2005

We studied the commensurate semifluxon oscillations of Josephson flux-flow in Bi-2212 stacked structures near T_c as a probe of melting of a Josephson vortex lattice. We found that oscillations exist above 0.5 T. The amplitude of the oscillations is found to decrease gradually with the temperature and to turn to zero without any jump at $T = T_0$ (3.5 K below the resistive transition temperature T_c), thus, indicating a phase transition of the second order. This characteristic temperature T_0 is identified as the Berezinskii–Kosterlitz–Thouless (BKT) transition temperature, T_{BKT}, in the elementary superconducting layers of Bi-2212 at zero magnetic field. On the basis of these facts, we infer that melting of a triangular Josephson vortex lattice occurs via the BKT phase with formation of characteristic flux loops containing pancake vortices and antivortices. The *B–T* phase diagram of the BKT phase found from our experiment is consistent with theoretical predictions. © *2005 Pleiades Publishing, Inc.*

PACS numbers: 74.25.Qt, 74.25.Dw, 74.50.+r, 74.72.Hs

The vortex phase diagram in layered high-T_c materials in parallel magnetic fields is significantly less studied than for perpendicular fields. This is related to the great difficulty in visualization of Josephson vortices [1] and the Josephson vortex lattice (JVL) [2]. Recently, a method of identification of triangular JVL has been found [3]. It was demonstrated as oscillations of Josephson flux-flow resistance in narrow Bi-2212 mesa structures in a parallel field with a periodicity of $\frac{1}{2}\Phi_0$ per elementary Josephson junction. The effect has been interpreted as a result of commensurability of a triangular JVL period with mesa width. In this paper (see also [4]) we develop an idea to use the effect of Josephson flux-flow (JFF) commensurate oscillations for probing of JVL melting. In a triangular lattice, the periodic rows of JVs in adjacent layers are shifted by π. Therefore, JFF oscillations with semifluxon periodicity reflect the transverse coherence of a triangular lattice. The melting of a triangular lattice should be accompanied by a loss of transverse coherence and, as a result, by disappearance of semifluxon oscillations. Different scenarios of melting can occur: melting into the liquid phase or melting into the Berezinskii–Kosterlitz–Thouless (BKT) phase [5–7]. For the latter case, the possibility of second order transition has been considered [7, 8]. The influence of BKT transition on a JVL phase at high fields and high temperatures has been widely debated [5–9]. However, until recently, there were no systematic experimental studies of JVL melting.

The experiment was carried out on stacked structures of slightly overdoped Bi-2212 with lateral sizes of $L_a \times L_b = 15–30\ \mu m \times 3–5\ \mu m$ containing about 100 elementary junctions (Fig. 1). The structures were fabricated by double sided processing of Bi-2212 whiskers by a focused ion beam (FIB) [10]. The field was ori-

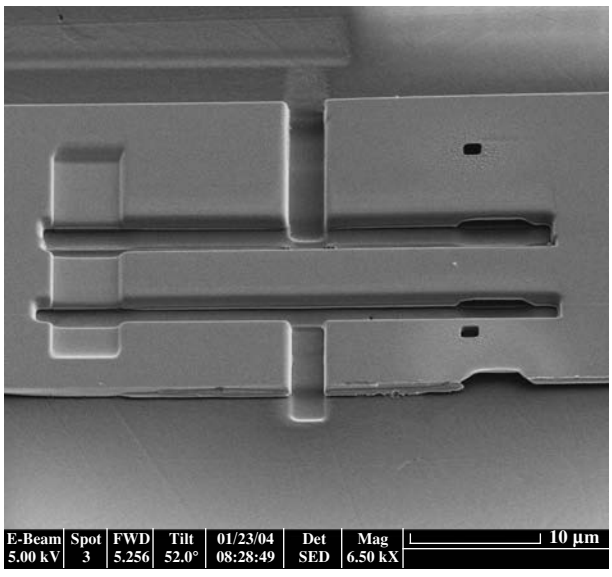

Fig. 1. SEM picture of the stacked structure fabricated by double sided FIB etching of a Bi-2212 single crystal whisker.

¶ The text was submitted by the authors in English.

ented strictly parallel to the *ab*-plane and perpendicular to the *a*-axis. The parallelity of the field orientation was adjusted within 0.01° by fixing that at the sharp maximum of the JFF magnetoresistance with field rotation around the *a*-axis. For that purpose, along with a main coil providing a magnetic field up to 1T, an additional perpendicular coil was used. The data were collected by a computer controlled current source and a nanovoltmeter.

We traced the oscillating dependence of the JFF resistance on a parallel magnetic field at fixed temperatures with temperature variation by small steps (Fig. 2). The period of the oscillations exactly corresponds to 1/2 fluxon per elementary junction, $\Delta B = 0.5\Phi_0/Ls$, with L (the stack size) being perpendicular to the magnetic field and s being the inter-layer spacing. The amplitude of the oscillations decreases with temperature and turns to zero at some temperature T_0, which is 3.5 K below T_c (Fig. 3). Figure 2 shows that, at a fixed temperature, oscillations exist within some field interval. The boundaries of that interval, which are marked in the picture, define the lower and upper boundaries of the triangular JVL state at the *B*–*T* diagram (Fig. 4a).

Let us discuss the main features observed. The characteristic point at the phase diagram corresponds to B = 0.6–0.7 T, where the upper and lower boundaries meet each other at $T = T_0$. There are no JFF oscillations above this temperature. We can then conclude that there is no triangular JVL state above that temperature. The value of T_0 lies 3.5 K below the transition temperature. That is very close to the bare BKT transition temperature observed at zero magnetic field on similar Bi-2212 single crystals [11]. The BKT transition is characterized by spontaneous formation of free pairs of pancake vortices and antivortices within elementary superconducting layers. Below T_{BKT}, the vortex–antivortex pairs can be unbound by the in-plane current and the *I*–*V* characteristics have the power law $V = I^{a(T)+1}$, where the exponent $a = \Phi_0^2 d/(4\pi\lambda)^2$ (with d being the thickness of the layer and λ the London penetration depth) is proportional to the unbinding energy. At the BKT transition, this exponent undergoes a universal jump from 2 to 0, which is known as the Nelson–Kosterlitz jump, which is a characteristic feature of the BKT transition. By observation this jump, the BKT transition has been identified in the elementary conducting layers of Bi-2212 single crystals [12] with $T_{BKT} - T_{co} = 3.5$ K.

The BKT transition in a parallel magnetic field [5, 9] was considered in connection with melting of JVL [7, 8] and with the observation of independent Lorentz force dissipation when both the transport current and magnetic field lie in the *ab*-plane [13]. The elementary process accompanying JVL melting has been considered by Blatter *et al.* [6]; that is, the hopping of a segment of Josephson vortex into the neighboring junction with formation of a loop that includes a pancake vortex and antivortex (Fig. 5).

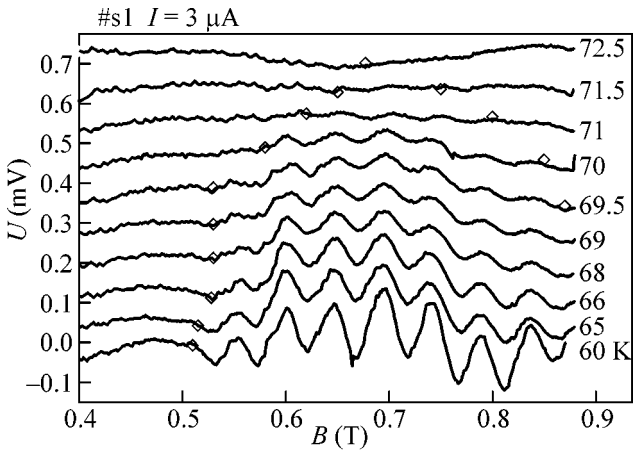

Fig. 2. Semifluxon oscillations of Josephson flux-flow voltage of Bi-2212 mesa with lateral sizes of $L_a \times L_b = 15\ \mu m \times 5\ \mu m$ in the parallel field $B \parallel b$. The linear part is subtracted. The curves are shifted for clarity. The markers (rhombuses) indicate the lower and upper boundaries of the existence of oscillations.

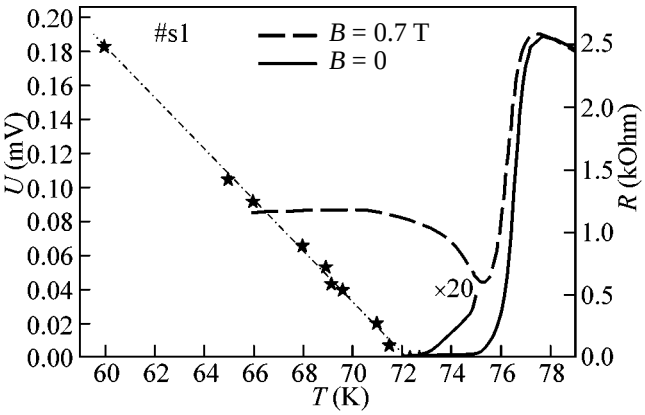

Fig. 3. Temperature dependence of the amplitude of semifluxon JFF oscillations on a parallel magnetic field measured near the field of 0.7 T for the Bi-2212 stacked junction and the superconducting transition for the same junction at zero field and at B = 0.7 T.

The BKT transition facilitates the hopping providing the free vortices and antivortices necessary for formation of a loop. The unbinding of vortex–antivortex pairs by the in-plane component of the current circulating around the Josephson vortex happens even at temperatures considerably lower than T_{BKT}. The hopping becomes preferable at higher temperatures, because of an increase of the thermal fluctuations, and also at a high enough magnetic field with an increase of the vortex concentration and, correspondingly, with an increase of the intervortex repulsive interaction in one junction. The critical field for JVL melting into the

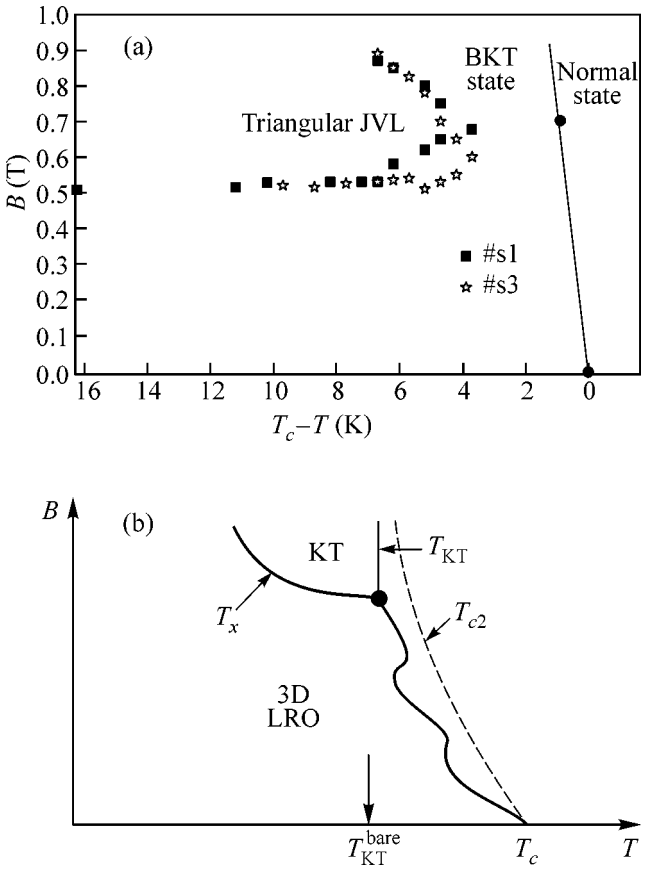

Fig. 4. Phase diagram of the JVL state restored from the data on semifluxon oscillations of the JFF voltage on a parallel magnetic field for two Bi-2212 mesas (a) and the schematic picture of the phase diagram considered in [7] (b).

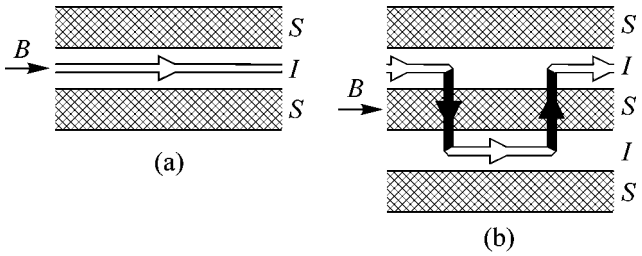

Fig. 5. Schematic illustration of hopping of a Josephson vortex segment with formation of a flux loop containing a pancake vortex and antivortex pair: (a) Josephson vortex before hopping, (b) after hopping.

BKT phase B^* has been calculated by Hu and Tachiki [7, 8] $B^* = \Phi_0/(2\sqrt{3}\gamma s^2)$ with γ being the anisotropy of the London penetration depths $\gamma = \lambda_c/\lambda_{ab}$, and s being the spacing between the elementary conducting layers. They also considered the B–T phase diagram of the JVL melting schematically shown in Fig. 4b.

The experimentally found phase diagram of JVL melting is quite similar to the theoretical picture. The maximum temperature of existence of the BKT phase T_0, as it was mentioned, corresponds well to the bare BKT transition. The critical magnetic field B^* estimated for our samples with $\gamma = 500$ [14] corresponds to 0.5 T, which is close to the experimental value 0.6–0.7 T. The upper boundary of JVL existence is also in qualitative agreement with the theoretical $B(T)$ dependence for the melting line: B grows with a decrease in T. The crossing of the BKT melting line by moving from the JVL state either by increasing the temperature or field corresponds to a continuous decrease of the amplitude of the oscillations to zero without any jump expected for the first order transition. That is a signature of the JVL melting into the BKT phase since, as it was argued in [7] for $\gamma > 9$ and $B > B^*$, it should be a phase transition of the second order. Note that the experimental picture corresponds to the sliding JVL, while the theoretical picture relates to the static case. However, due to the small dc currents used in the experiment, the JVL velocity was relatively small, about 3% of the Swihart velocity.

In contrast, the lower boundary is characterized by much sharper variation of the oscillation amplitude with a decrease of the field. The origin of the low boundary is still not quite clear. The JFF voltage is known to have a threshold as a function of the magnetic field [15] that corresponds to a flux density of $0.7\Phi_0$ per junction. The oscillations appear starting with a field of about 0.5 T and are nearly independent of the temperature. That field corresponds to 5–7 periods of triangular JVL, which appears to be the threshold value for the commensurability effect corresponding to the minimal number of periods for the lattice to start to behave as a solid piece.

We found that the Josephson flux-flow branch still exists on the I–V characteristics above T_{BKT}; however, the JFF voltage drops rapidly at $T > T_{BKT}$ (Fig. 3). The study of the JFF state above T_{BKT} is of great interest for future research. Another interesting point is to study the influence of the c-axis field component on the JVL melting temperature.

We acknowledge fruitful discussions with L.N. Bulaevskii, V. Geshkenbein, and M.B. Gaifullin. This work was supported by the Russian Ministry of Science and Industry (project no. 40.012.1.111.46), the Russian State Program for the Development of New Materials, the Russian Foundation for Basic Research and French Centre National de la Recherche Scientifique (project no. 03-02-22001), and the US Civilian Research and Development Foundation (grant no. RP1-2397-MO-02).

REFERENCES

1. J. Clem and M. Coffey, Phys. Rev. B **42**, 6209 (1990).
2. L. N. Bulaevskii and J. Clem, Phys. Rev. B **44**, 10234 (1991).

3. S. Ooi, T. Mochiku, and K. Hirata, Phys. Rev. Lett. **89**, 247002 (2002).
4. Yu. I. Latyshev, A. E. Koshelev, M. Gaifullin, *et al.*, in *Proceedings of 4th International Symposium on Intrinsic Josephson Effect and Plasma Oscillations in High-T_c Superconductors* (Tsukuba, Ibaraki, Japan, 2004), p. II-85-87.
5. S. E. Korshunov and A. I. Larkin, Phys. Rev. B **46**, 6395 (1992).
6. G. Blatter, B. I. Ivlev, and J. Rhyner, Phys. Rev. Lett. **66**, 2392 (1991).
7. X. Hu and M. Tachiki, Phys. Rev. B **70**, 064 506 (2004).
8. X. Hu and M. Tachiki, Phys. Rev. Lett. **85**, 2577 (2000).
9. B. Horovitz, Phys. Rev. B **47**, 5947 (1993); Phys. Rev. B **47**, 5964 (1993).
10. Yu. I. Latyshev, S.-J. Kim, and T. Yamashita, IEEE Trans. Appl. Supercond. **9**, 4312 (1999).
11. S. N. Artemenko, I. G. Gorlova, and Yu. I. Latyshev, Phys. Lett. A **138**, 428 (1989); S. N. Artemenko and Yu. I. Latyshev, Mod. Phys. Lett. B **6**, 367 (1992).
12. S. N. Artemenko, I. G. Gorlova, and Yu. I. Latyshev, Pis'ma Zh. Éksp. Teor. Fiz. **49**, 566 (1989) [JETP Lett. **49**, 654 (1989)].
13. Y. Iye, S. Nakamura, and S. Tamegai, Physica C (Amsterdam) **169**, 433 (1989).
14. Yu. I. Latyshev, A. E. Koshelev, and L. N. Bulaevskii, Phys. Rev. B **68**, 134504 (2003).
15. Yu. I. Latyshev, A. E. Koshelev, V. N. Pavlenko, *et al.*, Physica C (Amsterdam) **367**, 365 (2002).

JETP Letters, Vol. 82, No. 4, 2005, pp. 236–240. Translated from Pis'ma v Zhurnal Éksperimental'noĭ i Teoreticheskoĭ Fiziki, Vol. 82, No. 4, 2005, pp. 255–259.

Minimum Energy of a Free Electron in Inert Gases

S. Nazin and V. Shikin

Institute of Solid State Physics, Russian Academy of Sciences, Chernogolovka, Moscow region, 142432 Russia

Received June 23, 2005

The properties of the minimum energy W of a low-energy free electron in an inert gas are discussed. This quantity is one of the basic characteristics of the electron in problems of the formation of various charged clusters (bubbles or compacts) in low-dimensional electronic states along interfaces. A relation between the energy W and a similar energy W_0 determined in the so-called optical approximation, where the energy W_0 is proportional to the gas density n_g, has been obtained. Comparison makes it possible to determine the n_g dependence of the scattering length a_0 introduced in the "optical" description of the gaseous medium and to reveal the conditions under which $a_0(n_g)$ may change sign, which behavior, by definition, is beyond the framework of the optical approximation and is observed experimentally. © *2005 Pleiades Publishing, Inc.*

PACS numbers: 67.70.+n, 72.60.+g

One of the basic characteristics of a low-energy electron in inert gases is its average minimum energy W determining the behavior of the electron in such media (free motion at lengths much larger than interatomic distances or localization). In this context, the optical approximation (see [1] and further publications [2–9], where this approach was developed; the list of references may be expanded)

$$W_0 = \frac{2\pi\hbar^2 a_0}{m} n_g \quad (1)$$

is very usable. Here, n_g is the average gas density, m is the free-electron mass, and a_0 is the so-called scattering length of a slow electron on a given atom, which is closely related with the s component of the electron scattering amplitude on the atom. Representation (1) is particularly valuable for solving inhomogeneous problems such as bubble or cluster problems, where the local definition of the energy W_0 by Eq. (1) with the coordinate-dependent density $n_g(r)$ has no alternative [10–12].

Formula (1) is certainly valid for the contact interaction $V_0(\mathbf{r} - \mathbf{R_i})$ of the electron with an atom:

$$V_0(\mathbf{r} - \mathbf{R_i}) = \frac{2\pi\hbar^2 a_0}{m} \delta(\mathbf{r} - \mathbf{R_i}), \quad (2)$$

where $\delta(x)$ is the Dirac delta function. In fact, this interaction $V(r)$ is more complex, and formula (1) remains acceptable if the scattering length, which is an integral characteristic of $V(r)$, depends slightly on n_g. The situation for inert gases seems to be acceptable, because a_0 is independent of n_g as follows from data on the electron mobility in rarefied gases. For He, Ne, Ar, Kr, and Xe, $a_0/a_B \simeq +1.16$, 0.45, –1.63, –3.8, and –6.8, respectively, where a_B is the Bohr radius (see [13, 14], where the references to the information sources are given). However, optical data indicate the formation of an electron–helium bound state (a negative helium ion has a binding energy of about 0.07 eV [15–17]). Therefore, the scattering length in low-density gaseous helium that enters into Eq. (1) is negative (we recall that an electron is pushed out of the liquid helium bulk with an energy of $W \sim 1$ eV [12, 14, 18–20]; therefore, a_0 in Eq. (1) is positive in this case).

Independent examples of the change in sign of a_0 are presented by molecular hydrogen (here, a_0 is positive for the liquid and solid phases, whereas it is negative for the gas [21]) and argon, where the signs of a_0 are different for the liquid and solid phases [13, 22, 23]. Thus, the dependence $a_0(n_g)$ is expected for all inert gases, although information on this dependence is scarce. The aim of this work is to fill in this gap. The problem of interest is to determine the energy $W(n_g)$ with the maximum inclusion of information on the polarization interaction of the electron with surrounding atoms, including a qualitatively correct passage to the limit of zero gas density. The further comparison $W(n_g)$ with $W_0(n_g)$ given by Eq. (1) provides an estimate of the gas-density dependence of the effective scattering length a_0 for small and intermediate n_g values and the unification of available separate data on the $a_0(n_g)$ behavior, including the appearance of negative values of this parameter.

1. To start formulating the problem, we note that the calculations are performed in the previously used Wigner–Seitz spherical model [5, 6], in which an atom of a gas is located at the center of the cell and the presence of other atoms is approximately taken into account by the boundary condition at its outer boundary with the radius R depending on the vapor density as (the dif-

ference between [5, 6] and our work will be commented on below)

$$(2R)^3 = n_g^{-1}. \quad (3)$$

Thus, the problem is formally reduced to the search for the ground state W for the electron in a spherically symmetric polarization-induced well described by the following potential (the N nearest neighbors are closely located on the first coordination sphere with the radius $2R$) composed of individual polarization contributions of various atoms:

$$V(r) = V_0(r) + \left\langle \sum_{i=1}^{N} V_0(2\mathbf{R_i} - \mathbf{r}) \right\rangle. \quad (4)$$

Here,

$$V_0(r) = \begin{cases} V_0 > 0, & r \le a \\ -\alpha e^2/2r^4, & r > a, \end{cases} \quad (5)$$

where α is the polarizability of the atom and a is its effective radius that is the variable parameter in further calculations.

The interaction $V_0(r)$ given by Eq. (5) is not used in accurate (including numerical) calculations of the binding energy of an extra electron with an isolated inert-gas atom (see, e.g., [24]). Nevertheless, since the dependence $W(n_g)$ is primarily of interest and in order to minimize numerical calculations, we use Eq. (5), which allows the application of the one-electron approximation. In this case, the interaction of the extra electron with "internal" atomic electrons is represented by the appropriate boundary condition for the electron wave function on the "surface" of the atom with radius a. This condition excludes the fall of the particle onto the attractive center and takes into account the hardness of internal shells. The importance of the latter circumstance is seen at least from the fact that the helium atom, whose atomic polarization α is minimal among inert gases, binds the extra electron with the binding energy ~0.07 eV, whereas other representatives of this series with much larger α values have no bound states [24]. The single-electron formalism proposed below qualitatively takes into account this circumstance.

Boundary conditions. They are comparatively simple on the outer boundary of the cell. There is the natural requirement

$$\psi'(R) = 0, \quad (6)$$

which efficiently allows the electron with the wave function $\psi(r)$ to move from one cell to another. In order to reveal the details of the $W(n_g)$ dependence, it is also appropriate to use the alternative requirement

$$\psi(R) = 0. \quad (7)$$

As was mentioned above, the boundary conditions on the inner boundary $r = a$ should be specially discussed. Under these conditions, it is desirable to provide the possibility of localizing the electron (or its absence) on an individual atom. At first glance, the atomic polarizability α is of most importance in the interplay of the parameters (the larger the α value, the higher the localization probability). However, the situation is opposite. The helium atoms with the minimum α value form a negative ion [15–17], while the other inert gases do not form such an ion [24]. Only the boundary conditions that may invert the situation remain in the single-electron formalism.

To reveal the desired perspective, we consider the impedance solution of the problem of the electron localization on the center with potential (5). It is easy to verify that the electron wave function near a polarized atom has the form

$$\psi(r) = A\sin(\lambda/r) + B\cos(\lambda/r), \quad \lambda = \sqrt{\alpha/a_B}, \quad a_B = \hbar^2/me^2, \quad (8)$$

and a_B is the Bohr radius. In the general case, the single-electron problem with attraction $\propto -r^{-4}$ is reduced to the Mathieu equation [25, 26]. The asymptotic form of such wave functions at small distances is given by Eq. (8).

The approximation with vanishing $\psi(r)$ on the atomic surface:

$$\psi(r)|_{r=a} = 0 \quad (9)$$

leads to the relation between the coefficients A and B:

$$A = -B\cot(\lambda/a); \quad (10)$$

where a is the atomic radius. The alternative case has the form

$$\psi'(r)|_{r=a} = 0, \quad A = B\tan(\lambda/a). \quad (11)$$

Then, setting

$$\psi(r) \simeq C\frac{\exp(-\kappa x)}{r} \quad (12)$$

at large distances and asymptotically matching Eqs. (8) and (12), for the case given by Eqs. (9) and (10), we obtain

$$\kappa^{-1} = \lambda\cot(\lambda/a). \quad (13)$$

Matching Eqs. (8) and (12) for the case given by Eq. (11), we arrive at

$$\kappa^{-1} = -\lambda\tan(\lambda/a). \quad (14)$$

By varying α, it is easy to verify that result (13) is physically meaningless. First, in this result, there is no threshold that is characteristic of three-dimensional problems with localization. Second, as α decreases, although the localization length κ^{-1} increases (this behavior is reasonable), it approaches a finite limit a_B from the side of small values of $a < a_B$, which is senseless!

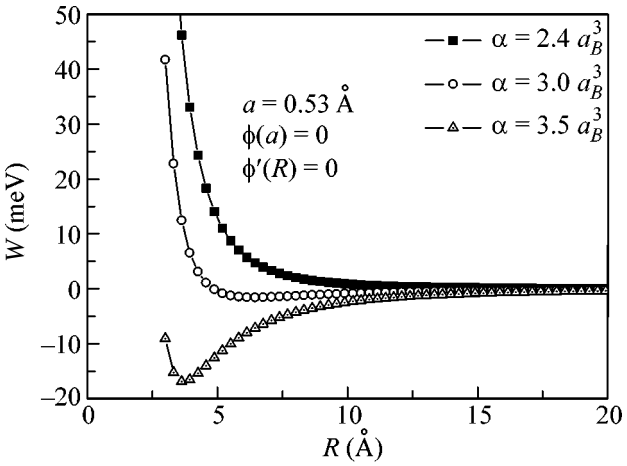

Fig. 1. Energy $W(R, \alpha)$ vs. R for various α values for the problem given by Eqs. (6) and (9) with the fixed value $a = a_B$. The fan of the plots is chosen so that it includes the transition from the case with no minimum to the case with a minimum in the $W(R)$ plot that occurs at the critical value $\alpha_c/a_B^3 = 2.48$ (for arbitrary a values, $\alpha_c/a_B a_c^2 \simeq 2.48$).

Variant (14) is more physically meaningful. First, there is a pronounced threshold for the electron localization. Indeed, κ^{-1} and, therefore, the right-hand side of Eq. (14) are positive if $\tan(\lambda/a)$ is negative, which is possible if

$$\lambda/a \geq \pi/2. \tag{15}$$

Second, the localization length κ^{-1} decreases, beginning from infinity, as α increases in the region $\lambda/a \geq \pi/2$ [λ increases, but $-\tan(\lambda/a)$ decreases nonlinearly in the interval $\pi/2 < (\lambda/\alpha) < \pi$, so that the right-hand side of Eq. (14) diverges at the point $\pi/2$ and decreases monotonically above the localization threshold).

Thus, boundary condition (9) at the inner boundary excludes the localization of the electron on an atom with an arbitrary α value with impedance accuracy. This boundary condition should be imposed for all atoms except helium, whereas the localization possibility should remain for helium, which corresponds to requirement (11). Threshold (15) is formally reached at a given α value by varying the inner radius a, which is considered as a varying parameter in our formulation.

The numerical analysis corroborates the impedance picture given by Eqs. (8)–(15) of the electron behavior near an individual atom.

2. Discussion of the boundary conditions given by Eqs. (9) and (11) completes the formulation of the problem. The wave equation was solved numerically for the known series of inert gases with "individual" boundary conditions at the inner and outer boundaries of the Wigner cell and parameters taken from references (atomic weight and density [27], polarizability [13, 14], binding energy in a negative ion [24], and barrier height [12, 14, 18–20, 22, 23, 28]). Then, the desired scattering length is calculated by the formula

$$a_0(n_g) = \frac{mW(n_g)}{2\pi\hbar^2 n_g}, \tag{16}$$

where $W(n_g)$ is the numerically found energy of the electron ground state in the cell with the outer radius determined from Eq. (3) for various gas densities. The inner radius a was chosen for each gas by taking into account additional circumstances (existence of a bound state in the limit of zero gas density, the known energy of the electron interacting with the liquid phase, etc.).

A necessary test is the existence of the threshold of the formation of a bound state in the problem given by Eqs. (6) and (11) at zero gas density. The change $r \longrightarrow Ar$ and $\alpha \longrightarrow A^2\alpha$ transforms the radial Schrödinger equation with the potential $V(r) = -\alpha e^2/2r^4$ in the semi-infinite interval (a, ∞) with the boundary conditions $\psi'(a) = \psi(\infty) = 0$ to the same equation in the interval (Aa, ∞) with the energy change $E \longrightarrow E/A^2$. This means that the critical values α_c and a_c at which the bound state first appears (at the time of its appearance, its energy $E = 0$) are related by the scaling expression

$$\alpha_c = Ca_c^2. \tag{17}$$

The numerical solution of the Schrödinger equation shows that the coefficient C in this expression is equal to 2.48, which coincides with the value $C = \pi^2/4$ followed from Eq. (15) with an accuracy better than 1%.

With the same accuracy, the problem given by Eqs. (6) and (9) in the limit $n_g \longrightarrow 0$ has no bound states, as was expected [see Fig. 1, where $W(R) \longrightarrow 0$ for $R \longrightarrow \infty$].

Within the framework of our plan, we consider the dependence $W(R, \alpha)$ for the problem given by Eqs. (6) and (9) with a continuous increase in α and the fixed value $a \sim a_B$. The fan of the corresponding plots in Fig. 1 exhibits the threshold change in the regime from the monotonic behavior of the energy with $dW/dR < 0$ to the appearance of increasing nonmonotonicity in this dependence. Similar to the case given by Eq. (15), the threshold following from the data presented in Fig. 1 exhibits the scaling behavior given by Eq. (17) (with the same proportion constant). The physical sense of the behavior in Fig. 1 is clear. The energy W integrally includes the contribution of zero oscillations and polarization attraction: $W \simeq W_\hbar - W_\alpha$, where $W_\hbar \propto R^{-2}$. The main part of W_α comes from small distances $r \geq a$ and depends slightly on R. Another part of W_α comes from the region $r \leq R$, where the "vertex" of interaction (4) decreases rapidly with R: $\partial V/\partial R \propto R^{-5}$. If the wave function is nonzero in this region [which is ensured by boundary conditions (6)], the negative contribution from $r \leq R$ to W becomes dominant beginning with a certain threshold in α and finally leads to nonmonotonicity in the behavior of $W(R, \alpha)$ shown in Fig. 1.

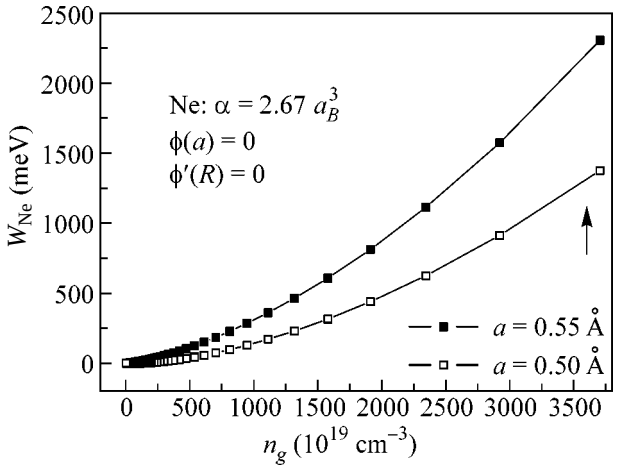

Fig. 2. Energy $W_{Ne}(n_g)$ for Ne with two different radii a. The value a = 0.50 Å, for which the energy W_{Ne} reaches a value of about 1.05 eV [28] for the liquid-phase Ne density, is favorable. This position on the horizontal axis is marked by the arrow.

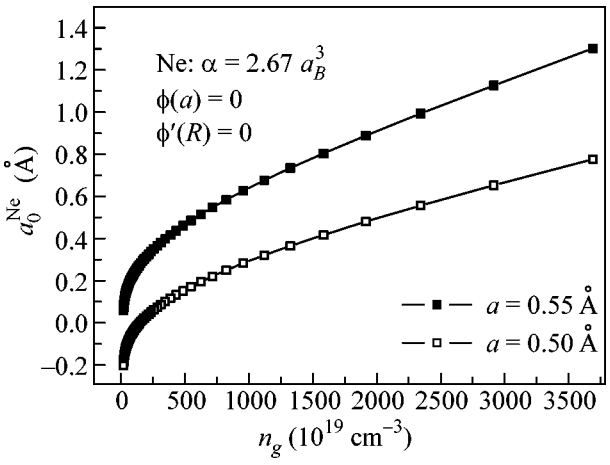

Fig. 3. Scattering length a_0^{Ne} according to Eq. (16) and data presented in Fig. 2 for $W_{Ne}(n_g)$.

Neon is a typical "monotonic" representative among inert gases. The problem given by Eqs. (6) and (9) for Ne, where the radius a_{Ne} is varied to fit the observed energy W in the liquid state, falls into the subthreshold region (Fig. 1) and gives the general behavior of $W_{Ne}(n_g)$ presented in Fig. 2. Then, $a_0^{Ne}(n_g)$ is obtained from Eq. (16) (see Fig. 3).

Argon lies on the other side of the boundary (Fig. 1). The change of the sign of the energy $W_{Ar}(n_g)$ in the transition from the liquid state to the solid one can be obtained by varying a_0^{Ar}. In this case, the problem given by Eqs. (6) and (9) leads to the result shown in Fig. 4, which indicates that W changes sign at the boundary R = 1.8 Å, which corresponds to the liquid argon density (the change is easily shifted to the liquid argon–solid argon interface, where a_0^{Ar} really changes sign). Thus, the change of the sign of a_0^{Ar} observed in argon in its transition from the liquid state to the solid one [23] has a polarization origin associated with the contribution of the periphery of the Wigner–Seitz cell to the energy W. This contribution cannot be separated by varying only the effective scattering length extracted from the data on the electron mobility in gaseous and liquid argon, as was done in [22] (see below and comments to [5, 6]).

The $W(n_g)$ dependences for xenon and krypton are similar to the plot in Fig. 4 with the expanding region of negative energies. Gaseous ^{3}He and ^{4}He in the general inert series require special consideration with the use of the wave solution in the cell with the boundary conditions given by Eqs. (6) and (11). The properties of $W_{He}(n_g)$ in this problem will be discussed elsewhere.

Summary. In this work, formalism has been proposed that provides a more detailed analysis of the polarization contribution to the minimum energy W of a free electron in an inert gas. In the single-electron approximation, this formalism completely includes details of the interaction of the electron with atoms of the gas both near atomic centers and at their periphery. Qualitatively different branches have been found in the behavior of $W(n_g)$ in dependence on the capability of an atom to form a negative ion. The situation in which an individual atom does not form a bound state with an extra electron has been analyzed in detail. It has been shown that separation in the parameter $\gamma \propto \alpha/a_B a^2$ exists

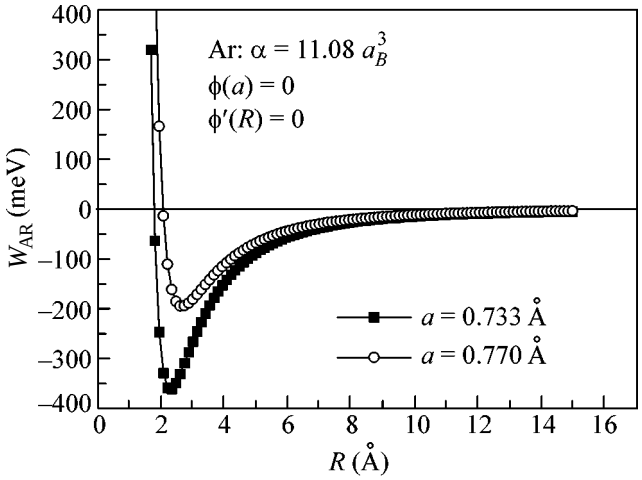

Fig. 4. Energy $W_{Ar}(n_g)$ for Ar with two different radii a. The value a = 0.733 Å, for which the energy W_{Ar} passes through zero at the point R = 1.81 Å corresponding to the liquid-phase Ar density, is favorable. The distance R is related to the density n_g by Eq. (3).

in this set of "participants" to which all inert gases except He belong. For small γ values, the energy $W(n_g)$ is everywhere positive (the case of neon). As γ increases, the behavior of $W(n_g)$ becomes nonmonotonic and this function becomes negative for intermediate n_g values. Argon and heavier gas exhibit such a nonmonotonicity.

It is worth noting that, although a_0 depends pronouncedly on the gas density, this dependence is relatively weak. In particular, the length a_0^{Ne} for Ne changes by a factor of only 2–3 when the density changes by several orders of magnitude (see Fig. 3). This circumstance justifies the application of the optical approximation given by Eq. (1) in problems [10–12, 21], where the gas (fluid) density varies within a small interval.

Let us make some comments on the calculations [5, 6] where the Wigner–Seitz cell was used. In those works, the wave function in the cell was taken in the form

$$\psi(r) \propto \sin[k_0(r - a_0)]/r \quad (18)$$

with the additional boundary condition given by Eq. (6). In such a representation, most information on the effect of polarization on the properties of the electron energy in the cell is obviously lost. The expression for the energy

$$W_*(n_g) = \hbar^2 k_0^2/2m, \quad k_0 R = \tan[k_0(R - a)], \quad (19)$$

that was derived in [6] is monotonic [here, polarizability can be effectively introduced only through the dependence $a(\alpha)$].

This work was supported in part by the Russian Foundation for Basic Research (project no. 03-02-16121) and the Presidium of the Russian Academy of Sciences (program no. P28).

REFERENCES

1. E. Fermi, Nuovo Cimento **11**, 157 (1934).
2. H. Margenau and W. Watson, Rev. Mod. Phys. **8**, 22 (1936).
3. L. Foldy, Phys. Rev. **67**, 107 (1945).
4. B. Burdick, Phys. Rev. Lett. **14**, 11 (1965).
5. J. Jortner, N. Kestner, S. Rice, and M. Cohen, J. Chem. Phys. **43**, 2614 (1965).
6. B. Springet, J. Jortner, and M. Cohen, J. Chem. Phys. **48**, 2720 (1968).
7. L. Tankersley, J. Low Temp. Phys. **11**, 451 (1973).
8. A. Fetter, in *The Physics of Liquid and Solid Helium*, Ed. by K. Berreman and J. Ketterson (Wiley, New York, 1976).
9. E. Bashkin, Zh. Éksp. Teor. Fiz. **82**, 1868 (1982) [Sov. Phys. JETP **55**, 1076 (1982)].
10. C. Kuper, Phys. Rev. **122**, 1007 (1961).
11. J. Levin and T. Sanders, Phys. Rev. **154**, 138 (1967).
12. V. Shikin, Usp. Fiz. Nauk **121**, 457 (1977) [Sov. Phys. Usp. **20**, 226 (1977)].
13. T. O'Malley, Phys. Rev. **130**, 1020 (1963).
14. A. Khrapak and I. Yakubov, *Electrons in Dense Gases and Plasma* (Nauka, Moscow, 1981) [in Russian].
15. B. Smirnov and M. Chibisov, Zh. Éksp. Teor. Fiz. **49**, 841 (1965) [Sov. Phys. JETP **22**, 585 (1966)].
16. A. Rivier and D. Sweetman, Phys. Rev. Lett. **5**, 560 (1960).
17. V. Oparin, R. Il'in, I. Serenkov, *et al.*, Pis'ma Zh. Éksp. Teor. Fiz. **12**, 237 (1970) [JETP Lett. **12**, 162 (1970)].
18. M. Woolf and G. Reifield, Phys. Rev. Lett. **15**, 235 (1965).
19. W. Schoepe and G. Reifield, Phys. Rev. A **7**, 2111 (1973).
20. J. Broomall, W. Johnson, and D. Onn, Phys. Rev. B **14**, 2819 (1976).
21. V. Zav'yalov and I. Smol'yaniniv, Zh. Éksp. Teor. Fiz. **92**, 339 (1987) [Sov. Phys. JETP **65**, 194 (1987)].
22. J. Lekner, Phys. Rev. **158**, 130 (1967).
23. J. Jortner and A. Gaathon, Can. J. Chem. **55**, 1801 (1977).
24. B. M. Smirnov, *Negative Ions* (Atomizdat, Moscow, 1978; McGraw-Hill, New York, 1982).
25. E. Vogt and G. Wannier, Phys. Rev. **95**, 1190 (1954).
26. T. O'Malley, L. Spruch, and L. Rosenberg, J. Math. Phys. **2**, 491 (1961).
27. *Physical Encyclopedic Dictionary*, Ed. by A. M. Prokhorov (Sovetskaya Entsiklopediya, Moscow, 1960) [in Russian].
28. W. Tauchert, H. Jungblut, and W. Schmidt, Can. J. Chem. **55**, 1860 (1977).

Translated by R. Tyapaev